UNIVERSITEIT VAN PRETORIA
UNIVERSITY OF PRETORIA
YUNIBESITHI YA PRETORIA

University of Pretoria

Optimisation of microstructures and texture of AISI 436 steel through simulated hot rolling for improved drawability and surface quality

By

Muhammed Yusuf Salojee

Supervised by

Prof. Charles W. Siyasiya

Dr Kofi A. Annan

Submitted in partial fulfilment of the requirement for the degree

Master of Engineering (Metallurgy)

in the

Department of Materials Science and Metallurgical Engineering,

Faculty of Engineering, Built Environment & Information Technology

October 2024

Acknowledgements

We grow, not in solitude but through experiences and support gained from those around us. I believe their support have motivated me to achieve the finalisation of this dissertation into a coherent piece of work that they and I are proud of.

My supervisors, who, unlike the many horrendous stories I've read around the world, were completely supportive of my side projects and work, encouraged and assisted me throughout the process and were available to the best of their abilities. I would wholeheartedly like to thank Mintek and Columbus Stainless Steel for the generous funding and financial support made available to me through a time that was bleak for many.

I cannot name all my colleagues, postgraduate and undergraduate students, but thank you for the laughs and giggles, the assistance and the open sharing of knowledge throughout our journey. Finally, I cannot thank the department and its staff enough, including IMMRI, for making my learning process worthwhile.

I want to dedicate this paragraph to my friends and family. Thank you to my friends, Baitshepi, Gabisile, Mohammed Faheem, Ridwaan, Reza, Joshua, Kyle, Thabang, Shane and others who entertained my never-ending list of frustrations. To my friends who came into my life over the past year, Izak, Kyle, and others, I do not believe I could have done this without you. I love you all, and thank you so much for your support.

My parents, Fatima and Yusuf, for giving me the opportunities you were deprived of and understanding my unique personality; you have a special place in my heart. My siblings, Bilaal and Salmah, who are quite frankly more than siblings, please know that I will always be here for you. Finally, my nieces and nephews, yes, I do love you even though I hid away from you to write this never-ending length of work. I hope this work encourages aspiring masters' students to trust and believe in themselves, regardless of circumstance and situation.

Abstract

Ferritic stainless steels (FSS) are a versatile, cheaper alternative to austenitic stainless steel. This has resulted in a growing research interest in these steels. However, the downside of ferritic stainless steel is that they exhibit surface ridging, which contributes negatively to the final product aesthetics and requires machining and polishing to rectify this defect. The manifestation of ridging is known to be inherited from the casting and hot rolling of the FSS sheets. This study delved into the effects of the hot working parameters on the evolution of the microstructures and texture in 436 FSS through lab-based thermomechanical uniaxial, isothermal compression simulations. In a previous study on the optimisation of the roughing rolling process, it was shown that by varying the rolling parameters, it was possible to accumulate strain prior to the finishing rolling process. Therefore, in this work, the roughing rolling was simulated in such way to achieve a variation in the retained strain prior to the finishing rolling process with the intention of studying its effect on the recrystallisation process during the finishing rolling process. The simulated finishing rolling process parameters were kept constant.

The industrial rolling process was simulated through multi-pass hot deformation, using the Gleeble 1500 and Bähr Dilatometer 850D thermomechanical simulators. The roughing and finishing rolling processes were simulated by three multi-pass deformation passes each. The strains were varied between 0.18 and 0.3 per pass with total strains per schedule ranging between 0.58 and 1.4. Strain rates were varied between 5 and 15 /s while inter-pass times were varied between 11 and 50 s per pass. The strain rates were consistent with the industrial roughing rolling but not the finishing rolling process because the latter was not achievable in the lab. The microstructures and hardness values were studied using the Olympus BX51M microscope, Jeol IT300LV SEM equipped with XMAX^n EDS and Oxford Nordlys Nano EBSD detectors and a Struers Duramin-40 automated hardness tester. The Channel 5 software was used for texture characterisation and ImageJ was used for the microstructural analysis.

The particle stimulated nucleation was present in all hot working schedules. As expected, the recrystallisation mechanism was by DDRX. This resulted in random grain orientations around the inclusions and precipitates. However, the recrystallised fraction was not adequate to significantly change the bulk of the cast structure and texture.

The simulated roughing rolling schedule, R2, with increased total strain (from 0.68 to 0.8) and inter-pass times (from 43.3 to 60 s), exhibited less sub-grain refinement i.e., resulted in less retained strain than the other two schedules, CF and R1 after three passes. This resulted in CR and R1 schedules having increased driving force for recrystallisation during roughing but less retained strained for recrystallisation during finishing. The goal of accumulating strain during the simulated roughing rolling process to act as the driving for recrystallization during finishing rolling was not achieved, but this increased the potential for strain retention during finishing. Annealing of the finishing rolling schedules proved this by showing a higher reduction in hardness values of 14% compared to the simulated benchmark with a 2% reduction in hardness value. The accumulated strain per pass in all simulations could not reach the critical strain for recrystallisation during the simulated finishing rolling process to aid the breaking down of the cast columnar grains with predominantly Cube oriented grains. This was attributed to the limitations in strain rates and strains in laboratory simulations. However, industrial hot rolling with higher strain rates, and strains could possibly overcome these limitations i.e., the accumulated strain between passes could reach the critical strain for recrystallisation. Therefore, it would be worthwhile doing plant trials of higher strain per pass and increased inter-pass time during the roughing rolling or the early finishing passes to accumulate strain to aid the recrystallisation process during the latter finishing rolling passes, without substantial drop in temperature to trigger mill stoppage due to increased mill load.

Publications

Conferences & Presentations:

1. Salojee, M., Siyasiya, C.W., Annan, K.A, Moema J., 2021. Effect of Hot Rolling Parameters on Recovery Mechanism in 436 (17%Cr, Nb-Mo) Ferritic Stainless Steel. Suid-Afrikaanse Tydskrif vir Natuurwetenskap en Tegnologie. 40(1):1-7.
2. Salojee, M., Siyasiya, C.W., Annan, K.A, Moema J., Electron backscatter diffraction postprocessing techniques for studying recrystallisation phenomenon of Ferritic Stainless Steel. Paper presented at the 2022 RAPDASA-RobMech-PRASA-CoSAAMI Conference; 2022 Dec.; Stellenbosch, South Africa.
3. Salojee, M., Siyasiya, C.W., Annan, K.A, Moema J., Precipitate Evolution During Hot Rolling & it's Implication on Recrystallisation in 436 Stainless Steels. Paper presented at Microscopy Society of Southern Africa 2022 on Microscopy; 2022 Dec.; Johannesburg, South Africa.
4. M. Salojee, C. W. Siyasiya, K. A. Annan, J. S Moema; Effects of strain and inter-pass time on the softening behaviour of 436 stainless steels, Journal of Materials Engineering and Performance, *Under Review*.

Candidature

Candidate: Muhammed Yusuf Salojee

Supervisors: Professor Charles Witness Siyasiya,

Doctor Kofi Ahomkah Annan

Department: Materials Science and Metallurgical Engineering

University: University of Pretoria, South Africa

Degree: MEng (Metallurgical Engineering)

List of Abbreviations/ Acronyms/ Initialisms

BCC	Body-centred cubic crystal.
BCT	Body-centred tetragonal crystal.
CSL	Coincident site lattice
CDRX	Continuous dynamic recrystallisation
DRV	Dynamic recovery
DDRX	Discontinuous dynamic recrystallisation
DRX	Dynamic recrystallisation
EBSD	Electron backscatter diffraction
FCC	Face-centred cubic crystal.
FSS	Ferritic stainless steel
GB	Grain boundary
GDRX	Geometric dynamic recrystallisation
GG	Grain growth.
HAGB	High-angle grain boundaries
LAGB	Low-angle grain boundaries
ND	Normal Direction- The direction perpendicular to the rolling and transverse directions, moving out of the sheet plane.
ODF	Orientation distribution factor
ppt	Precipitate
RD	Rolling Direction- The direction is parallel to the direction of rolling for a sheet.
REC	Recovery of crystal.
RX	Recrystallisation.
SD	Standard deviation
SEM	Secondary electron microscopy
SRX	Static recrystallisation
TD	Transverse Direction- The direction perpendicular to the direction of rolling within the plane of the sheet (not accurate for uniaxial tests).
XRD	X-ray diffraction

List of Symbols

a	Lattice parameter; x-axial length
$\bar{b}$	Burgers vector
%CW	Percentage of cold work
$\overline{D}$	Average grain diameter
d_{hkl}	Interplanar spacing relevant to Miller parameters h, k, l
F	Force
(hkl)	Miller indices relevant to a plane
l	length
T	Temperature
T_m	Melting temperature
$[uvw]$	Indices relevant to the crystallographic direction
z-phase	Phase forming in stainless steels associated with embrittlement
α	Phase designated as by Greek symbol, having a BCC crystal structure for steel
α-fibre	Crystals having <110> direction // to the RD in a rolled product
γ	Austenite phase designated as by Greek symbol, having an FCC crystal structure for steel
γ-fibre	Crystals having <111> direction // to the ND in a rolled product
σ	Greek symbol designated to represent sigma phase found in stainless steel
θ	Bragg incidence angle

Table of Contents

List of Figures

List of Tables

Chapter 1: General Background

1 GENERAL BACKGROUND

1.1 Introduction

Columbus Stainless is the only fully integrated stainless-steel producer in Africa. The company has a client base throughout the world, and to meet the needs of the competitive global markets, it requires products of optimum quality [1]. The company's product range includes austenitic (ASSs), martensitic, duplex and ferritic stainless steel (FSS) grades. FSS has attracted attention in applications where ASS was previously required due to its low cost and improved mechanical properties. Ferritic stainless steels have rarely been exploited upon the advent of stainless steels [2, 3, 4]. The appeal taken by the FSS market was primarily due to the high cost and the volatility in the nickel (Ni) market price [4, 5, 6]. Ni is an austenite former which improves the steel's ductility and retention of the mechanical properties at high temperature [7]. Ferritic stainless steels have attractive properties such as their aesthetic appeal, very good thermal properties and they are magnetic [7, 8, 9].

FSSs however have low drawability relative to austenitic stainless steel and are prone to a surface phenomenon commonly referred to as ridging [6-10]. The low drawability and ridging phenomenon of FSS limits its use in applications that require high ductility and good surface finish. Certain grades of FSS are therefore stabilised to improve the problem of drawability and ridging [10]. During solidification and subsequent cooling, stabilising elements, such as titanium (Ti), niobium (Nb) and aluminium (Al) tie up carbon and nitrogen in highly stable carbides and nitrides, lowering the solution's carbon (C) content, which makes 16 – 18% chromium (Cr) grades fully ferritic at all temperature ranges. An improvement in properties such as drawability, pitting corrosion resistance, high-temperature strength and creep resistance are achieved in stabilised grades of FSS. The stabilising elements have a high affinity for sulphur (S) and oxygen (O) in addition to C and therefore tend to act as ferrite-forming elements; this allows for ferrite formation and hinders detrimental Cr carbide formations [2, 7, 9, 12].

Ridging is characterised by the appearance of parallel alternating elevations and valleys on the surface of FSS along the transverse direction during rolling [11, 12, 13].

Scientifically, the phenomenon manifests due to the grains of the material assuming preferred homogeneous clusters of orientations within the steel sheet. These clusters spread non-randomly throughout the material. This uneven distribution produces anisotropic properties during plastic deformation of the sheet material, resulting in these undulations following drawing [8, 11, 14]. Textures from upstream processes impact annealing and cold rolling orientations formed. Therefore, microstructural engineering requires optimisation of the entire processing route [8, 17-19]. Kruger [15] argued that microstructures could be either highly strained or recrystallised through continuous dynamic recrystallisation (CDRX).

For recrystallisation to occur, a certain amount of critical strain is required to initiate the recrystallisation process [16]. Previous work [17] showed that in FSS, DRX to DRV transition temperature decreased with increased strain rates. It further showed that the DRX to DRV transition temperature increased with inter-pass times.

Micro-shear bands have been found to assist in CDRX, where their formation has been confirmed through TEM, EBSD and optical microscopy. It occurs when dislocations organise into cellular structures leading to the formation of micro-shear bands. These bands act as nucleation sites for recrystallisation [18, 19, 20].

This study focused on simulating roughing parameters with an aim to retain strain within the microstructure. The retained strain would aid in recrystallisation and subsequently lead to a breakdown of unwanted textures through recrystallisation during finishing. The main roughing parameters manipulated were strain and inter-pass time, whilst finishing parameters were kept constant. The effects of strain rate were also studied to supplement the main study.

1.2 Problem statement

Ferritic stainless steels offer an attractive, inexpensive alternative to its austenitic stainless steels (ASSs) counterparts. However, FSSs suffer from poor surface quality known as ridging upon deep drawing, resulting in a loss of aesthetics [8, 18, 25]. Extensive and costly amounts of grinding and polishing are required to remove this manifestation as FSSs find use in applications where appearance is of significance [21].

Substantial research to address the knowledge gap and cause of surface ridging in FSS consensually found that uneven grain orientation distributions manifest as surface ridging [11, 14]. These grain distributions inherited from casting and hot rolling result in anisotropic plastic deformation properties during the final drawing of the cold-rolled sheet [6, 8, 11, 17, 27]. Research to mitigate the effects of uneven orientation banding in FSSs looking at the casting practices [22, 23], hot rolling conditions [6, 8,19], hot band annealing and final cold rolling and annealing practices [4, 9, 11] has been the primary focus of studies.

The 436 FSS grade does not undergo any austenite to ferrite phase transformation, hence, besides controlling the casting parameters, the only means of grain refinement and orientation randomisation within the material would be controlled thermomechanical processing (TMP). The aim of TMP within the current context is to encourage recrystallisation, which discourages bands of orientations in the microstructure, as randomly nucleated new grains form [19, 27]. However, recrystallisation in FSS is a challenge as it has a body-centred-cubic (BCC) structure that is prone to cross-slip due to the high stacking fault energy (SFE) and, as such, favours recovery above recrystallisation [19, 27, 28]. It is well-known fact that the final sheet inherits its texture from upstream processing. For FSSs, recrystallisation is encouraged by retained strain in the crystal structure at lower temperatures. The focus of the current study was to establish whether promoting a highly strained crystal structure during roughing would improve the texture characteristics during the finishing hot rolling of FSSs.

1.3 **Scope**

The study was carried out in five phases through simulated isothermal, axisymmetric compression testing using the Gleeble and Dilatometer systems. All tests were conducted on continuously cast plant samples using the columnar grain structure of 436 FSS. Phase one simulated roughing rolling in 3-pass tests, varying inter-pass time and strain inputs. Phase two undertook the same tests but at higher strain rates, from 5 /s to 15 /s. Phase three simulated roughing rolling in 4-passes and analysed the effects of variations in strain rates and inter-pass times. Phase five looked into what

the variations in roughing rolling parameters; undertaken in phase one; had on the finishing rolling.

1.4 Aims and objective

The aim of this study was to improve the hot working of 436 in order to optimise the microstructures and textures which have a direct bearing on ridging resistance. In order to achieve this, the following objectives were drawn:

1. To investigate the effects of the starting microstructures from simulated roughing rolling (i.e. highly deformed versus partially recrystallised structure) on the evolution of the microstructures and texture during and after simulated Steckel finishing rolling.
2. To investigate the influence of thermomechanical processing parameters namely, inter-pass time, strain per pass and strain rates on the evolution of the microstructures and texture to encourage retained strain.

Chapter 2: Literature Review

2 LITERATURE REVIEW

2.1 Stainless steels

Stainless steels fall within the metal and alloys classification. Stainless steels are widely used in many applications that require high corrosion resistance. Stainless steels contain Cr above 10.5 wt%, which enables them to provide passivation for corrosion resistance [7, 22]. The passive layer imparts wet corrosion resistance and resists high-temperature oxidation [7, 17, 29]. A number of stainless grades are available in the market but for the purposes of this literature review, austenitic, martensitic and ferritic stainless steels are discussed. Note all alloy percentages are given as weight percentages in text, unless stated otherwise.

2.1.1 Austenitic stainless-steel systems

Austenitic stainless steels are characterised by high Ni and lower Cr contents compared to other grades. Cr additions generally range between 10.5-18% to ensure austenite phase stability [24]. Austenitic stainless steels have a characteristic face-centred cubic (FCC) structure at room temperature. The extension of the austenite phase (denoted by the Greek symbol-γ) to room temperature is sustained by adding elements such as Ni and manganese (Mn). When Ni is added to steels containing Cr, it retards the kinetics of the $\gamma \rightarrow \alpha$ transformation in the steel upon cooling, thus making it possible to retain austenite at room temperature. Adding C to the Fe-Cr system also extends the γ-loop that occurs in the binary diagram up to the maximum addition of 0.3% carbon. Nitrogen (N) is also a strong austenite former and is less likely than carbon to cause intergranular corrosion. Classical 300 series austenitic steels contain 8-10% Ni, with higher Cr and Molybdenum (Mo) grades requiring more Ni to stabilise austenite. To counter the market price volatility with the addition of Ni, Manganese (Mn) and N in partial replacement of Ni has seen newer austenitic grade developments [24].

Austenitic stainless steels are the most commonly exploited stainless steel due to their high formability and medium tensile strength and hardness [5,29, 30]. Austenitic stainless steels are readily fabricated and do not undergo a profound ductile to brittle transition common to martensitic and ferritic stainless-steel grades. They typically

sustain large deformations and undertake large plastic deformations imparted by their FCC structure [5, 29, 30]. Although ASSs exhibit good corrosion resistance, they are usually prone to stress corrosion cracking (SCC), making them undesirable for use in chloride and ammonia environments at warm temperatures [24]. ASSs are not known to suffer from ridging due to their low stacking fault energy, favouring recrystallisation over recovery [20, 31, 32].

2.1.2 Martensitic stainless-steel systems

Martensitic Stainless-Steels have low to moderate Cr and high C content, ranging from 12 - 16% Cr and 0.12 - 1.2% C with low Ni and rarely Mo. The C content is principally responsible for the high hardness of martensitic stainless steels after rapid cooling from the austenite region upon which, the C is trapped in interstitial sites straining the crystal lattice and imparting strength to the material. The lower Cr range limits the material's corrosion resistance. Martensitic stainless steels are very good for high wear resistance applications such as making of tool steels for cutting and surgical tools. Welding of martensitic stainless steels are not recommended due to the variation in cooling temperatures which would lead to the formation of unwanted microstructural products. Cold deformation is not favourable due to the high hardness and strength coming at the detriment of the material's ability to deform [29, 33, 34].

2.1.3 Ferritic stainless-steel systems

Ferritic stainless steels (FSS) have a characteristic body-centred cubic structure (BCC) at room temperature [22]. The stability of the ferritic phase (denoted by the Greek symbol α) is ensured in that Cr acts as a ferritic stabiliser by closing the γ phase loop in the Fe-Cr binary phase diagram, Figure 2-1.

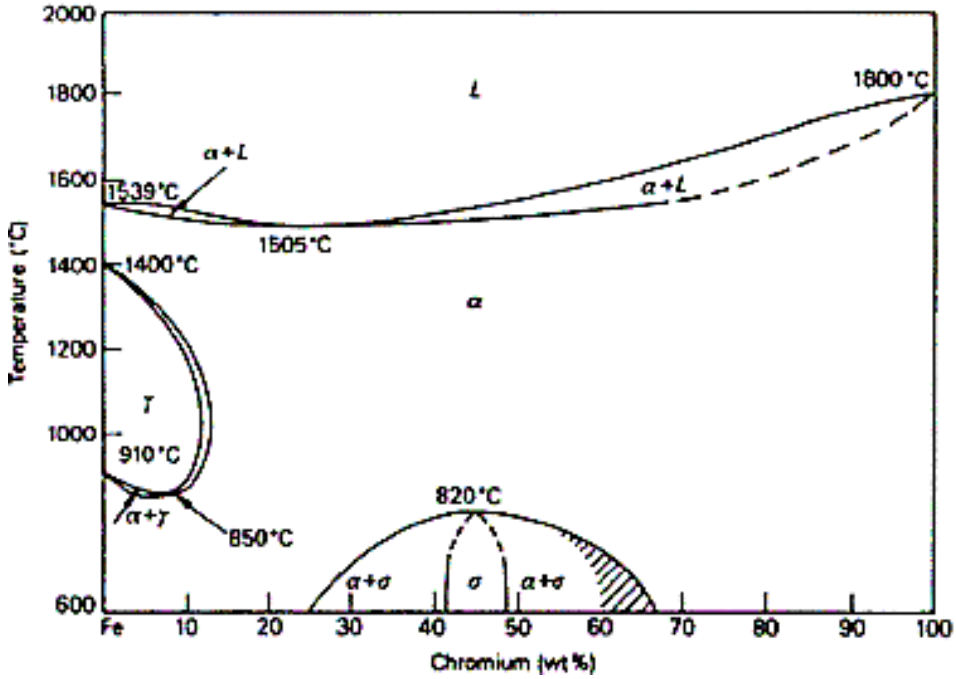

Figure 2-1: Fe-Cr binary phase diagram [25].

Based on the binary Fe-Cr phase diagram, Cr reduces the austenite loop such that above 13% Cr, only ferrite exist across all temperature ranges. FSSs have low to no Ni, low C, around 0.12%, and contain 10.5 – 29% Cr [22]. Ti, Zirconium (Zr) and Nb can act as additional ferrite stabilisers as they remove C and N from the solution to form carbonitrides [22]. Adding Mo in 436 and 434 grades enhances resistance to localised corrosion. Higher Cr ferritic alloys have excellent corrosion resistance, which is improved by adding Mo (1 – 2%). Based on composition, FSSs can be classified into either three standard or two special groups [7, 26].

Group 1 of standard ferritic grades have the lowest Cr contents (10-14% Cr). Group 2 of FSSs have Cr contents ranging between 14 - 18% Cr and is the most widely used family of FSS. C is kept low between 0.02 – 0.05% to improve ductility. Increasing C content results in dual-phase austenite and ferrite phase at high temperatures, which results in a duplex structure upon rapid cooling. Group 2 grades of FSS exhibit higher corrosion resistance and can replace 304 austenitic grades for corrosion resistant applications. Group 3, standard FSS types, have 14 – 18% Cr and are stabilised ferritic steels with Nb or Ti. Group 4 forms part of the special ferritic groups, with grade 436 stainless steel forming part of this group. They contain 10 - 18% Cr with Mo additions greater than 0.5% to enhance pitting corrosion resistance. Group 5 special FSS have

Cr contents above 18% and have Mo additions of about 3% for wet corrosion resistance and Cr in the 25 - 29% range and can rival Ti in applications where severe corrosion-resistance is required [7, 26].

FSS grades do not undergo phase transformation and are therefore prone to grain growth and 475°C embrittlement related problems. FSSs have stronger plastic deformation strength than austenitic but work harden less, making tensile strengths lower than austenitic stainless steels. Finally, FSSs experience non-uniform texture, which leads to heterogeneous mechanical behaviour and as such, ridging is observed [8, 11, 14, 27, 28].

FSSs with high Cr content are vulnerable to forming sigma phase below 600 °C, which results in embrittlement. FSSs are usually quenched from above 600 °C to prevent the formation of embrittling phases. The main advantage of FSS over their versatile austenitic counterparts is cost, as most do not have expensive Ni additions. The market for ferritic stainless steels subsequently increased during the first decade of the 21st century due to the volatility in Ni prices, their bright surface finishes and magnetic properties [5, 7, 29, 30].

2.1.3.1 436 Ferritic stainless steel

Grade 1.4526, or ASTM 436 FSS, is a Nb-stabilised, Mo (1%) containing steel alloy. It has a Cr content of 16% and N below 4% [29]. Cr allows for the passivation of the protective film under aerobic conditions. Cr stabilises ferrite and increases yield strength. Furthermore, it increases heat resistance and high-temperature scaling. Mo passivates better than Cr as a protective film at lower additions. Mo substantially increases corrosion resistance in acidic and anaerobic environments. Mo is a ferrite-stabilising element and increases material strength. Carbon is kept as low as possible as Cr and C generally bind, resulting in intergranular corrosion. C also acts as an austenite stabiliser. N enhances the passivation film reaction and it acts as the only austenite stabiliser that increases the pitting resistance equivalent (PREN) of the steel. However, it is difficult to add N as a solute element in molten metal.

ASTM 436 FSS has excellent corrosion resistance and is not prone to SCC due to their low Ni contents as typically depicted on Copson curves. 436 FSS grade is widely

used in shaping applications such as automotive trimmings, architectural decorations and exhaust systems of cars.

2.1.4 Other stainless-steel systems

To overcome the short falls associated with ASS, FSS and MSS, there has been the development of dual phase stainless steel grades or grades that undergo phase transformation to improve the properties. These contain either austenite and ferrite or austenite and martensite. Stainless steels that are strengthened through precipitation are also available.

2.1.4.1 Duplex stainless steel

Phases present in duplex stainless steels are constituted of ferrite and austenite, with not less than 30% each. These are steels that consist of low C with Cr content ranging between 22 and 26%, Ni 1 and 7% and additions of Mo. Duplex stainless steels can use N for austenite phase stabilisation; the chemical additions extend the austenite-ferrite loop, Figure 2-1 [7, 24, 30].

Due to their high Cr contents (>20%), they have relatively high stress corrosion cracking (SCC) resistance. In addition, they have increased high temperature strength due to the high Ni content [7, 24].

Duplex SS are however susceptible to intergranular corrosion due to intermetallic precipitation of chi, sigma and Cr-nitride phases, which can be suppressed by controlled processing, limiting their service temperatures between -40 and 300 °C. Duplex SS have attracted a lot of attention in applications that require increased corrosion resistance and good weldability [7, 30].

2.1.4.2 Precipitation hardening (PH) stainless steel

These steels typically contain 15 to 17% Cr, 4 to 8% Ni contents, and up to 5% Cu in terms of mass. Mo additions are low. The material is generally martensitic in nature and precipitation is achieved at high temperatures through the formation of fine precipitates such as Cu rich phases, NiAl particles and Ni_3Ti precipitates. Precipitates essentially impart strength to the material by impeding dislocation movement. PH

stainless steels have uses in aerospace, marine equipment and applications where strength, toughness and corrosive resistance is needed [7, 38].

2.2 Texture in ferritic stainless steel

Texture analysis after thermomechanical processing of steels provides metallurgical information on deformation, recrystallisation and phase transformation that are useful in improving the material's properties

Figure 2-2 shows how grains can have different orientations within a rolled material. Some polycrystalline materials have random distributions of grains that average each other to behave in an isotropic manner while others have preferential crystallographic orientations due to manufacturing processes. This phenomenon is known as texture and it impacts heavily on the materials properties [31, 32, 33].

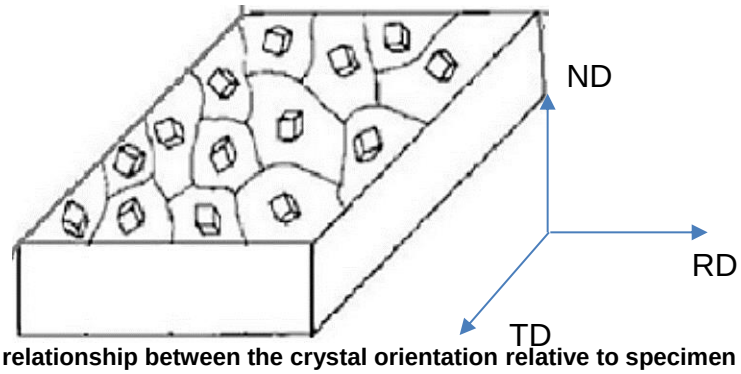

Figure 2-2: Depiction of the relationship between the crystal orientation relative to specimen orientation [34].

Grain orientations can be represented using Miller indices for the sheet plane and rolling direction. With this convention, {hkl}<uvw> refers to grains having a crystallographic plane {hkl} parallel to the sheet surface and crystallographic direction <uvw> parallel to the rolling direction [22].

The processing of FSS has favoured specific orientations aligned with specific sheet directions. It has been shown that the spatial orientation distribution in the RD–ND and TD-ND sections exhibits inhomogeneity but no alignment giving rise to different textures such as Gamma and Alpha in FSS [35, 13]. Alpha fibres are a family of fibres with orientations having <110> directions parallel to the rolling direction (RD) and associated with cold-rolled textures. Gamma fibres are orientations with {111}

planes/directions parallel to the normal direction (ND) and are associated with the recrystallised texture [22].

Other specific texture orientations of importance include rotated cube – {001} <110> and Goss – {110} <001>. Rotated cube textures and those close to them exhibit strong resistance to recrystallisation, whilst Goss orientations are associated with high shear deformations. The major texture components can be found by taking a section through the Euler space at $\varphi_2 = 45°$ [22], Figure 2-3.

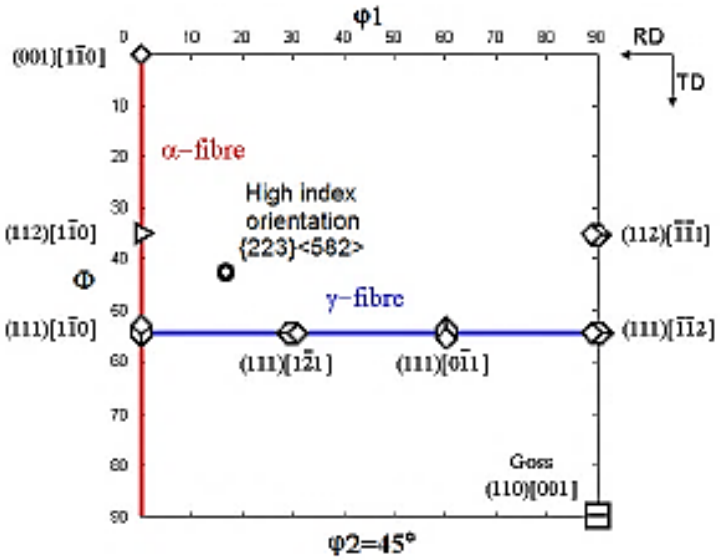

Figure 2-3: Euler space section through 45° for orientations of relevance in BCC unit cells [22].

2.2.1 Techniques for texture characterisation

Depending on the technique employed, the texture may be classified as macrotexture when X-ray or neutron diffraction-based techniques are employed or microtexture when electron diffraction such as SEM-EBSD are used. Due to the high transmission of neutrons, neutron diffraction is efficient for the analysis of bulk texture for polycrystalline materials. Neutron diffraction is a well-established technique for understanding deformation and recrystallisation textures of a material. It makes use of pole figure measurements of coarse-grained materials in a non-destructive manner and can be used as a means of comparative analysis for samples under different conditions. Neutron diffraction set-ups can undertake texture analysis at temperatures above 1000 ºC and textural evaluation under an applied load [36, 37].

During neutron diffraction, two reference frames are defined, one of the specimen's and the other for the crystal. The distribution can essentially lead to pole figures or inverse pole figures under different conditions. Texture is quantitative, where there is a reliable information about a statistically significant number of grains [44, 45]. Neutron or synchrotron facilities are available but are specialised and not as easily accessible. Neutrons can be generated in a nuclear reactor or an accelerator. Neutrons, can penetrate larger depths and larger grains can be analysed due to large specimen capability. Neutron diffraction techniques are generally seen as bulk measurement techniques as opposed to near surface techniques such as electron and X-ray analysis [38].

X-ray mapping is a technique that can provide textural data to a resolution of 10 µm. It is based on the energy dispersive spectrometry and can be used for material characterisation, providing simultaneous texture mapping and imaging X-ray micro-fluorescence on a grain scale [39]. It must be noted that the XRD technique does not penetrate the bulk as in neutron diffraction but only surface grains are considered in this technique. X-rays are capable of analysing grains up to 0.2 mm in size [38].

In analysis where, larger grains are scanned the electron analysis technique such as SEM-EBSD is preferred. With a SEM, the surface is examined with an electron beam at a specific scanning rate, and the reflected beam of electrons is collected and displayed at the same speed on a cathode ray tube. The surface will need to be polished or etched, and samples must be electrically conductive. A conductive surface layer can be applied on the surface for nonconductive materials. Magnification can range from 10 000X to 50 000X [31]. EBSD allows for understanding the orientation of grains in a sample that has been suitably prepared. The spatial resolution is taken generally as one tenth of the average grain size. Information about the grain size, shape, crystal structure and phase boundaries can be evaluated. During the process, when an electron beam is exposed to surface at an inclination, backscattered electrons diffract, these diffracted electrons are caught on a screen, with each crystal structure having a diffraction pattern that is unique. Although EBSD facilities, have become widely available, X-ray pole figures remain a cost effect method to quantify preferred crystallographic orientation [22].

Historically, orientation distribution functions and pole figures were key to understanding material texture. The axes of the orientation distribution functions are given by Euler angles that characterise individual orientations. Where a statistical function is used to define orientation distributions present. As Euler angles require three angles to be defined, orientation distributions exist in a three-dimensional space that show the variation in orientation intensity with respect to these parameters.

Pole figures defines planes with high atomic densities detected by diffraction data and shows variations in diffraction density. Pole figures can be generated through back reflection. Pole figures are typically plotted on stereographic or equal area projections to represent directionality [38]. Critical to interpreting these projections is considering the x axis as the rolling direction, and contrary to typical plotting of these projections is the normal direction is taken as the y axis. For a particular orientation, the axis will show the highest intensity when that orientation aligns with that particular axis, for example in the Figure 2-4 the 101 plane is aligned to the normal direction.

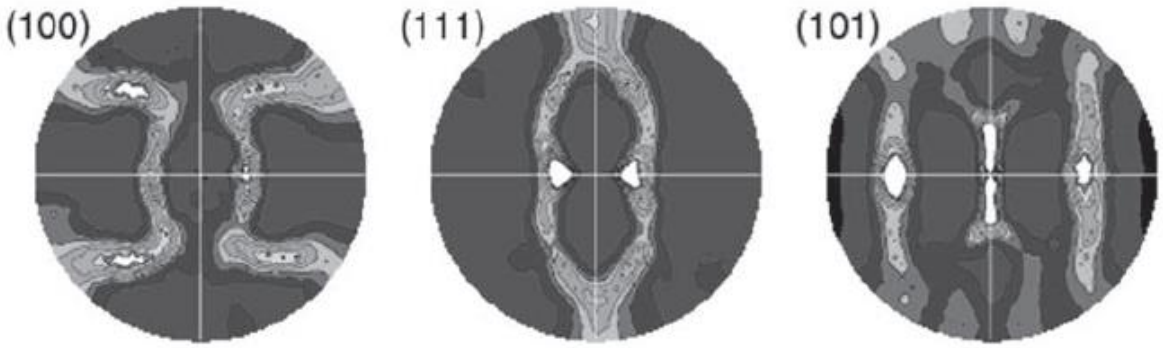

Figure 2-4: Pole figure for rolling texture typical of FCC metal, where RD points to the right, and ND out of the surface [38].

2.3 **Ridging**

Ridging and roping have previously been used interchangeably for surface roughening in aluminium and ferritic steels. More recently, roping has been reserved for surface roughening developing during the stretching of aluminium products, whilst ridging has been reserved for the phenomenon related to FSS [22]. However, the phenomenon of roping and ridging are similar. They both occur as a result of forming or stretching, with troughs and ridges running along the rolling direction, and they produce

roughness characteristics larger than the sample's microstructure [40]. Roping occurs when tensile stretching is imposed along the transverse direction, whilst ridging manifests mainly when tensile elongation is imposed along the rolling direction of the sample. Furthermore, ridging tends to form corrugations along the transverse direction of the sheet material, whilst roping does not show correlations between the top and bottom surfaces. This difference would lead to the belief that ridging is a through-thickness phenomenon, whilst roping is a near-surface phenomenon [22].

Ridging can be explained visually as a roughening of the sheet surface manifesting after a processing condition such as deformation, annealing or cold rolling. A wave like surface manifests with the crest being the peak and the trough being the deepest point in the surface. The surface troughs and crests run lengthwise along the rolling direction of the sheet after tension is applied through processes such as deep drawing along the rolling direction [40, 41]. As ferritic stainless steels tend to be exploited for their visual properties, these manifestations are detrimental to their purpose as shown in Figure 2-5 and Figure 2-6.

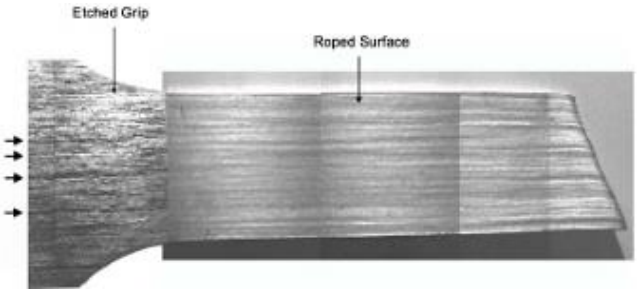

Figure 2-5: Relation between etched bands and ridged surfaces following tensile testing along the RD of a Ti-stabilised FSS [40]

Figure 2-6: Ridging on an AISI FSS sink [41].

The depth of the crests and troughs is linearly dependent on the tensile strain applied to the sheet [40]. Furthermore, these crests and troughs form more severely based on the direction along which the tensile test is taken, with maximum amplitude measured when tensile strain is applied along the rolling direction of the sample. The amplitude of ridges at 15% tensile strain can amount to 10 - 50 micrometres in length [22, 23]. The period, or distance between crest and crest or trough and trough, can be qualitatively defined between 1 - 5 millimetres. The length of these ridges running along the rolling direction can be several centimetres. These measurements underpin that ridging manifests on a scale much larger than the grain size of the sample, but microstructure significantly influences the ridging behaviour of the sample. Ridging is not manifested on one surface alone as it displays correlations between the top and bottom surfaces of the sheet material and can be described as corrugations, along the TD direction of the sheet. This means that at a certain point on the surface, a peak, on the top surface would correlate to a trough on the bottom surface and vice versa as shown in Figure 2-7. Therefore, it is the internal crystal structure manifesting as the surface irregularity [15-18].

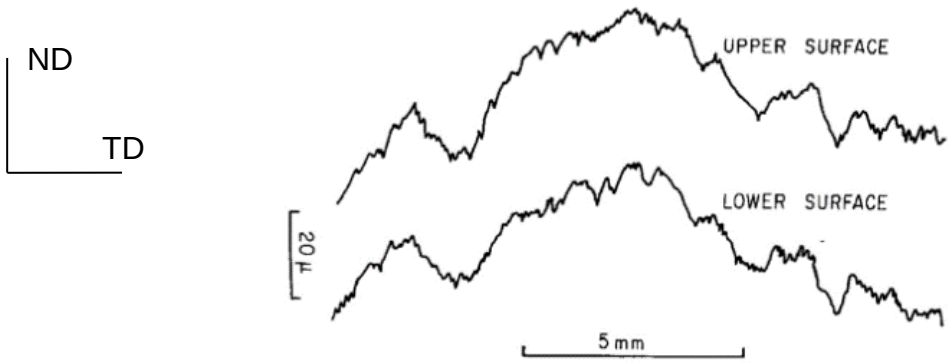

Figure 2-7: Relation between the top and bottom sheet surfaces of FSS that have undergone ridging [14]

2.3.1 Effect of texture on ridging and roping

Ridging is accepted as plastic anisotropy by regions with grains having a particular crystallographic orientation. These grains have similar deformation behaviour due to the alignment of their orientations, resulting in deformation patterns more significant than the size of individual grains [40].

Three models have been proposed by Chao [11], Wright [42] and Takechi [14], respectively to explain ridging in FSS. Chao was the first to introduce the idea of microtexture to explain ridging. In his model, he claimed that FSS microstructure could be defined as bands of “Cube on Face” grains - {001} <110>, in a “Cube on Corner” grain - {111} <110> matrix. Cube on Face grains deform in plain strain, extend along the RD, and contract along the ND. On the other hand, Cube on Corner grains tend to deform in plain strain with zero strain along the ND and contraction in the TD [11]. Contrary to real-life experience, this predicts a ribbed profile instead of a corrugated surface profile on the sheet as shown in Figure 2-8.

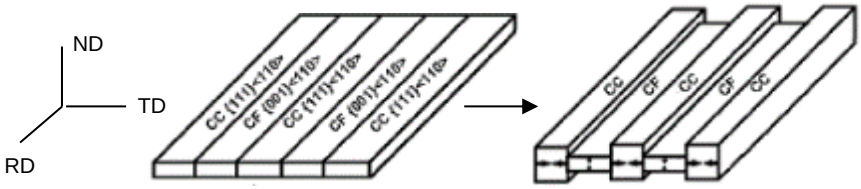

Figure 2-8: Depiction of the Chao model schematically manifesting a ribbed profile expected on a sheet surface after deformation [11].

Wright proposed a model whereby inhomogeneous buckling among grains resulted in ridging. Here, bands of {001} <110> were assumed to be embedded in a matrix of {111} <112> grains. As with the Chao model, the {001} <110> does not contract in the TD upon deformation along the RD. Instead, the {111} <112> will contract along the TD, {001} <110> grains will buckle in-homogeneously as presented in Figure 2-9. Although the model produces the correct ridging profiles, computer model simulations show buckling would not be expected [22, 43].

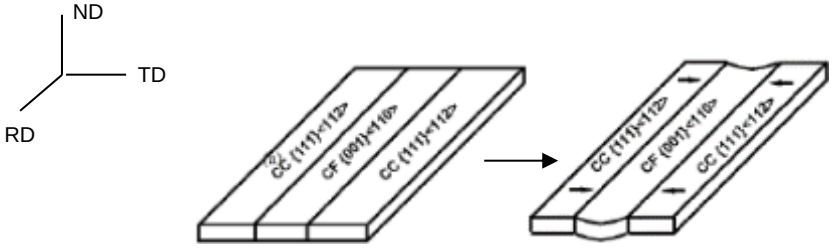

Figure 2-9: schematic representation of the occurrence of ridging as explained by Wright [42].

Another setback of both the Chao and Wright model is their requirement for a substantially large amount of {001} <110> oriented grains, which is not an observation in real-life experimentation of final sheet texture [22, 44].

The Takechi model, set forth at a similar time as the Chao model, considers alternating clusters of {111} <110> oriented grains. Bands are said to be occupied by these grains at 180° rotations about the ND. Upon tensile stress, three slip systems are activated in each grain. The two slip systems cancel each other out, whilst the third system creates an out-of-plane shear (shearing in the ND-RD plane along the ND), leading to a crystal rotation [45]. As bands are in opposite directions, they rotate in opposite directions leading to a corrugated profile. Takechi's model has been validated through simulation; however, it is criticised as an oversimplified model [22].

A fully quantitative description of grain orientation within a band tends to be difficult as each grain within a band assumes a particular orientation. The spread of bands clustered together within ranges of 10 - 20° along the TD is smaller than the wavelength of ridging observed. A complex mix of grains poses a dilemma when considering ridging based on the simplified models referred to above. To fully account for ridging behaviour in a material, microtexture analysis needs to be incorporated into computer finite element modelling software where simulations can model the material behaviour from deformation to the formation of preferred orientations during recrystallisation. This allows for predictions of the microstructure on a much larger scale [15, 17].

As clusters of grains are not found on the sheet's surface, it is predicted that the centre layer of the sheet contributes most significantly to ridging [22, 46].

2.4 Recovery, recrystallisation and grain growth in ferritic stainless steels

Most of the energy stored from deformation is in the form of dislocations. About 5% of the energy applied is stored as strain energy around newly formed dislocations. Majority of the deformation energy is dissipated as heat. The stored energy serves as a driving force for softening, which can be grouped into three stages; recovery, recrystallisation and grain growth as shown in Figure 2-10 [22, 39].

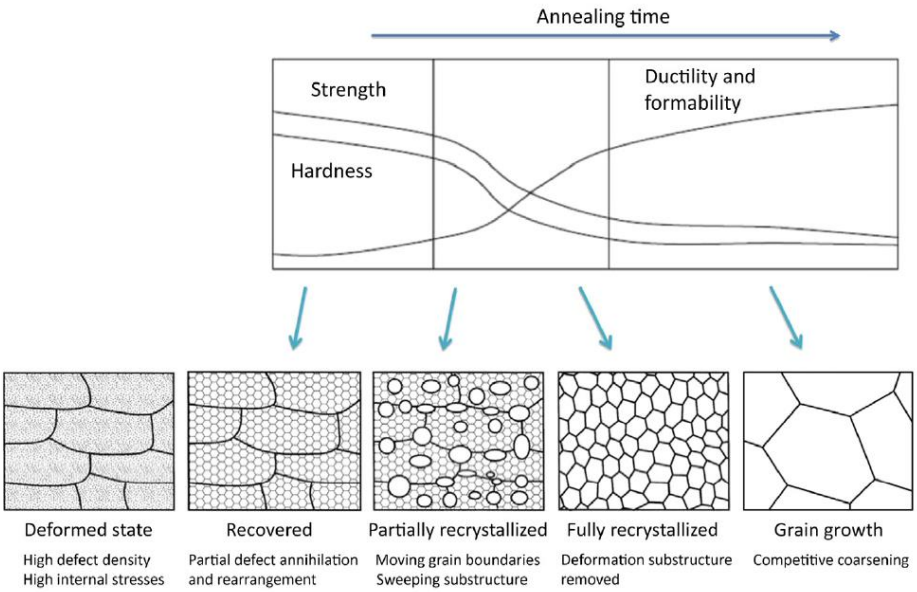

Figure 2-10: Schematic of steps involved in the softening process [18].

Recovery is the process when deformed grains in metals or alloys reduce their stored energy by the removal or rearrangement of defects in their crystal structure after being exposed to temperatures approximately half or a third of its melting point. During recovery, the internal energy is relieved through annihilation and rearrangement of dislocations that move through diffusion. During recovery, dislocations reorder and form sub-grain structures with low angle grain boundaries. Recovery does not involve the motion of high angle grain boundaries, but rather dislocation and low angle grain boundary rearrangement within the deformed microstructure and takes place at lower temperatures than recrystallisation [22, 39].

Recrystallisation is a process where deformed grains are replaced by undeformed grains of a minimum critical size nucleates and grow within the deformed microstructure, until a new undeformed microstructure remains. Recrystallisation is achieved through the supply of sufficient thermal activation to the deformed material. Recrystallisation is concerned with the formation and motion of high angle grain boundaries. The new grains have lower overall dislocation density, similar to pre-cold worked conditions. The reduction in strength and hardness during recrystallisation is far more significant than with recovery [32, 18, 31]. Recrystallisation is diffusion controlled and it is, therefore, a temperature and time dependent process. Plastic deformation is usually carried out at temperatures above the recrystallisation

temperature in a process referred to as hot working. The material remains soft as it cannot strain harden, and a large amount of plastic deformation is possible, this can result in dynamic recovery or recrystallisation, discussed in Section 2.4.2. From classical nucleation theory, recrystallisation has been seen as having a specific nucleation phase, where strain free grains of small dimensions form. A defined discontinuous method of recrystallisation occurs when microstructural inhomogeneities are present, such as heavily distorted grain boundaries, heterogeneous strain gradients and high lattice curvature in the vicinity of hard second phase particles or areas with high dislocation densities such as shear bands [22, 39].

Recrystallisation has been proposed to occur during annealing after deformation through one of two mechanisms, selective growth and oriented nucleation. In the concept of oriented nucleation, it is believed that some grain orientations nucleate preferably to other grain orientations and these preferentially oriented grains play a role in final recrystallisation. This means that the final microstructure would always have a preferred final orientation in a material, and a certain texture will always prevail. On the other hand, selective growth proposes that specific nuclei growth is preferred due to certain misorientation relationships within the matrix it nucleates, which suggests that the final microstructure is a function of the microstructure preceding it [4].

Grain growth occurs when the mean grain size increases, resulting in in an overall decrease in grain boundary area per unit volume after exposure, of a polycrystalline material, to high temperatures. During recrystallisation, grain growth occurs in the recrystallised equiaxed crystal structure. The driving force is the reduction in internal energy due to lowering the total grain boundary surface area. Larger grains grow at the expense of smaller grains through competitive capillary driven grain coarsening [22, 39, 40, 55]. Nucleation of grains through recrystallisation is favoured through abnormal sub-grain growth. During abnormal grain growth, a few grains grow at the expense of smaller grains, resulting in a bimodal distribution of grain sizes. When the grains are large enough, grains impinge on each other and normal grain growth occurs. Abnormal grain growth is characterised as a discontinuous process [47].

Recovery and recrystallisation are driven by lowering the internal stored energy. Therefore, they are seen as competing mechanisms for softening in a material. In fact, the effects that they have on refining the material texture differs. As recovery affects in-grain sub-grain and dislocation networks, it would lead to no change from the original internal texture [18]. This makes breaking down unwanted textures difficult, because if the material is completely softened through recovery, no change in the texture can occur. This is shown in Figure 2-12 for a low-C steel typically having high stacking fault energy, where no change in texture occurs during recovery after 5 and 6 seconds. This is unwanted in FSS as elongated recovered grains within a recrystallised microstructure is undesired leading to inhomogeneous plastic flow and ridging [48].

2.4.1 Textures associated with dynamic recovery & dynamic recrystallisation in ferritic stainless steels

Recrystallisation can occur through the mechanism of particle simulated nucleation (PSN). This type of recrystallisation acts as a means of randomising the recrystallisation texture. Non-deformable precipitates are elastically much harder than the matrix acting as an obstacle to dislocation motion. After large deformations, around non-deformable coarse precipitates (> 0.1 µm) a high degree of lattice curvature and strain between the precipitate and the matrix occurs, called deformation zones [22, 40]. These are favourable sites for nucleation during recrystallisation. 436 ferritic Nb-stabilised steel is known for precipitation of laves and NbC precipitates which could act as sites for PSN [49]. In Nb-ferritic stainless steels, 1 µm precipitates were found to play a significant role in nucleation of randomly nucleated grains as shown in Figure 2-11. Research points to the need for a dense and fine dispersion of precipitates to ensure a randomised texture of the matrix [50]. It should be noted that there is research that points to evidence of PSN resulting in preferred orientations being nucleated, however this was not the focus of this study [51].

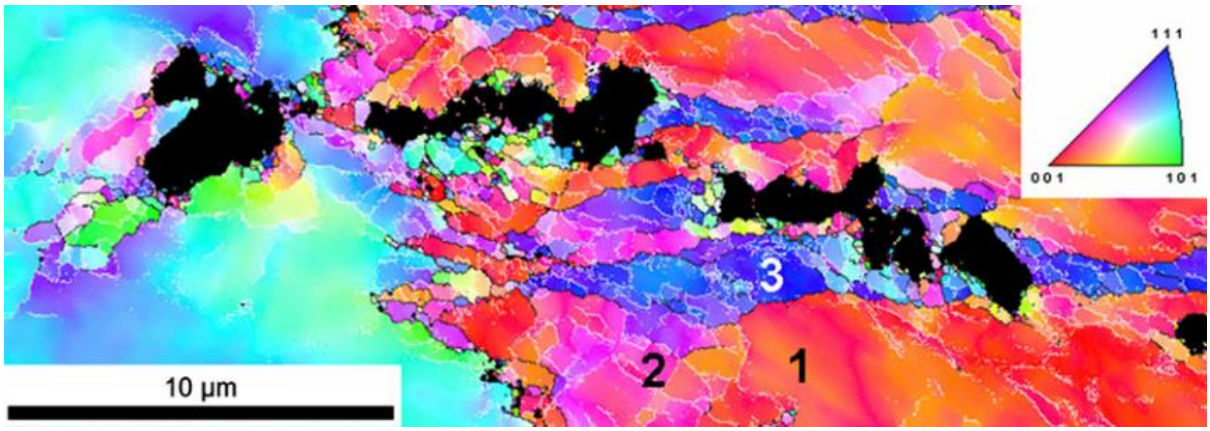

Figure 2-11: Nucleation of random orientated grains during PSN as observed by Siqueira et al [49].

During recovery, Gamma fibres exhibit a high degree of internal sub-grain misorientation within the grain compared to Alpha fibres. Gamma fibres can accommodate a high degree of stored energy in the form of dislocation density through a high degree of curvature. Alpha-fibres have low stored energy and undergo recrystallisation through strain-induced boundary migration (SIBM). At Alpha-Gamma grain boundaries, growth tends to occur within the Gamma grain consuming the neighbouring Alpha fibre cell and reducing the overall stored energy. A growth advantage of specific orientations is found, pointing to selective growth. However, the phenomenon is limited compared to abnormal sub-grain growth in plain Gamma fibre grains [14, 1, 61].

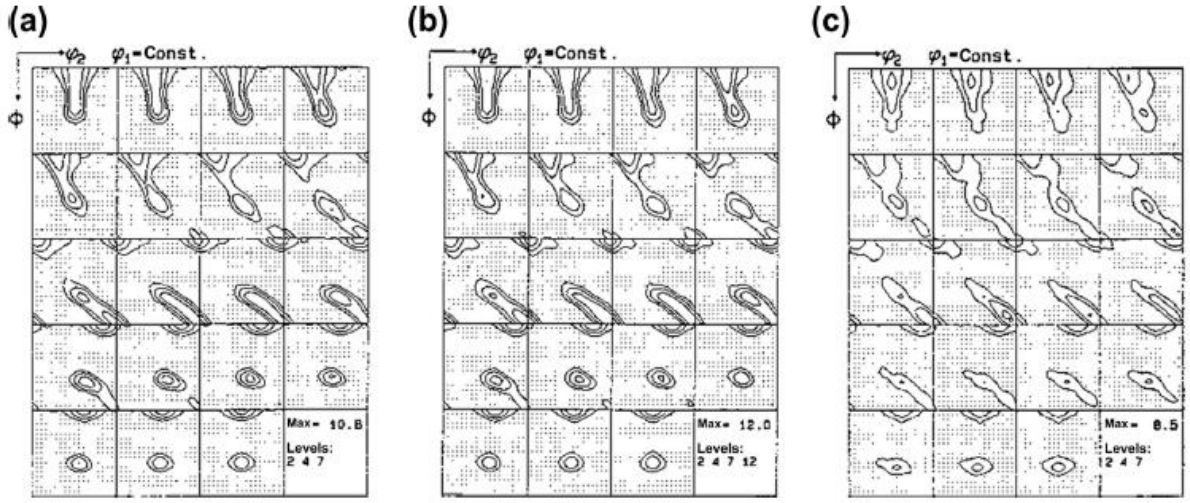

Figure 2-12: XRD ODF maps of 90% cold rolled steel at 1000 K after a) 5s; b) 6s; and c) 7s [44].

2.4.2 Dynamic recovery & dynamic recrystallisation in ferritic stainless steels

Recrystallisation and recovery occurring during deformation are called dynamic recovery and recrystallisation, respectively.

Dynamic recrystallisation occurs during hot deformation and occurs through three mechanisms namely, discontinuous dynamic recrystallisation (DDRX), geometric dynamic recrystallisation (GDRX) and continuous dynamic recrystallisation (CDRX) [52, 53]. Discontinuous dynamic recrystallisation occurs through nucleation and growth of new grains during deformation [22, 63]. The competing recovery mechanism in FSSs makes it difficult for DDRX to occur due to cross-slip and climb of the deformed structure, reducing stored energy and thus the driving force of recrystallisation. GDRX occurs under high strains (> 1), where original grains are broken into new recrystallised grains. During CDRX, the misorientation of low-angle grain boundaries increases as dislocations move during DRV. No nucleation of new grains is required. The dislocations accumulate at low angle grain boundaries, increasing misorientation, forming high angle grain boundaries. When grain boundaries increase in misorientation, they gain mobility, and pass over the deformed structure, lowering the overall strain. DRX studies are essential for refining microstructure in FSS as no phase change occurs and significant refinement potential is offered [20, 22, 28].

A further factor of importance in defining the work-hardening is the strain rate on the sample. It has been shown that increase in strain rate leads to increased work hardening in FSSs under low applied strains [54]. The flow stress of high-Cr FSS increases with lower deformation temperature and increasing strain rate. At low strain rates, however, where DRV occurs, the material softens faster than work hardening, and the flow stress remains constant with strain, reaching a steady state. For dynamic recrystallisation, the material work hardens until maximum flow stress is reached with strain, after which softening occurs and eventually a steady state is reached, which is common in CDRX [55]. During laboratory studies of dynamic recrystallisation, strain rates and temperature tend to be kept constant for a deformation pass [20, 23]. It is then useful to incorporate the influence of temperature and strain rate into a single

factor called the Zener Holloman parameter. The Zener Holloman parameter, Z, is defined as the temperature-compensated strain rate [56] and is given by:

Equation 2.1:

$$Z = \dot{\varepsilon} e^{Q/RT}$$

where $\dot{\varepsilon}$ is the strain rate, Q is the activation energy for deformation, R is the universal gas constant and T is the temperature in Kelvin.

It is typically found, for low Z values, multiple flow stress peaks occur, whilst high Z values tend to find flow stress behaviour exhibiting a single peak. With low Z values, the critical strain required for recrystallisation is lowered [16, 19].

It has been shown in works by Mehtonen [20, 55] that the dynamic restoration mechanism in high-Cr (21% Cr) FSSs depends on the Z value under strain rates between 0.1 to 10 /s and in the temperature ranges of 950 to 1050 °C. Tests showed that a steady state was reached after initial work hardening, typical of a material undergoing DRV. Under high Z values, the primary restoration mechanism is DRV, with higher strains favouring GDRX and CDRX followed by SRX. Medium Z values showed the primary restoration mechanism as DRV and CDRX with possible DDRX. Under low Z, DRV was extensive, with CDRX occurring; however, CDRX did not produce a drop in flow stress curves due to the limited fraction of new grains formed [53, 55]. A different study into ferritic Fe also showed that DRX occurred under low Z values and DRV under high Z values [57].

Dynamic recovery has been shown to dominate higher temperature deformations during hot rolling, whilst lowering the deformation temperature encourages a highly strained state within the microstructure [52]. In addition, the number of low-angle boundaries within grains increases with decreasing hot deformation temperature from 950 to 650 °C.

2.4.3 Dynamic recovery of ferritic stainless steel

Recovery results in the rearrangement and annihilation of dislocations into sub-grain or cell boundaries [18]. When this process occurs during deformation, it is termed as dynamic recovery. Dynamic recovery is aided by temperature, increasing the motion

of dislocations formed during deformation into low-energy dislocation structures as shown in Figure 2-13 [58]. The primary mechanism linked to dynamic recovery has been linked to the ability of a material to cross-slip [32]. In FSS, DRV is the primary softening mechanism at high temperatures due to the high stacking fault energy. This reduces the stored energy for driving static recrystallisation as it reduces the energy imparted during deformation [59]. Dynamic recovery is high at high deformation temperatures and reduces stored energy, hence the driving force for SRX [19, 27]. Decreasing deformation temperature usually increases work-hardening, which points to a lowering DRV rate. Increasing deformation temperatures results in increased dynamic recovery of grains. DRV reduces the number of low-angle boundaries or dislocations within the grain [52].

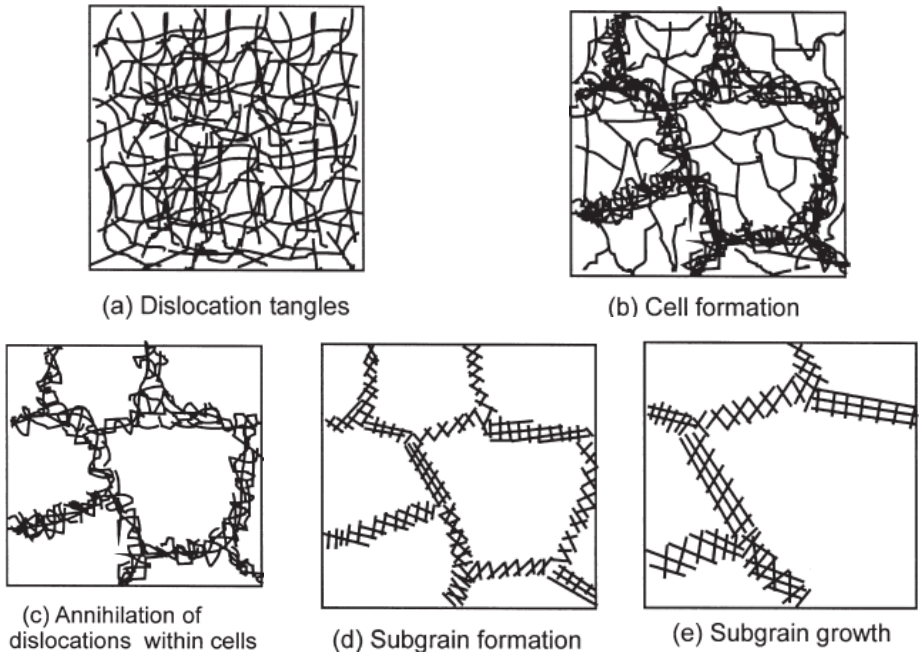

Figure 2-13: Stages of recovery following plastic deformation [60].

2.4.4 Dynamic recrystallisation in ferritic stainless steels

Studies to encourage texture randomisation through increasing the driving forces for recrystallisation in FSSs are vast [4, 9, 27, 66, 69]. The SRX during hot rolling of FSSs can be promoted by increasing strain or inter-pass time or by using intermediate rolling temperatures that are high enough for recrystallisation but low enough to prevent dynamic recovery [6]. Studies to lower the finishing pass temperature in order to

increase the amount of stored energy from dislocation density coupled with lower temperatures to limit the recovery have been undertaken in FSSs [19, 27]. Braga found that deformation in the first passes should be undertaken at high temperatures to promote static recrystallisation, whilst the final rolling should be done at lower temperatures to promote work hardening which subsequently favours recrystallisation upon annealing [61]. Mehtonen found that lowering the finishing temperature increased the flow stress and the sub-grain boundary density through the formation of in-grain shear bands in <111>//ND grains [52].

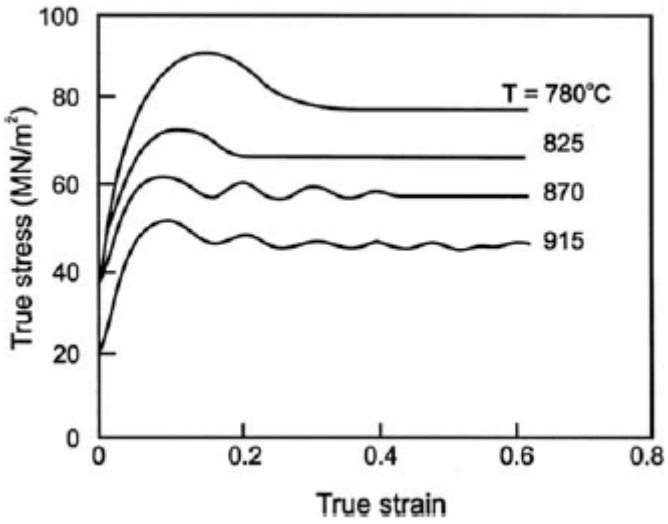

Figure 2-14: Hot compression curves taken at various temperatures under a strain rate of $1.3 \times 10^{-3} s^{-1}$ [62]

During dynamic recrystallisation, the stress strain behaviour exhibits a single peak as shown in Figure 2-14. Low Z parameters (low strain rates and high temperatures), leads to multiple peaks in the stress-strain curves. In order for dynamic recrystallisation to occur, a minimum strain is required. The strain required to initiate dynamic recrystallisation decreases with the Z parameter [63].

2.5 Thermomechanical processing of ferritic stainless steels

2.5.1 Effect of continuous casting on microstructure and texture of ferritic stainless steels

In steel production, the cast structure influences the evolution of the microstructures in the successive processing stages, such as hot rolling. For instance, ridging is known to be related to the as-cast microstructures [22, 23].

Depending on the casting conditions employed, a cast structure can either be equiaxed, columnar or a combination of both. During solidification, nucleation of grains starts from the mould wall due to the lower temperatures experienced. This creates a fine-grained structure due to high nucleation rates from lower temperatures. Alongside this, columnar grains form due to directional cooling from the centre of the slab. At the centre of the mould, or in this case the slab, a more isotropic structure of equiaxed grains of a few millimetres in length forms with a weak random texture.

The columnar grains are strongly textured with {001} plane parallel to the casting direction- {001}<uvw> [61, 22]. Braga and Hamada (2003) cited that it was particularly the {001}<uv0> for FSS [64]. Takeuchi, also states that in order to decrease ridging, a ratio of equiaxed to columnar grains needs to be a minimum of 50% [65]. Itoh et al. [66] found that for FSS, the equiaxed ratio of 50% could be achieved through electromagnetic stirring and by controlling the superheat of liquid steel to within 15 to 25 ºC, improving the ridging of the final cold rolled sheet [67].

Columnar grains with cube orientation are very difficult to deform and recrystallise uniformly. As a result, columnar grain regions exhibit a higher degree of ridging after hot rolling, cold rolling, and annealing than the equiaxed grain regions [23]. The main contributor to ridging is the strong {001}<110> component arising from the {001}<uvw> texture in columnar grains. This {001}<110> component is difficult to breakdown through deformation and annealing instead it results in elongated grains. The reason is that these grains have lower Taylor Factor and lower dislocation density consequently leading to texture banding and susceptibility to ridging [17, 18, 24, 27]. The Taylor Factor is given by the relative amount of work required to deform differently orientated grains to the same strain assuming an equivalent critical resolved shear

stress. Where high Taylor Factor grains are found to have the ability to accommodate higher dislocation densities and overall greater strains [68].

2.5.2 Effect of hot rolling conditions on texture of ferritic stainless steels

Hot and cold rolling are two types of forming processes. Hot rolling occurs when a material is deformed at high temperatures whilst cold rolling is conducted at low temperatures. It should however be noted that temperatures during cold rolling can be significantly high due to energy inputs from straining [39, 40, 63]. Hot rolling usually allows for significant deformations, with lower energy inputs than cold rolling due to the reduction in the material's ability to strain-harden above the recrystallisation temperature [31]. Warm rolling is a controlled rolling process that generally takes place at temperatures between phase transformations, i.e., between Ar3 and Ar1 temperature. A high resistance to deformation occurs due to the lowered temperature limiting its application [69].

For FSS, most often, the surface of hot band samples consists of recrystallised grains elongated along the RD, with a large grain size distribution. Texturally the main components in the hot band are Goss with minor elements of {112}<111>. The centre of the sheet tends to be highly elongated and recovered with significant Alpha fibre components of {001}<110> and {112}<110>, though weaker Gamma fibres are also present [22]. Mehtonen [20] stated that to achieve good deep drawability in the finished sheet, the formation of uniform Gamma fibre is essential from SRX during inter-pass time and subsequent annealing of the hot band [28, 62]. Ridging has been found on the sheet directly after hot rolling, implying the cause of ridging is a function of not only cold rolling and annealing processes in the plant, but processes prior to hot rolling itself. Based on crystal plasticity simulations, the hereditary nature of texture from upstream manufacturing processes contributed to ridging. In research by Lefebvre [22] it was hypothesised that CDRX during hot rolling favours Alpha fibre orientations that adversely affect ridging properties [22].

Long inter-pass times, of 8 - 20 s, are typical in reverse mill set ups. Long inter-pass times lead to static recrystallisation if the steel does not form precipitates prior to recrystallisation. If the steel forms precipitates, strain induced precipitation will prelude

static recrystallisation. Delaying recrystallisation during inter-pass times leads to strain accumulation and increased driving force for recrystallisation. Solute drag occurs when solute atoms in the alloy matrix, limiting the grain boundary migration needed for recrystallisation [70, 71].

2.5.2.1 Effect of roughing on ferritic stainless steel texture

Roughing is the hot rolling of the as-cast slab under high deformation per pass. Cast stainless steel slabs are typically solution treated between 950 and 1050 ºC and this was followed by roughing, i.e. reduction of the 200 mm slab to a 30 - 40 mm transfer bar with exit temperatures as low as 850 ºC [29].

The sheet's surface, which is in contact with the roll experiences high friction and shear deformation while the centre experiences near plain strain deformation [17, 18]. Coupled with this, the higher cooling rate on the surface results in less dynamic recovery and increasing dislocation density, which encourages dynamic recrystallisation of the surface layers in the final passes.

High rolling temperatures and lowered strain rates favour recovery. The resultant microstructure is characterised by elongated grains. This results in non-randomisation of texture [17, 19, 21]. These un-recrystallised grains form strong Alpha fibres with weak Gamma fibre. The strong Alpha fibres associated with the {001}<110> components arise from {001}<uvw> columnar grains as no randomisation of texture occurs from either phase transformation or recrystallisation [52, 79].

2.5.2.2 Effect of finishing on ferritic stainless steel texture

After roughing, the transfer bar is rolled down to a final thickness of 3 to 5 mm through the finishing rolling process [29]. DRX is the most common softening mechanism from finishing processes due to the high amount of stored deformation with lowered temperatures which limits DRV, increases the strain accumulation and overall the driving force for DRX [6, 80].

Braga et al. [61] employed a five-pass thermomechanical processing simulation to study the effect of inter-pass time, entry and exit temperature during finishing rolling on the softening mechanisms in 430 FSS. The study revealed that increased inter-

pass time, high entry temperature and lower exit temperature leads to increase recrystallisation. It was found that DRV and SRX were prevalent in the first three passes during finishing rolling. However, recovery was not effective in the last two passes. Microstructural evaluations found that recrystallisation occurred entirely in passes one to three, with partial recrystallisation and work hardening occurring in the last two passes. The last two passes favoured work hardening due to lowered process temperature. Braga [6] also studied finishing rolling of FSS through interrupted Steckel mill simulations. It was found that inter-pass recrystallisation was favoured by decreasing initial hot rolling temperatures between 900 and 840 °C and that work hardening in the last few passes of Steckel mill simulations would favour recrystallisation in hot band annealing before cold rolling.

Gao et al. [72] found that a decrease in hot deformation temperature resulted in a shift from {001}<110> towards {111}<110> stable end orientations. Lowering the final pass deformation temperature also encouraged the formation of in-grain shear bands that appeared in <111>//ND grains. Gamma fibres nucleate in micro shear bands [52].

Another study on 21%Cr FSS showed a 25% increase in R-value and a 40% decrease in surface roughness after straining at 15% when the finishing entry temperature was decreased from the conventional entry temperature of 970 up to 750 °C. The reason for decrease in surface roughness was due to an increase in recrystallisation of {111} textures [27]. It should be noted that lowered finishing temperatures are not always practicable in the industrial processing of FSSs due to increased mill loads [73].

Gao [4] found that the layer close to the surface is characterised by strong {011}<uvw> and weak {225}<554> shear-induced textures after hot rolling. The centre was dominated by strong Alpha fibre and weak Gamma fibres in the hot rolled plate and this was retained after annealing as well. The Alpha fibre of {115}<110> formed from the persistent as-cast columnar grains with {001}<uvw> structure. Furthermore, these textures exhibit a low Taylor Factor, making them more susceptible to recovery than recrystallisation during annealing [4].

2.5.2.3 Effect of cold rolling & annealing on ferritic stainless steels' texture

Cold rolling of FSS is a strain-hardening process, whereby material experiences an increase in strength with a decrease in ductility, typically conducted between 60 and 180 ºC. Cold rolling allows for a better overall surface finish and dimensional control than hot rolling. It can be used to optimise the texture through annealing processes [74].

Due to the elongation of the already elongated hot band grains, cold-rolling results in a pancaked structure, with final annealing, these elongated grains, recrystallise into grain colonies of similar orientations [4]. During cold rolling, the intensity of the Alpha fibres increases towards the centre of the sheet, strengthening the {001}<110>, {112}<110>, {111}<110> or combinations thereof including the Gamma fibre, if present. Simulations of sheet surface texture show that slight deviations from Goss during cold rolling tend to re-orient toward {111}<112> Gamma fibre or towards {001}<110> Alpha fibre. The intensity of Alpha fibres increases throughout the thickness with an increase in reduction during cold rolling. Gamma fibres increase in all layers with an increase in reduction, but intensity decreases towards the centre and is attributed to texture distribution in the hot band. The sheet has strong Alpha and weaker Gamma fibre following cold rolling, and texture gradients within the hot band tend to disappear. During annealing the cold-rolled sheet, the Alpha fibre tends to be replaced by Gamma fibre as you get closer to the sheet centre. An advantage of the {111}<112> component is that its nucleation and growth lead to the final product's texture. These grains possess positive and negative out-of-plane shear strain and favour reduced ridging [4, 17].

Annealing of hot-rolled material alters the microstructure but not as significantly as annealing following cold rolling [22]. A study found that samples with a hybrid columnar and equiaxed structures were less prone to ridging following annealing of the hot band prior to cold rolling [23].

Chapter 3: Material & Methodology

3 MATERIAL & METHODOLOGY

The material used in the current study was AISI 436 FSS samples produced by Columbus Stainless Steel Pty Ltd in Middelburg, South Africa. The chemical composition of the steel as is given in Table 3-1 and compared to ASTM A240 for the 436 steel grade. The received as-cast sample was macroetched and characterised to determine the cast structure. The columnar region was isolated and subjected to uniaxial hot compression tests.

Uniaxial multi-pass compression tests were aimed at simulating the industrial roughing and finishing rolling conditions. The resulting microstructures and textures were studied to determine whether they were favourable for ridging resistance or not. The microstructures and textures were analysed after the third and sixth passes, with a systematic changing of the inter-pass time, strain rate and strain. An additional set of deformation schedules of 4 passes were undertaken to study the relative effects of inter-pass time and strain rate on the deformation behaviour.

Table 3-1: Chemical composition for FSS grade 436 as per ASTM A240 with the material composition for the received sample.

Steels		Wt %								
		C	Si	Mn	P	S	Cr	Mo	Ni	Nb
Study sample		0.014	0.420	0.39	0.022	0.001	17.2	1.217	0.27	0.415
ASTM 240	Min	-					16	1.25		5xC
	Max	0.12	1	1	0.04	0.03	18	1.25	-	0.8

3.1 Deformation schedules

The hot deformation tests were conducted in close compliance with the uniaxial compression test good practice guide [75]. Cylindrical samples were machined from the columnar region of the cast slab, as the material in this region is difficult to recrystallise during hot rolling. Samples were prepared by wire-cutting cylinders of 15 mm length and 10 mm diameter for the Gleeble test and 10 mm length and 5 mm diameter for the Dilatometer test. This was done along the normal direction of the cast sample as shown in Figure 3-1. The hot deformations were carried out on a Gleeble 1500D system and the Bahr Dilatometer. The Gleeble was used to simulate lower strain rates, whilst the dilatometer was used for higher strain rate tests.

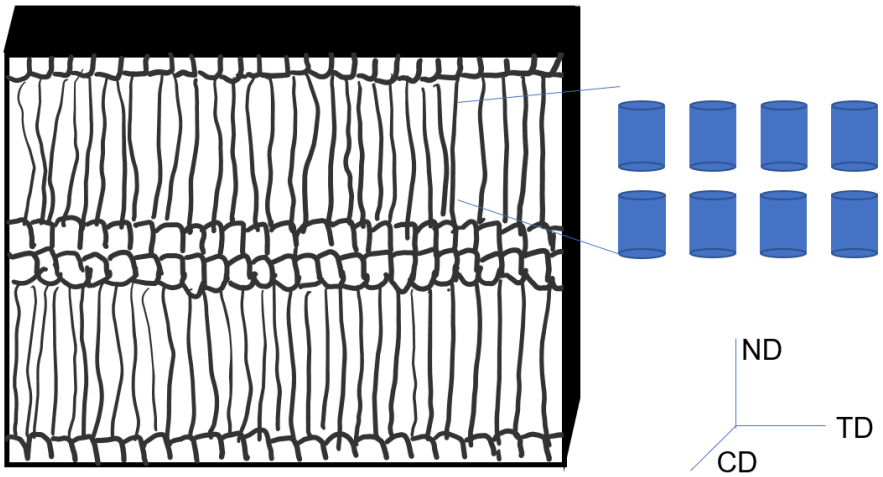

Figure 3-1: Depiction of area where samples were machined from the columnar region of the as received cast slab (not to scale).

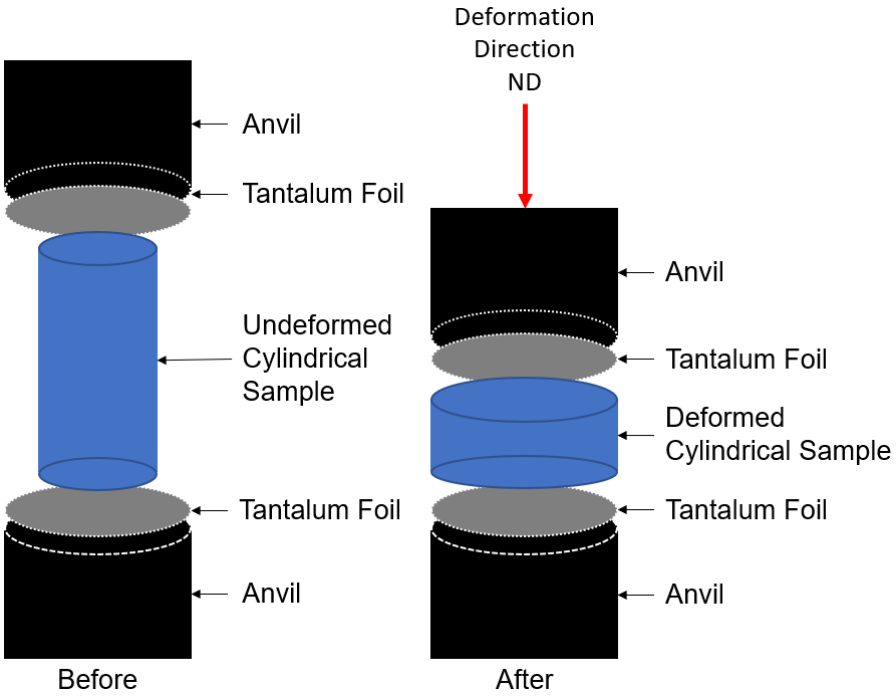

Figure 3-2: Sample test set-up orientation in Gleeble and Dilatometer compression test before and after deformation.

3.1.1 Gleeble thermomechanical simulation

The Gleeble 1500D thermomechanical simulator was used to undertake uniaxial compression test. Heating rates were fixed at 20 °C/s. Samples were first soaked at 1080 °C for 300 s, cooled to the temperatures of interest and thereafter subjected to various processing conditions as set out in Table 3-2. The specimens were held for 5

s at deformation temperature to allow for temperature equalisation before the isothermal deformation.

The roughing rolling was simulated in the first three passes and finishing in the last three passes. The finishing rolling conditions were kept the same for all three simulations. The specimens were quenched after third (designated by CR, R1 and R2 in text) and sixth passes (designated by CF, F1, F2 in text) to study the effective change of the roughing rolling simulations on finishing rolling. A total of 6 compression tests were thus undertaken. The control tests, denoted by CR and CF, simulated close to current industrial roughing conditions. The R1 and F1's inter-pass time was increased during roughing passes while R2 and F2 both inter-pass and the strain per pass were increased during roughing passes, as shown in Table 3-2.

Table 3-2: Test matrix for roughing and finishing six pass simulations

Experimental	Parameter	Roughing			Finishing		
		P1	P2	P3	P4	P5	P6
	Temperature (°C)	1000	950	930	920	910	900
	Strain rate (/s)	5					
CR/ CF	Inter-pass (s)	11	14	18.3	36	38	52
	Strain	0.18	0.2	0.3	0.2	0.2	0.2
R1/ F1	Inter-pass (s)	15	20	25	36	38	52
	Strain	0.18	0.2	0.3	0.2	0.2	0.2
R2/ F2	Inter-pass (s)	15	20	25	36	38	52
	Strain	0.2	0.3	0.3	0.2	0.2	0.2

To ascertain how much retained strain was in each of the 3 and 6- pass deformation structures, hardness tests were undertaken. After hot deformation, the samples were annealed at 800 °C for 300 s to evaluate the extent of softening. Hardness values were taken with a dwell time of 10 seconds on a Struers Duramin-40 micro-vickers hardness tester.

3.2 Dilatometer

Two sets of tests were undertaken on the Dilatometer; the first set simulated the 3-pass Gleeble roughing rolling simulation but at 15 /s strain rates, see Table 3-3. However, the thermal path was not changed in that the heat profile was consistent

with the previous test. These tests were suffixed by -15/s, denoting the strain rate to differentiate them from Gleeble 5 /s strain rate tests.

Table 3-3: Test Matrix for simulated three pass roughing rolling on Dilatometer

Experimental	Parameter	Roughing		
		P1	P2	P3
	Temperature (°C)	1000	950	930
	Strain rate (/s)	15		
CR -15/s	Inter-pass (s)	11	14	18.3
	Strain	0.18	0.24	0.3
R1 -15/s	Inter-pass (s)	15	20	25
	Strain	0.18	0.24	0.3
R2 -15/s	Inter-pass (s)	15	20	25
	Strain	0.24	0.3	0.3

The second set of tests were undertaken to study the effect of strain rate and inter-pass time on the evolution of texture by maintaining a constant strain. A total of 4 compression test schedules were undertaken in 4-passes, to evaluate roughing conditions over multiple passes. The “short” (20 s) and “long” (40 s) inter pass time deformation profiles were analysed for the progression of the restoration. In addition, the effect of strain rate was also investigated.

Table 3-4: Test matrix for the study of the effect of inter-pass time and strain rate on the restoration process.

Parameter			Roughing			
			P1	P2	P3	P4
Temperature (°C)			1000	960	930	900
Strain			0.24	0.3	0.23	0.23
Stain rate	5/s	Short inter-pass time	20 s			
		Long inter-pass time	40 s			
	15/s	Short inter-pass time	20 s			
		Long inter-pass time	40 s			

Following the various deformation schedules, true flow stress-strain curves were produced and evaluated to study recrystallisation and recovery. Friction was accounted for by a coefficient of 0.2. Tantalum foil was used to reduce incidence of sticking and to minimise friction. After each test, the samples were quenched in a

helium. The specimens were thereafter analysed for microstructure, grain boundary and texture evolution.

The choice for the area of analysis is supported by many researchers [76, 77, 78] and an analysis of the strain distribution within the deformed sample is provided in Figure 3-3. The authors all found that the applied strain is concentrated typically in the centre of the uniaxial test piece and decreases as one moves away from the centre, creating dead zones.

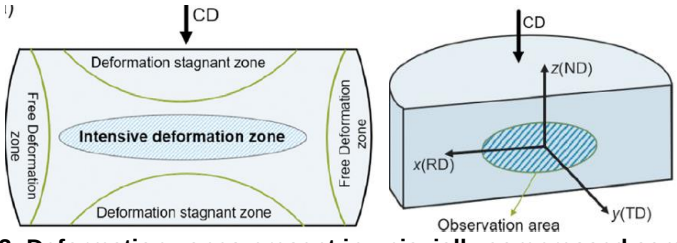

Figure 3-3: Deformation zones present in uniaxially compressed samples [51].

The deformed samples were carefully sectioned to ensure dead zones were not used in the analysis but softened areas of interest through transverse view was selected shown as 'intensive deformation zones' in Figure 3-4. The deformed discs were sectioned at the sample centre, and the rolling direction was taken in the direction the sample elongated. The deformed samples were sectioned parallel to the rolling direction (RD).

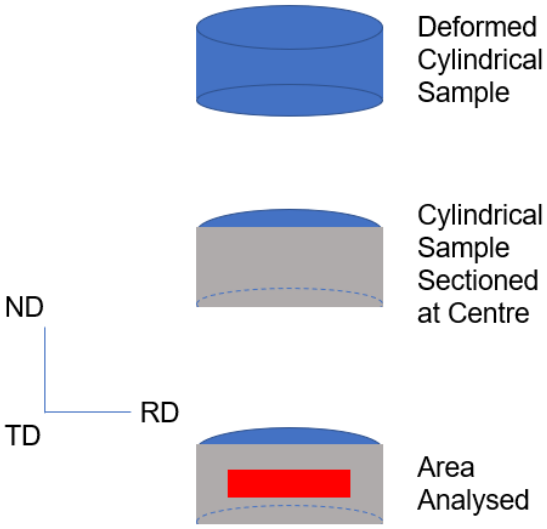

Figure 3-4: Deformed areas of interest used for the analysis.

3.3 Microstructural analysis

Light optical microscopy and electron microscopy techniques were used to analyse the microstructure of the samples. Whilst the optical microscopy focused on the structure and phases present in the samples, electron microscopy was used for the grain orientation and microtexture in the materials.

3.3.1 Optical microscopy

The microstructural evolution was studied using an Olympus BX51M microscope. The microstructures were revealed by etching with using an Aqua-Regia solution for 10 s after grinding and polishing to a 1 µm finish.

The macrostructures were taken by grinding and polishing a section of the cast slab followed by etching in aqua regia solution to evaluate the differences in structure moving from the chill zone through the columnar zone towards the centre equiaxed zone. This was done by Columbus Stainless Steel. ImageJ software was used to analyse both the macro- and microstructures i.e., grain angle alignment to the deformation axis, grain size and particle size. Where possible, grain size measurements were taken on macrographs using the linear intercept method and the grain size was determined using equation 3.1 [79, 31]:

Equation 3.1:

$$\bar{l} = \frac{L_T}{PM}$$

Where M is the magnification, P is the number of grains intersected by the line, L_T is the total length of the line and $\bar{l}$ is the average grain size.

The continuously cast structure was analysed to understand and evaluate the effects of this cast structure on subsequent processing steps and the overall transformation of this structure during processing. Microstructures were taken of the chill zone, columnar and equiaxed grains at 50X, 200X and 500X magnifications, respectively. In addition, micrographs of the deformed samples were taken at various magnifications. When relevant the 50X magnification micrographs were stitched to give a perspective of the relative grain sizes and recrystallisation behaviour.

3.3.2 Scanning electron microscopy- Energy dispersive spectrocopy analysis

The SEM imaging was taken in conjunction with EBSD and EDS analyses. Precipitates were identified and examined using the Jeol IT300LV SEM and XMAX^n EDS detector with a 1 µm probe size at an accelerating voltage of 15 to 20 kV to study its evolution from casting through deformation processing. Although 20 kV is high for analysis, it was done to identify Mo and Nb precipitates as shown in Table 3-5.

Table 3-5: Characteristic EDS peak voltages (kV) for identifying elements relevant to this study [80]

	Fe	Cr	Mo	Nb	Ti	Ca	C	O	Al	Si
Kα	6.398	5.411	17.441	16.581	4.508	3.690	0.277	0.525	1.586	1.739
Lα	0.705	0.573	2.293	2.166	0.452	0.341	-	-	-	-

When analysis of a sample is done with SEM, electrons penetrate the sample surface and scatter inelastically within the material. These can be simulated by complex Monte Carlo simulations to find the electron trajectory within the surface of the sample as shown in Figure 3-5.

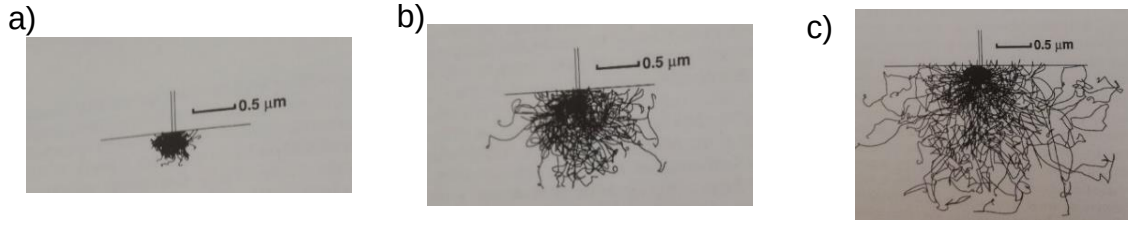

Figure 3-5: Monte Carlo simulation of electron trajectory simulations showing the interaction volume in iron at beam energies of a) 10 keV, b) 20 keV and c) 30 keV [80].

If the electrons interact with an area larger than the precipitate size, they essentially would result in background data from the base material. Kanaya-Okayama [81] simplified the interaction to the radius of interaction volume. The interaction depth (µm) can be approximated as:

Equation 3.2:

$$R_{KO} = \frac{0.0276AE_0^{1.67}}{Z^{0.89}\rho}$$

Where, E_o is the incident beam energy (keV), A is the atomic weight (g/mole), ρ is the density (g/cm^3) and Z is the atomic number. The interaction volume radius can be approximated as shown in Table 3-6.

Table 3-6: Interaction volume radius of interest, with approximated values for compounds of interest to this study considering the atomic ratios [31, 81].

Element/ compound	A (g/mole)	Z	ρ (g/cm^3)	R_{KO} (µm)	
				E_o (keV)	
				15	20
Fe	55.85	26	7.87	0.99	1.60
Nb	92.91	41	8.57	1.01	1.63
Cr	52.00	24	7.19	1.09	1.76
C	12.011	6	2.25	2.75	4.45
Approximated interaction volume					
Fe_2Nb	N/A	N/A	N/A	0.997	1.61
17Cr-Fe				1.01	1.63
NbC				1.88	3.04

Applied EDS voltages of 15 kV was used at high magnification to limit interaction volume and improve the reliability of results. For EDS maps undertaken during EBSD evaluation, the accelerating voltage was set at 20 kV.

3.3.3 Electron backscatter diffraction texture analysis

The SEM-EBSD equipped with an Oxford Nordlys Nano EBSD detector was used to analyse texture. The samples were analysed at large step sizes for cast structures to achieve coefficient linear expansion ODF maps and better understand the as-cast texture. The samples were analysed at large step sizes of 2 µm for low magnification scanning and small step sizes of 0.3 - 0.5 µm for high magnification scanning. This was undertaken to not miss any details of the deformed matrix. The EBSD analysis was done at an accelerating voltage of 20 kV and working distance of 20 mm. The sample was tilted at an angle of 70º to maximise the diffracted signal while minimising the signal to noise ratio. After grinding and polishing to 1 µm finish, electropolishing was done using the Struers Electropol automated polisher with A3® solution to remove any deformed matrix resulting from prior mechanical polishing. Post-processing to attain ODF, Taylor Factor (TF), IPF maps and MAD plots were done using AzTec Software and HKL Channel 5 software package. For all mapping, zero solutions were under 10%, aside for images in Figure 4-20, where zero solutions were under 30%. The lowered hit rate was likely due to the lower magnification used affecting results.

3.3.4 Transmission electron microscopy analysis

Samples were mechanically ground from 3 to 0.5 mm and subsequently polished to a 50 µm thickness with a 1 µm surface finish. After mechanical polishing, the samples

were jet polished further using a Struers Tenupol-3 twin-jet polisher using an A3® solution to create a thin film through which electrons can pass through. A Jeol 2100F FEGTEM was used to analyse the sample.

3.4 ThermoCalc™ phase transformation predictions

The simulation software ThermoCalc™ was used to predict the equilibrium phase transformation. The phase transformations predictions provided valuable insights into the correlation between microstructure and material properties. ThermoCalc™ 2019b with the TCFE7 database was used to understand the phase changes and precipitates likely to form during the heating and cooling cycles. The ThermoCalc™ TC Prisma plots were also used to gather information on the nucleation rate and particle density of the Laves and NbC phases.

The system showed that 436 FSS exhibits a main single-phase structure at all temperature ranges with secondary phases of significance precipitating from 1300 °C upon cooling, see Figure 3-6. ThermoCalc™ simulations based on the composition of 436 FSS presented in Table 3-1 confirmed the matrix of the steel to be ferritic under the conditions at which tests in the current study were carried out.

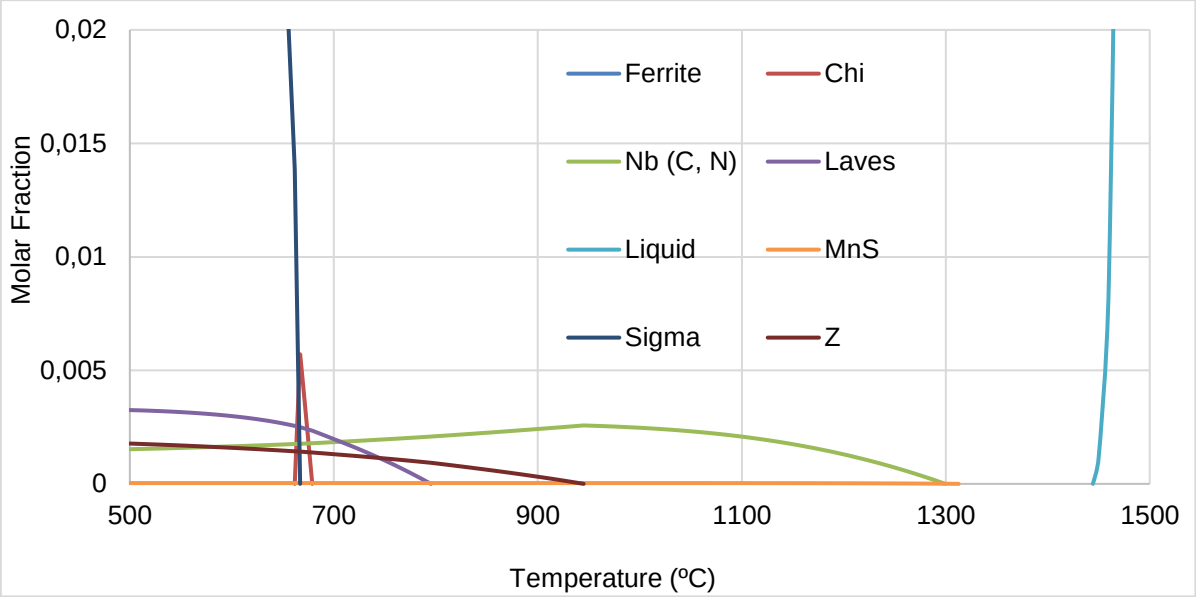

Figure 3-6: Molar fraction of the phases present in the steel received as a function of temperature predicted through ThermoCalc™.

In terms of the study of precipitates at play, the precipitation module was used to study precipitation kinetics using the Langer-Schwartz theory and the Kampmann-Wagner numerical approach [82, 83].

Figure 3-7 shows Thermocalc™ simulations carried out to determine the rate at which NbC precipitates at different deformation temperatures of interest.

The graphs show that the nucleation rate is initially high; thus, the number of particles forming increases, increasing the volume fraction of particles in the ferritic matrix. It was also noticed that all of these reactions occur within short periods. It is helpful to note that the volume fraction increases with decreasing density of precipitates. The precipitate number density then decreases, even though the volume fraction remains the same. The most practical explanation for this would be particle coarsening.

As the particles grow, small particles dissolve into the matrix as they do not reach a critical size. The dissolved particle can diffuse to larger stable embryos to assist in grain growth. Thus, the number of particles formed would be decreased but the volume fraction remains the same, whilst the nucleation rate decreases are attributed to the matrix not being able to precipitate NbC anymore as the matrix of ferrite is depleted in either C or Nb, likely Nb. The precipitate size is known to have a significant effect on recrystallisation through the mechanism of particle stimulated nucleation (PSN). Critical to note is that this could be detrimental to recrystallisation, if a critical particle size is not achieved, whereupon gran boundary pinning would occur [18].

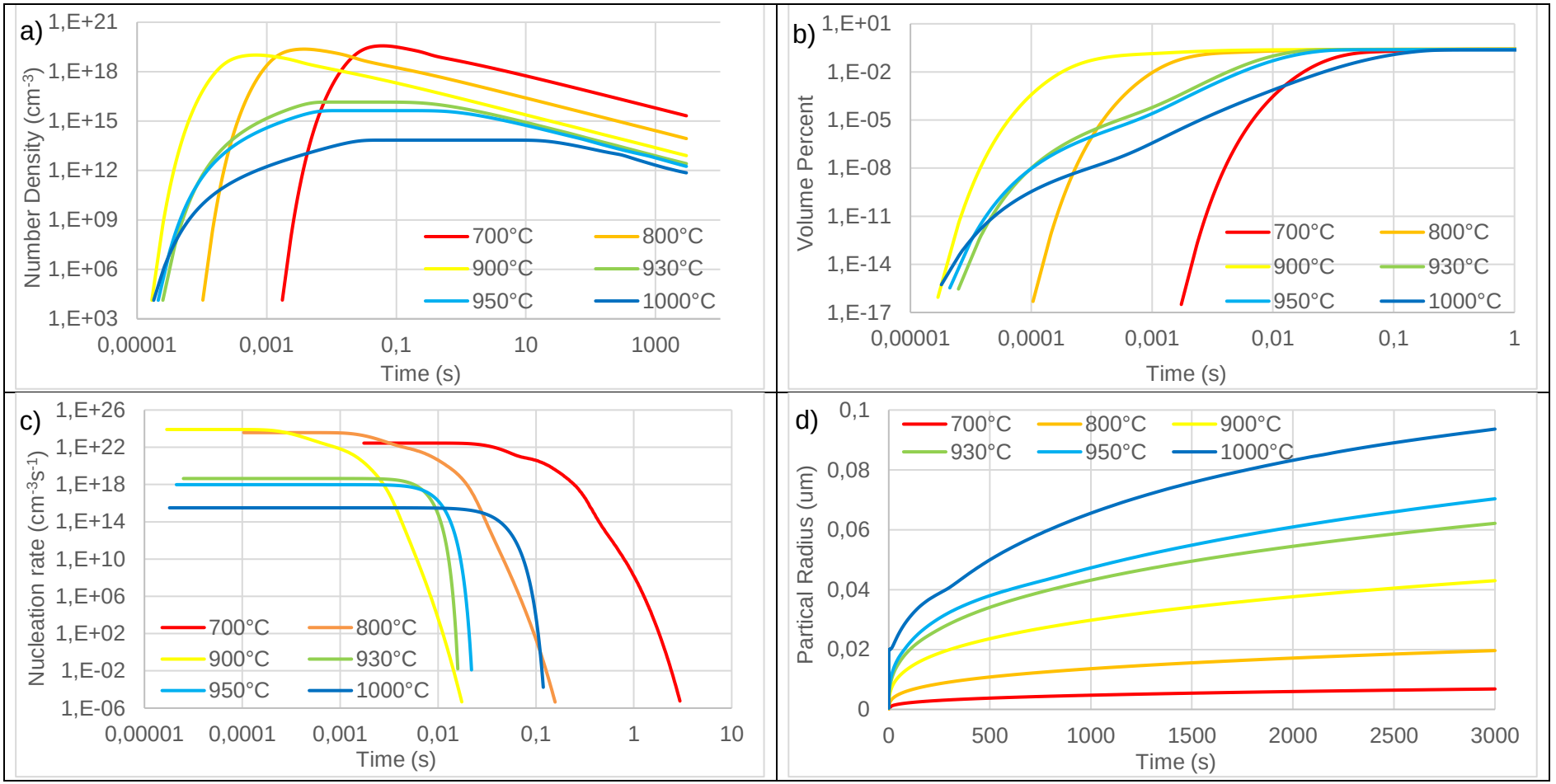

Figure 3-7: Thermocalc™ NbC precipitate analysis showing, a) number density of NbC precipitates forming at various temperatures, b) volume percentage of NbC precipitates forming at various temperatures, c) nucleation rate of NbC precipitates forming at various temperatures and, d) mean radius of NbC precipitates at various temperatures if growth is assumed to be spherical

Chapter 4: Results

4 RESULTS

4.1 As cast macrostructures

Macrostructural observation of the as-cast structure is essential in understanding material behaviour during thermomechanical processing. Figure 4-1 shows the macrographs of the cast sample with conspicuous regions of the chill zone on the outer edges, columnar grains at quarter thicknesses and equiaxed grains at the slab centre. The volume fraction of the chill zone, columnar zone and equiaxed zone were found to be 10, 80 and 10% respectively. The most dominant region was the columnar zone. The macroetched structure correlates to structures published by Kodukula et al. [84] with the equiaxed grain ratio (the thickness of equiaxed zones over the slab thickness) being 10% in this study.

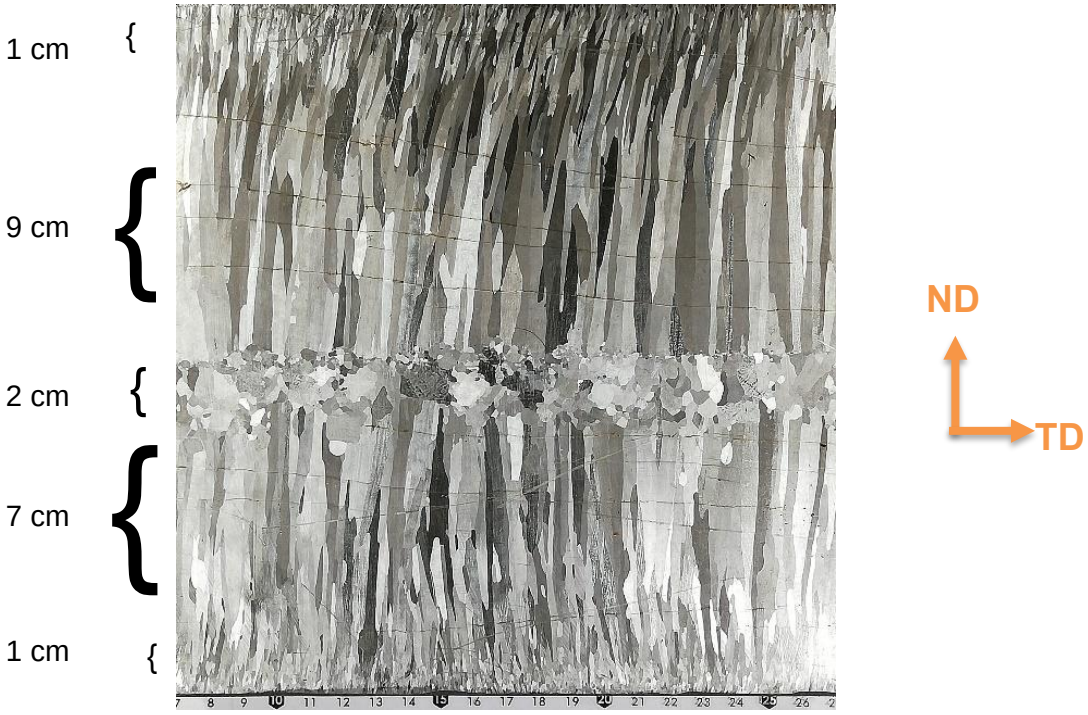

Figure 4-1: As received macro-etched of the through thickness section of the continuously cast slab. The scale at the bottom of the pic is in centimetres.

Grain sizes were determined using the grain intercept methods. Chill zone grains were not analysed for grain size as they were too large to be measured representatively by optical microscopes and too small to be characterised through macrostructure imaging. As columnar grains were significantly elongated, the length and width of

grains were determined at 90° angles to each other. It is known that the as-cast columnar structure is detrimental to the ridging properties of FSS, with columnar grains typically having Cube texture [23, 84]. The grain dimensions were measured to be 27.4 ± 12.7 mm in length and 3.44 ±0.4 mm in width. The length-to-width ratio gave the anisotropic index of 7.97 for the as-cast columnar structure. The average grain size was measured to be 3.47 ± 0.62 mm for equiaxed grains. Modak [23] elaborates that the presence of smaller grains would allow for more significant constraint by neighbouring grains and allow for the activation of different slip systems in adjacent grains allowing for lattice rotation upon deformation.

4.2 Flow stress curves

4.2.1 Flow stress curves for roughing rolling simulations

Figure 4-2 presents the Von Mises stress as a function of equivalent strain for the roughing simulations according to the schedules set out in Table 3-2. From Figure 4-2, all deformation schedules showed increased flow stress with applied strain for the first three passes. The CR and R1 deformation schedules show that both the second and third passes continued along the prior deformation path, evident by their similar work hardening rate Figure 4-3. This was most likely due to recovery between passes. R1 had a longer inter-pass time compared to the CR sample, hence the lack of softening between passes implied that no significant recovery occurred during the inter-pass times. As may be seen, R2 was subjected to higher strains per pass.

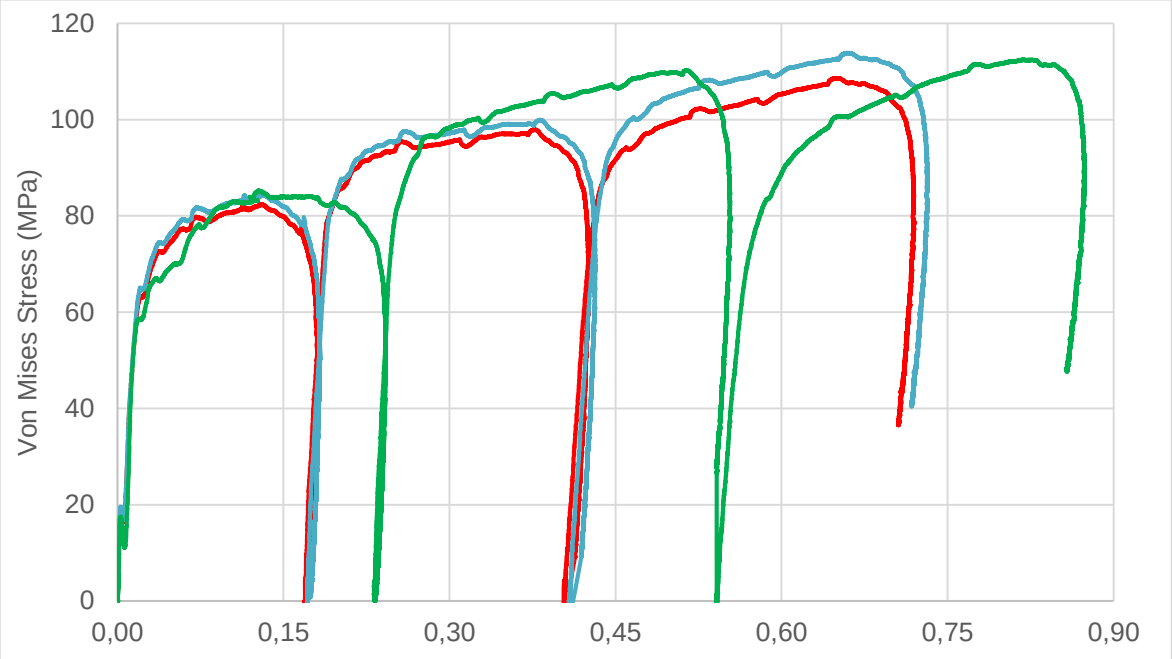

		Pass 1	Pass 2	Pass 3
Temperature		1000˚C	950	930˚C
Strain rates		5/s		
Strain	CR R2	0.18 0.24	0.24 0.3	0.3 0.3
Inter-pass time	CR R1 & R2	11 s 15 s	14 s 20 s	18.3 s 25 s

Figure 4-2: Flow stress curves for 3-pass roughing rolling simulation carried out under different roughing conditions at 5/s, more details provided in Table 3-2. CR defines close to industrial conditions, R1, increased inter-pass times and R2, increased inter-pass times and strain

R2-Pass 3 showed higher work hardening rate relative to samples CR and R1 Figure 4-3a. This was most likely due to the increased strain in pass 1 leading to more retained strain in pass 2, which triggered static restoration during the inter-pass time between passes 2 and 3. Upon straining in pass 3, the work hardening rate of R2 was comparatively higher than CR and R1 samples. This is evident in Figure 4-3c where local misorientation maps show widespread deformation after pass 3 for CR and R1 simulations compared to R2. R2 had undergone more restoration between passes 2 and 3 due to increased strain and inter-pass times, exhibiting a less strained structure, Figure 4-3c. R2 underwent more recovery and, therefore had less stored energy due to restoration between passes 2 and 3.

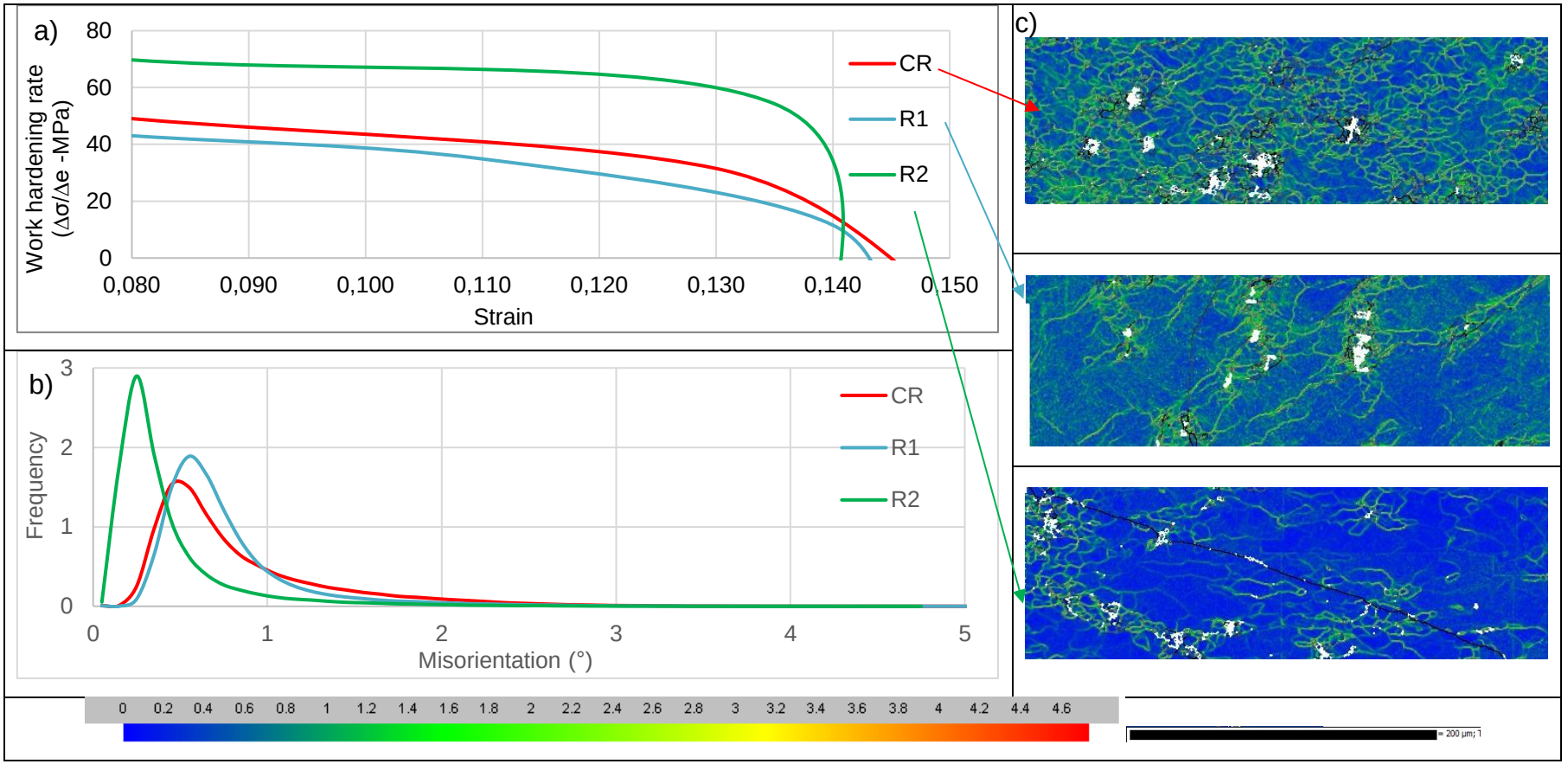

Figure 4-3: a) Work hardening rate of pass 3 as a function of applied strain at a strain rate of 5/s. b) Local misorientation plots for CR, R1 and R2 roughing rolling simulations after pass 3, with associated c) local misorientation maps at 0.5 µm step size.

4.2.2 Effect of the inter-pass time, strain, and strain rate during roughing rolling simulations on the restoration mechanisms

Figure 4-4 to Figure 4-7 show the true stress-strain graphs and the corresponding mean flow stress curves after systematically varying the strain per pass, strain and inter-pass time in 3-pass and 4-pass simulated roughing rolling respectively. Figure 4-4 shows the effect of the inter-pass time and strain at 15 /s strain rate (Table 3-3), on the flow stress behaviour. As may be seen, all tests almost reached steady state stress in the second pass. Huang and Loge [16] stated that dynamic softening limits strain hardening by dynamic recovery similar to observations made by Braga et. al. [61]. For the R2 -15/s sample, unlike in the other two deformation schedules, the increased strain led to increased retained strain and, consequently, more dynamic restoration in pass 2, resulting in a lower yield strength in pass 3. Additionally, strain hardening occurred in pass 3 due to the lowered deformation temperature, which promoted the retention of strain due to lower driving force for dynamic restoration, similar to work done by Mehtonen [52], Figure 4-4. This was contrary to the CR-15/s and R1-15/s samples which reached steady state in pass 3. Figure 4-5 shows the MFS curves showing the increase work hardening in pass 3 of the R2-15/s and not in the CR-15/s and R1-15/s. The progressive increase in MFS in R2-15/s was attributed to DRV and not CDRX during the simulated roughing rolling.

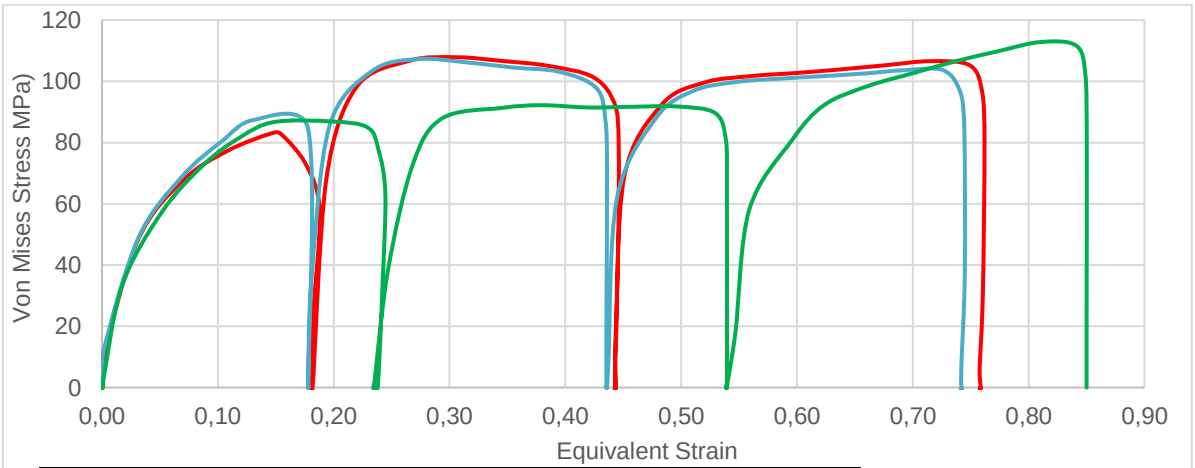

		Pass 1	Pass 2	Pass 3
Temperature		1000˚C	950˚C	930˚C
Strain rates		15/s		
Strain	CR 15/s R2 15/s	0.18 0.24	0.24 0.3	0.3 0.3
Inter-pass time	CR 15/s R1 15/s & R2 15/s	11 s 15 s	14 s 20 s	18.3 s 25 s

Figure 4-4: True stress-strain flow curves at 15/s, 3-pass roughing rolling simulations (Table 3-3), to study the effect of inter-pass time and strain applied per pass.

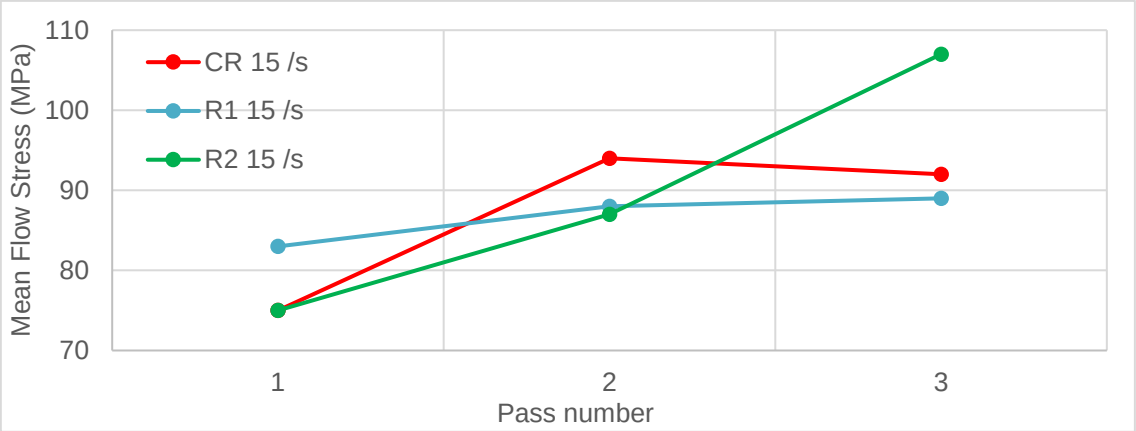

Figure 4-5: Mean flow stress per pass for the 3-pass roughing rolling simulated at a 15/s strain rate.

Figure 4-6 and Figure 4-7 show the 4-pass roughing rolling simulation true stress-strain flow curves and corresponding MFS curves at 5 and 15 /s strain rates with 20 and 40 s inter-pass times respectively (Table 3-4). While there was a significant increase in the flow stress and strain rate, no clear trend was observed by doubling the inter-pass time from 20 to 40 s. This suggested that there was no significant static restoration during the inter-pass time beyond 20 s. Mean flow stress data is presented in Figure 4-7, with corresponding increase in mean flow stress when inter-pass time and strain rate increases.

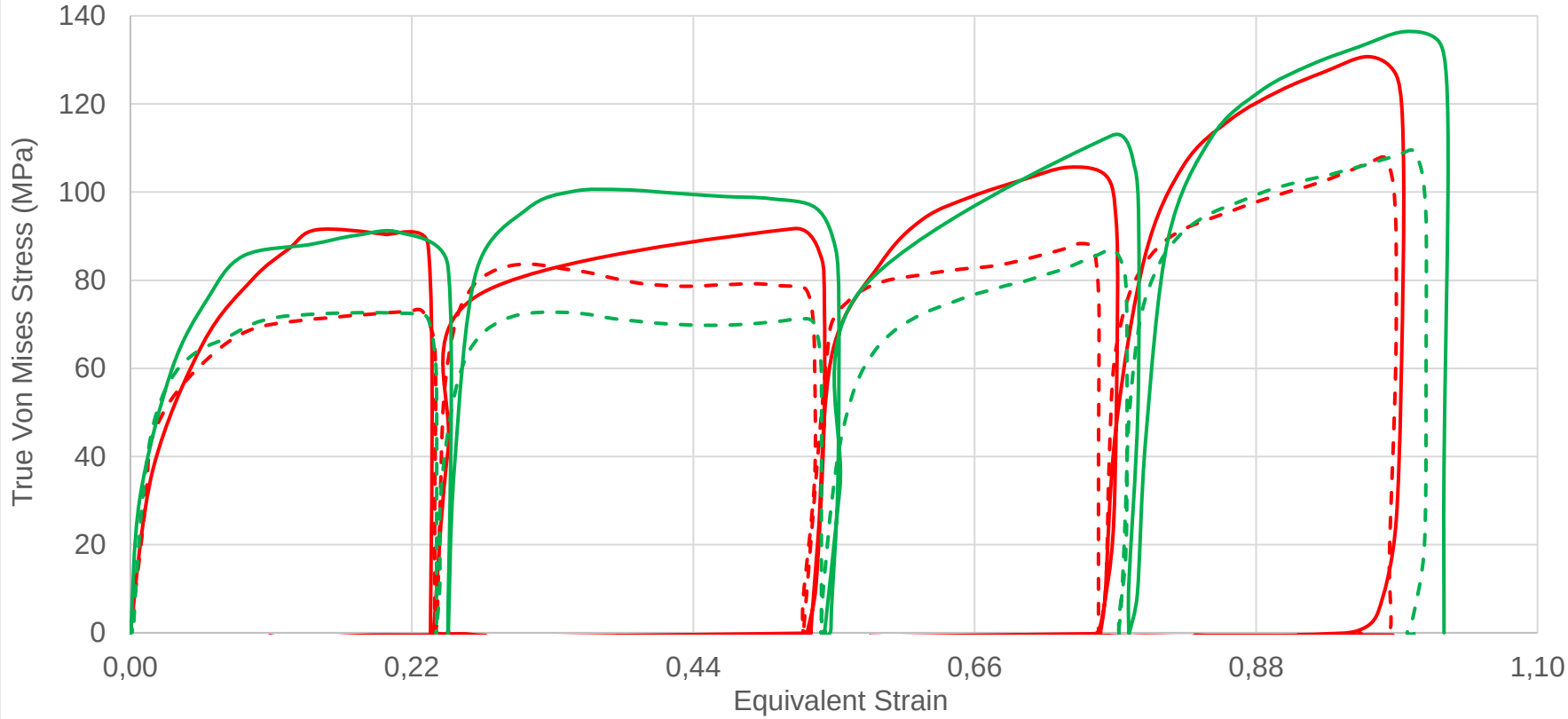

	Pass 1	Pass 2	Pass 3	Pass 4
Temperature	1000˚C	960˚C	930˚C	900˚C
Strain	0.24	0.3	0.23	0.23
Inter-pass times	20 s or 40 s			
Strain rates	5/s or 15/s			

Figure 4-6: Flow stress curves depicting the effect of strain rate and inter-pass time on roughing rolling simulation of 4-passes.

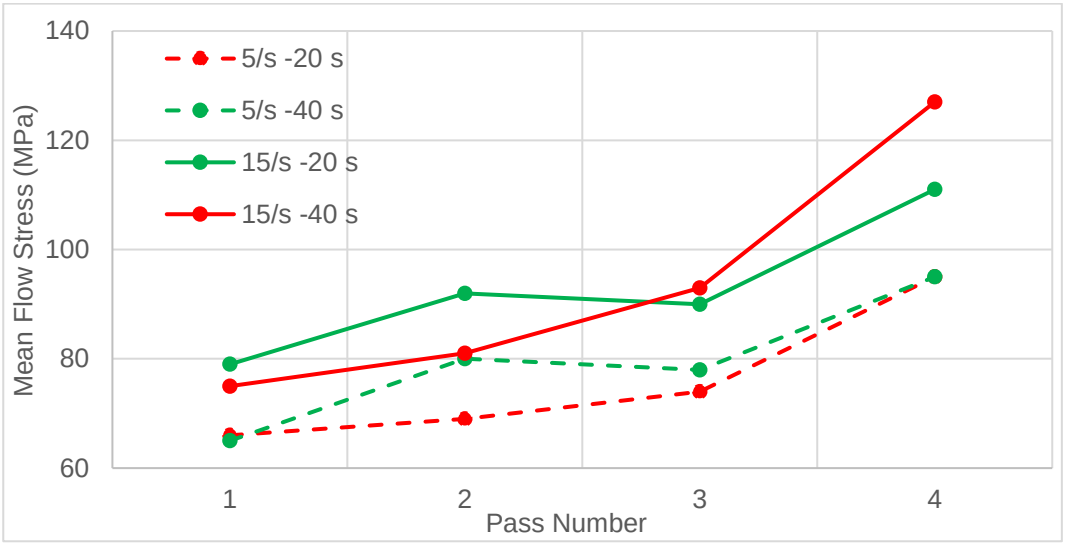

Figure 4-7: Mean flow stress curves showing the relationship between inter-pass times and strain rate.

4.2.3 Flow stress curves for roughing and finishing rolling simulations

Figure 4-8 presents the six-pass deformation schedules used for simulating roughing and finishing rolling schedules. After pass 3, the softening between passes was more significant with each successive pass, in that the maximum stress reached during deformation decreased, which signified substantial fraction of either dynamic or static or both softening mechanisms at play. Due to smaller strains per pass i.e. an average of 0.2 strain, the flow stresses never reached steady state, and as such, it cannot be deduced whether dynamic softening had been completed or not. Figure 4-9a shows the work hardening rate in the final pass as a function of the strain as well as the corresponding misorientation plots for the data. The graph shows that the work hardening behaviour for the F1 and F2 samples are significantly higher and similar when compared to the CF sample in pass 6. Furthermore, the higher work hardening rate in F1 and F2 could be attributed to the retained strain. This will be elaborated on later in section 4.4.3.

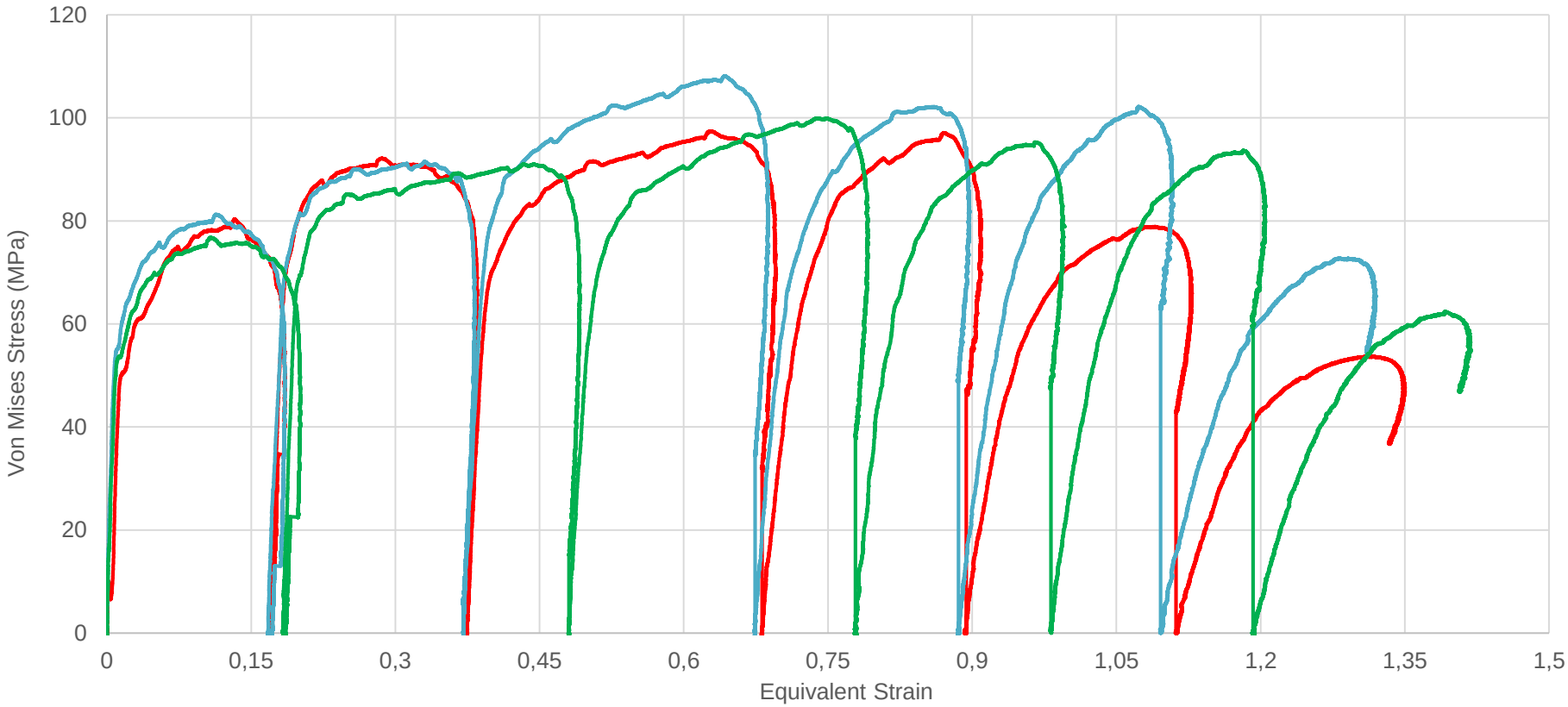

		Pass 1	Pass 2	Pass 3	Pass 4	Pass 5	Pass 6
Temperature		1000˚C	950	930˚C	920˚C	920˚C	900˚C
Strain rates		5/s					
Strain	CF F2	0.18 0.24	0.24 0.3	0.3 0.3	0.2	0.2	0.2
Inter-pass time	CF F1 & F2	11 s 15 s	14 s 20 s	18.3 s 25 s	36 s	38 s	52 s

Figure 4-8: True stress-strain graphs for 6 pass schedules from roughing and finishing rolling simulations, where CF was taken as control, F1 had an increase in inter-pass time in the first 3 passes and F2 had an increase in inter-pass time and strain in the first 3 passes.

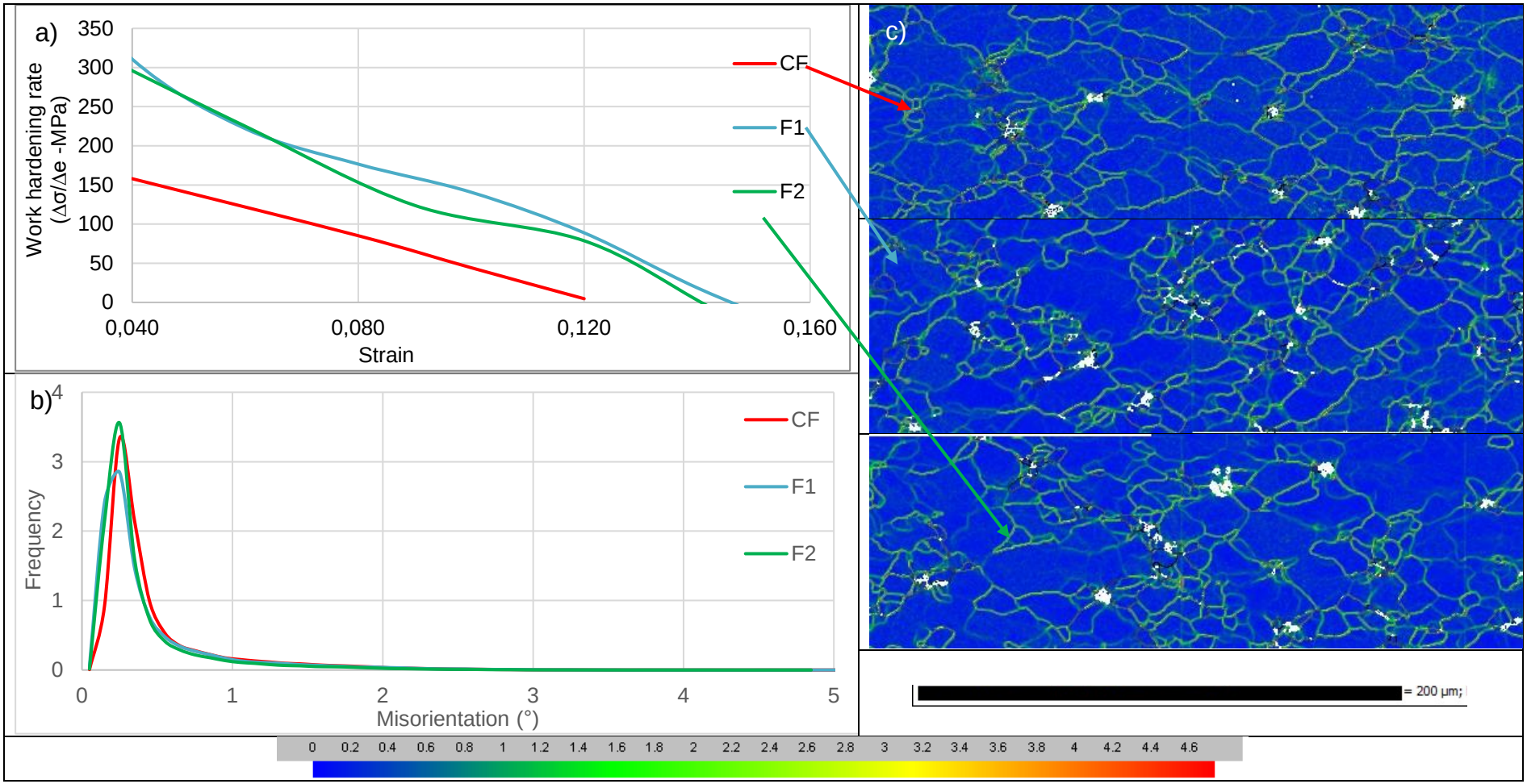

Figure 4-9: a) Work hardening rate as a function of applied strain of pass 6 for 6-pass finishing rolling simulations at a strain rate of 5/s. b) Local misorientation plots for CF, F1 and F2 roughing rolling simulations, with associated c) local misorientation maps. Maps taken at a 0.5 µm step size.

To ascertain how much retained strain was in each of the 3 and 6 - pass deformation structures, hardness tests were undertaken, Figure 4-10. After hot deformation, the samples were annealed at 800 °C for 300 s to evaluate the extent of softening.

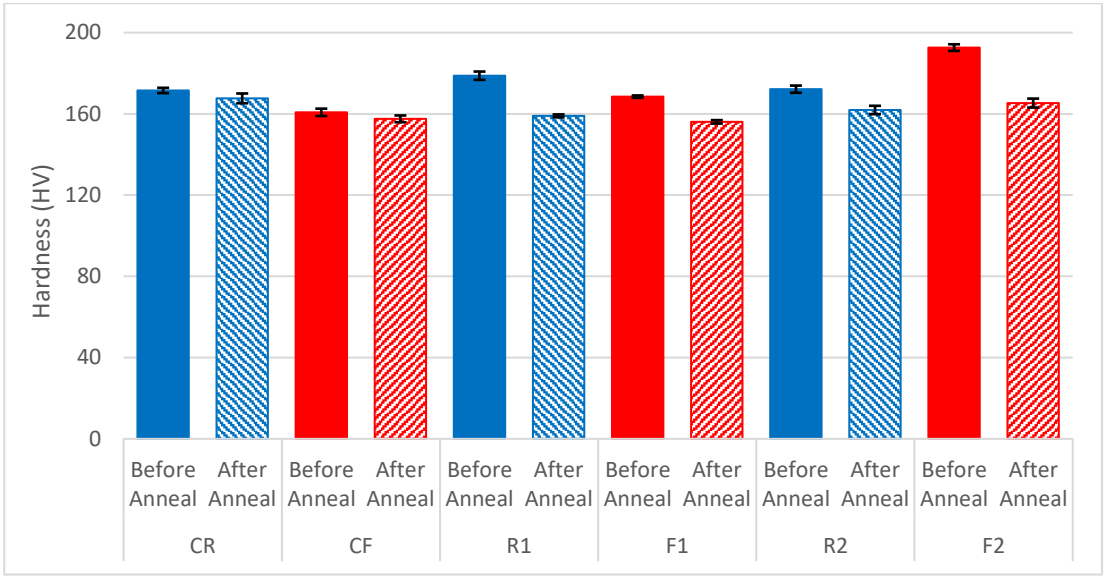

Figure 4-10: Average hardness values for each deformation schedule before and after annealing, raw data in appendix, Table 6-5.

The results from the hardness tests, summarised in Table 4-1, showed that the experimental schedules R1/F1 and R2/F2, with increased strain per pass in the initial passes and increased inter-pass time softened to a far greater extent (7 and 14%) as opposed to the control schedule (2%) after 6 - passes.

Table 4-1: Percentage softening following annealing, negative values denote that the materials hardness naturally decreased following annealing.

	After 3 passes		After 6 passes	
	ΔHV	ΔHV (%)	ΔHV	ΔHV (%)
Control (CR/CF)	-3,0	-2.2	-3,2	-2.0
Increased inter-pass times (R1/F1)	-19,9	-11.1	-12,4	-7.4
Increased inter-pass time and strain (R2/F2)	-10,3	-6.0	-27,3	-14.2

4.3 Optical microscopy

This section presents the microstructural analysis of the sample at different processing stages viz. the roughing, finishing and 4-pass simulation schedules.

4.3.1 Microstructures of the as cast

Figure 4-11 presents optical micrographs of the cast structure at different magnification. The microstructures comprised a single-phase matrix with a crossed-shaped and needle-like precipitates. Precipitates in the chill zone were too fine to characterise even at high magnification. However, precipitates in the equiaxed and columnar regions were aligned differently in different grains [85]. This suggests that precipitate growth had occurred through preferred directions (arrowed in blue, Figure 4-11) i.e., precipitates nucleated after solidification, as predicted by ThermoCalc^{TM} simulations. The directionality of the precipitates has been previously reported by Sello and Bemont [85, 86]. Bemont et al. [85] found through TEM analysis in Fe-C-Nb steel, that in disc-like precipitates, the carbides interphase made an 18º angle with respect to (001) planes and were parallel to the (103) planes of the ferrite matrix. They reported that other work found the matrix/ carbide interface parallel to the (010) ferrite planes. While Sello et al. [86] observed that the Laves phases exhibited relationships of $\{11\bar{2}0\}_{Fe2Nb}$ // $\{111\}_{\alpha}$: $<0001>_{Fe2Nb}$ // $<112>_{\alpha}$ for disc-shaped precipitates and rob shape precipitates having a relationship of $\{11\bar{2}0\}_{Fe2Nb}$ // $\{111\}_{\alpha}$: $<0001>_{Fe2Nb}$ // $<110>_{\alpha}$. Precipitates were found to have preferentially nucleate around inclusions as all inclusions were surrounded by precipitates due to heterogeneous nucleation from lowered activation energy being required [85, 87]. The heterogeneous nucleation is arrowed in green, Figure 4-11.

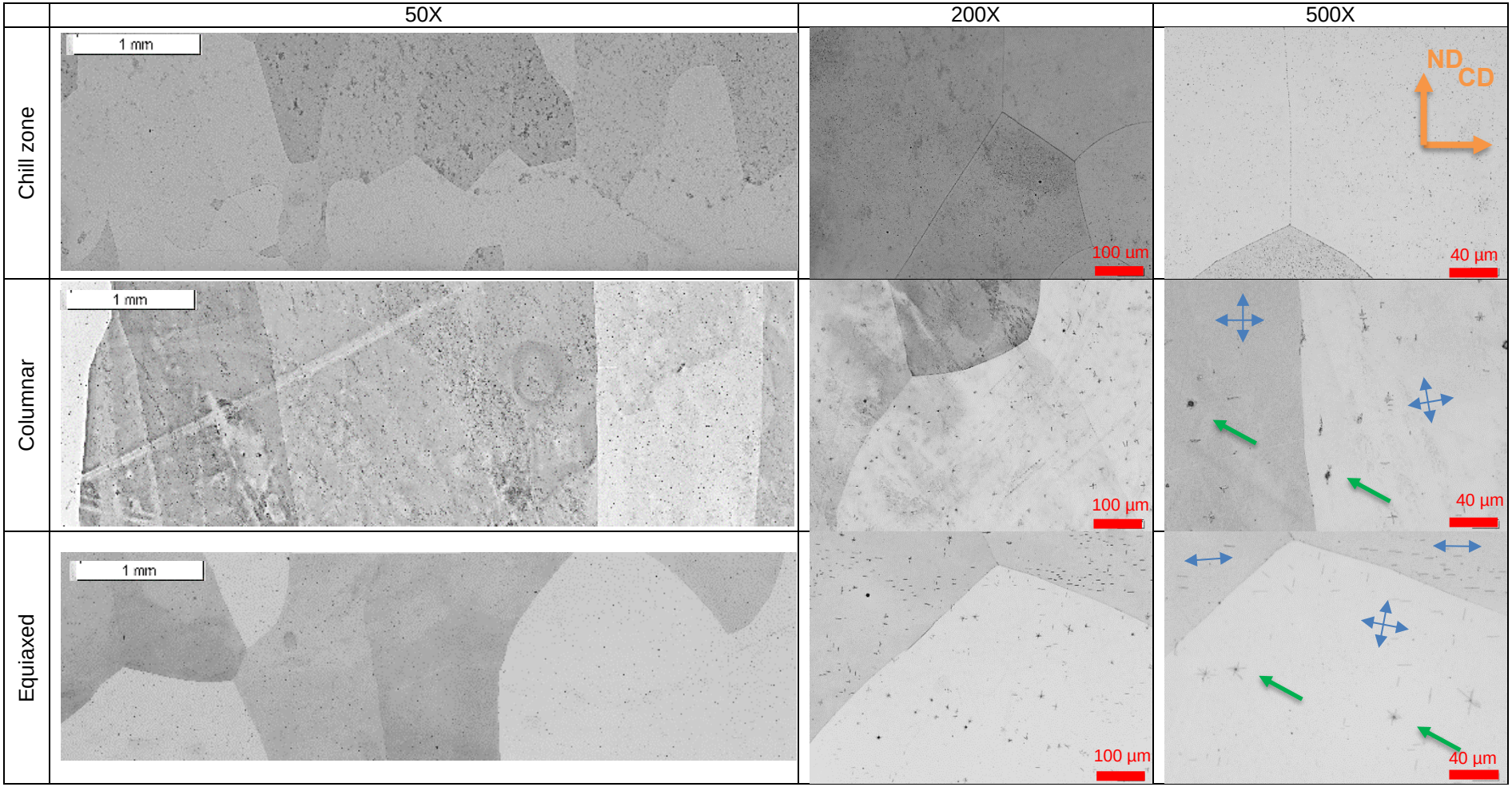

Figure 4-11: Microstructures of the as-cast structures showing large elongated nature of columnar grains, fine grain structure of chill zone and large equiaxed grains at slab centre. Note the directionality of precipitates formed in the material.

Figure 4-12 shows a typical microstructure of the sample in as cast condition. As may be seen, the grains were not only large, but there were no serrations. Grain boundaries in undeformed structures tend to be ‘smooth’ or ‘straight’, having a lower grain boundary curvature to lower the internal energy of the material [18, 58]. The significance of grain boundary serrations is a typical indication of the initiation of DRX. Therefore, any serrations found in deformed and annealed samples can be attributed to the initiation of DDRX, this is elaborated on further in subsequent sections.

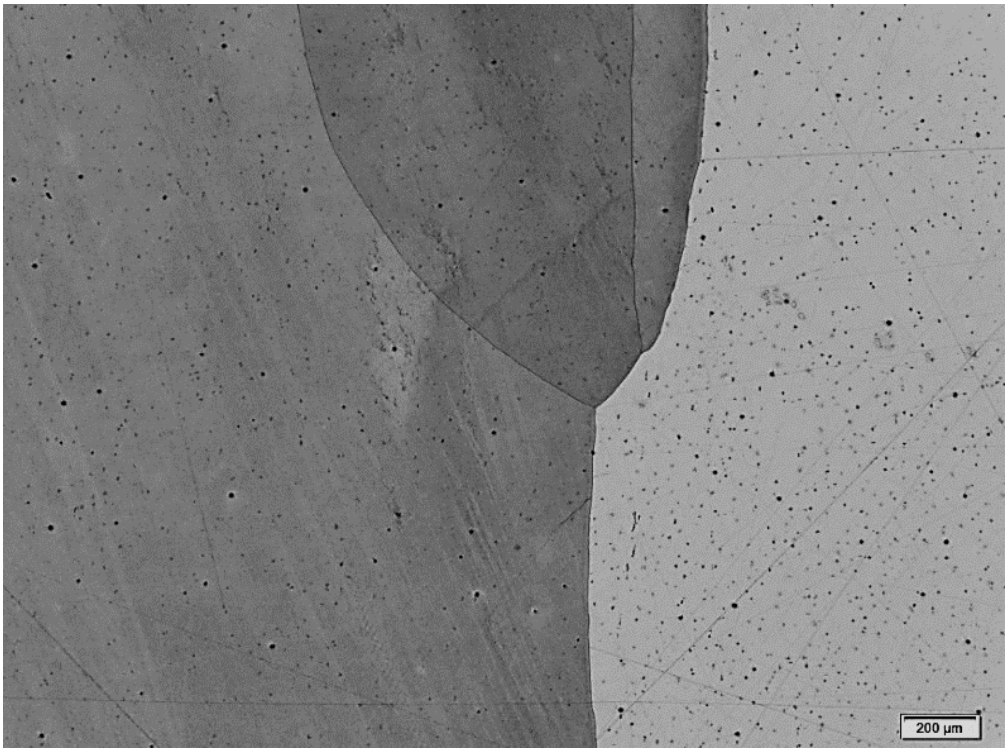

Figure 4-12: General cast structure, showing relatively straight grain boundaries.

4.3.2 Optical micrographs after 3-pass and 4-pass roughing rolling simulations

Figure 4-13 presents optical micrographs of samples subjected to three roughing rolling simulations. Grain curling (arrowed in black) with shear bands, grains aligned along 30-40º to the RD, circled in red. Although most of the cast structure remained largely recovered), recrystallised grains were also visible.

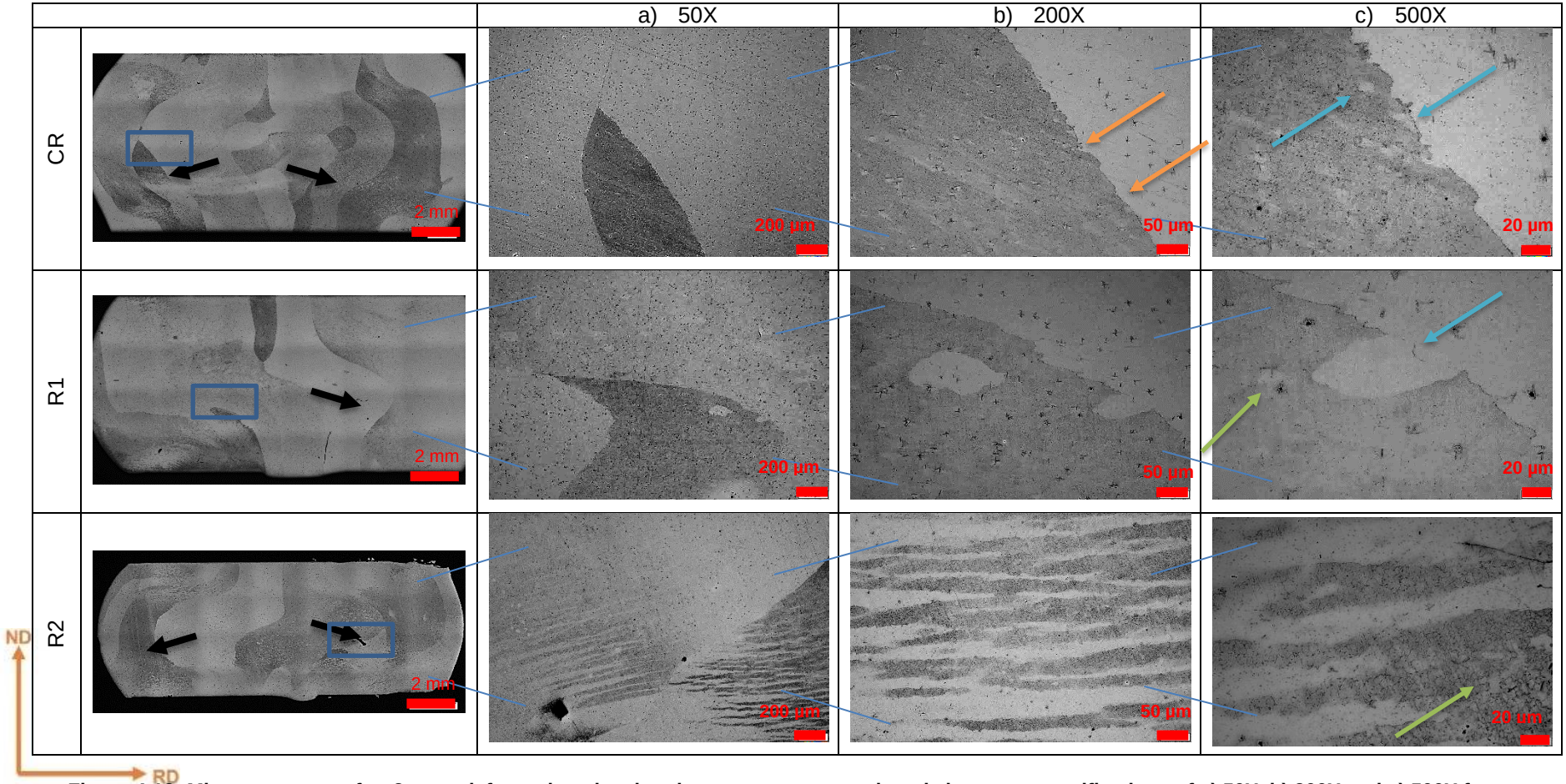

Figure 4-13: Microstructures after 3-pass deformation showing the parent structures largely intact at magnifications of a) 50X, b) 200X and c) 500X for areas encircled in red. Note that microstructures were taken away from dead zones, and not necessarily in the intensive deformation zone. *This was not the case for EBSD analysis where all samples were taken at intensive deformation zone.

		Pass 1	Pass 2	Pass 3
Temperature		1000˚C	950	930˚C
Strain rates		5/s		
Strain	CR R2	0.18 0.24	0.24 0.3	0.3 0.3
Inter-pass time	CR R1 & R2	11 s 15 s	14 s 20 s	18.3 s 25 s

Sample CR in Figure 4-13a showed a large portion of the deformed structure indicating an onset of recrystallisation with some grain boundary serrations (arrowed in orange) and fine, new grains being nucleated (arrowed in blue).

Micrographs of sample R1 presented in Figure 4-13b shows a high concentration of grains having a strong shear morphology. The grain boundaries forming at these 30-40º angles seem to form around star-like precipitates. These precipitates appear to act as the nucleation sites for recrystallisation (arrowed in green). Optical microstructures of sample R2 showed similar structure to sample R1, Figure 4-13.

Figure 4-14 shows micrographs after 4-pass roughing rolling simulations at different inter-pass times and strain rates. All deformation schedules showed substantial recrystallisation. In addition, the 5/s -20s sample showed a high tendency of shear bands and some recrystallised grains. Both 5/s -40s and 15/s -40s inter-pass schedules showed even more recrystallised grains, with 5/s -40s exhibiting larger grain sizes than the 15/s -40s. The slower strain rate allowed more time for dynamic softening mechanisms to be activated, while the longer inter-pass times promoted SRX between passes essentially resulted in even more recrystallisation.

The presence of precipitates around recrystallised grain boundaries in these deformation schedules and deformation schedules preceding this is of significance. Therefore, the benefit can be derived in finding whether these precipitates prevent recrystallised grain growth of newly formed grains or act as nucleation sites, thus, playing a role in particle-stimulated nucleation (PSN).

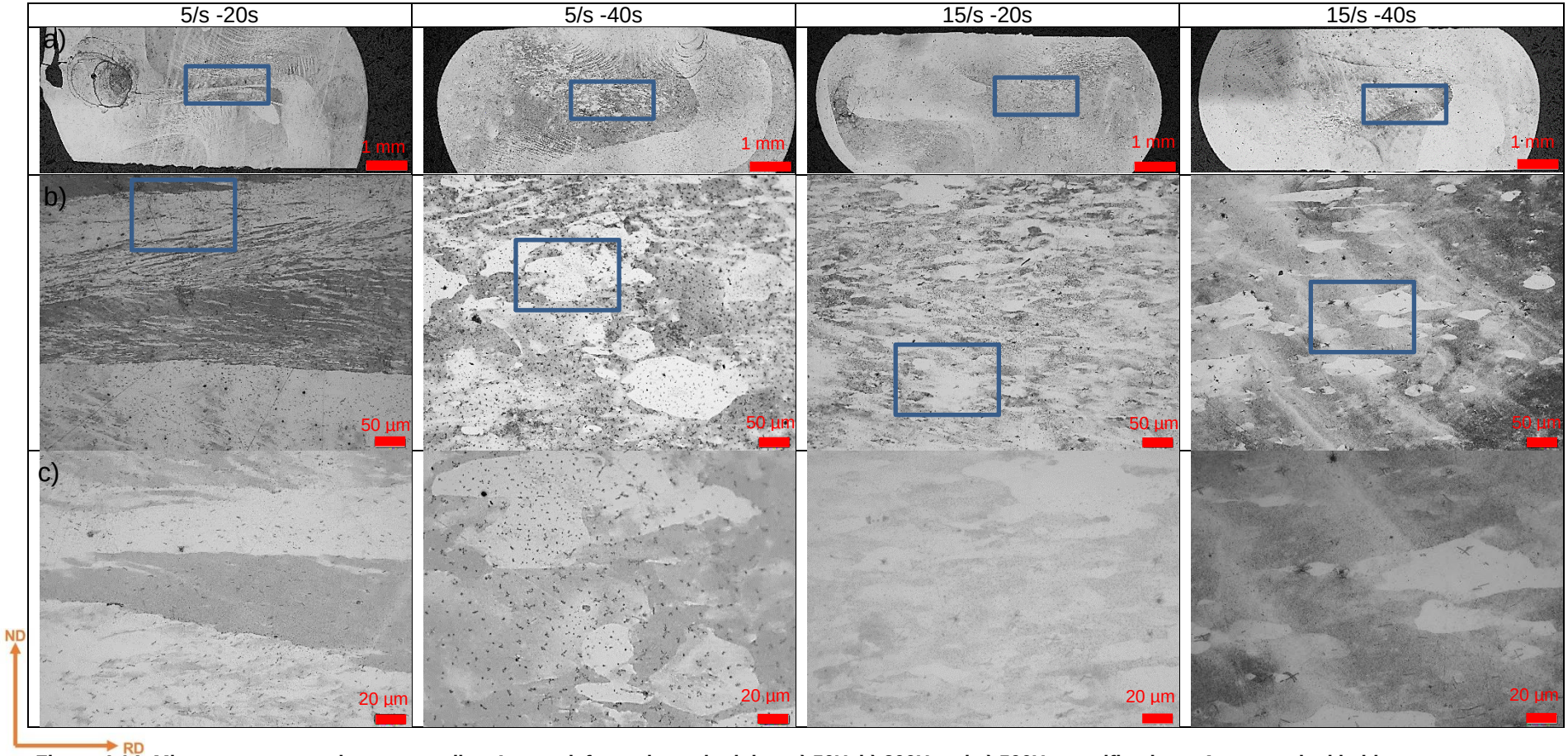

Figure 4-14: Microstructures and corresponding 4-pass deformation schedules, a) 50X, b) 200X and c) 500X magnifications. Areas marked in blue represent areas analysed at higher magnifications.

	Pass 1	Pass 2	Pass 3	Pass 4
Temperature	1000˚C	960˚C	930˚C	900˚C
Strain	0.24	0.3	0.23	0.23
Inter-pass time	20 s or 40 s			
Strain rates	5/s or 15/s			

4.3.3 Optical micrographs of samples subjected to 6-pass roughing & finishing simulations

Figure 4-15 presents micrographs for the finishing rolling simulations exhibiting a pronounced banded structure. The grains appeared to have been broken down with much clearer areas of recrystallisation being visible. The CF sample showed what would seem to be geometric dynamic recrystallisation (GDRX) when flattened grains result in pinching off of grains with small sub-grain sizes (arrowed in purple). Grains had also recrystallised within other grains (arrowed in maroon), sample F1. The grains were fine and of uneven shape. Recrystallisation within grain boundaries typically occurs through CDRX, where sub-grain structures increase misorientations forming new grains. The micrographs of sample F2 show an area of grain boundary migration (arrowed in yellow). Grain boundary migration is typical in DDRX, where grain boundaries move and pinch off their parent grain [20, 23, 63]. The grain boundary movement from a grain with high deformation energy to low deformation energy is driven by the reduction in stored energy.

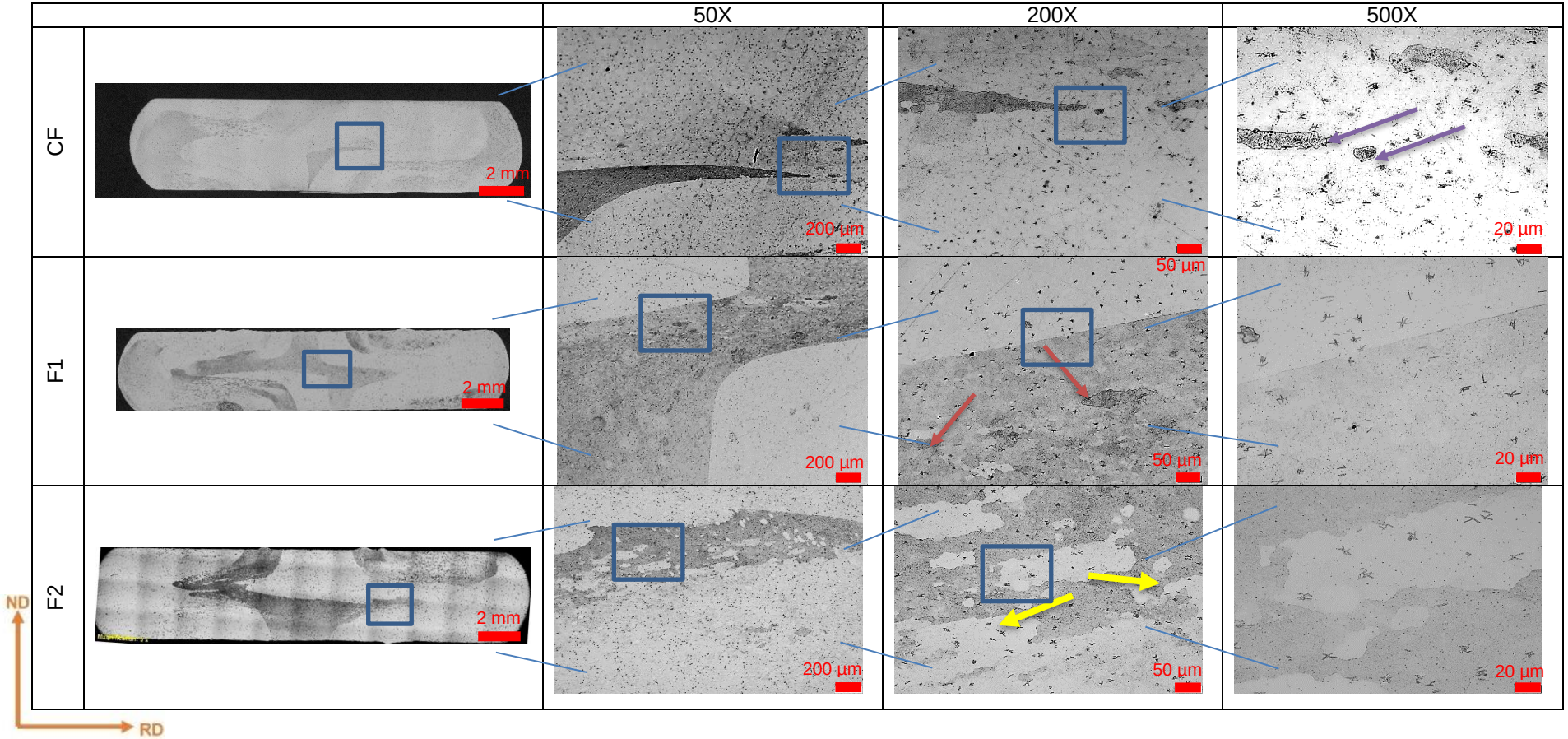

Figure 4-15: Microstructures of CF, F1 and F2 after 6-pass deformation at 50X; and 200X and 500X for areas demarcated by blue.

		Pass 1	Pass 2	Pass 3	Pass 4	Pass 5	Pass 6
Temperature		1000˚C	950	930˚C	920˚C	920˚C	900˚C
Strain rates		5/s					
Strain	CF F2	0.18 0.24	0.24 0.3	0.3 0.3	0.2	0.2	0.2
Inter-pass time	CF F1 & F2	11 s 15 s	14 s 20 s	18.3 s 25 s	36 s	38 s	52 s

CF sample showing the presence of GDRX initiating and occurring is evident in Figure 4-16. Typically, this occurs at strains more significant than 1. So, it is unexpected to observe GDRX at even lower strains. However, GDRX might have taken place with the aid of the localised retained strain. Huang and Loge [16] noted that GDRX occurs above a strain of 1 in Al alloys.

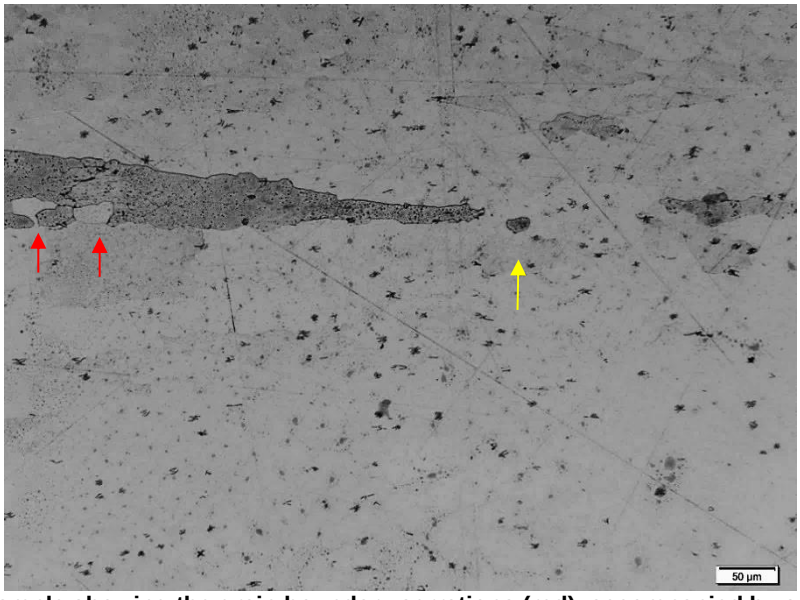

Figure 4-16: CF sample showing the grain boundary serrations (red), accompanied by a pinched-off grain (yellow) resulting from GDRX.

4.4 Electron backscattered diffraction analysis

4.4.1 Texture of the as-cast structure

EBSD and corresponding ODF maps of the cast structure are contained in Figure 4-17.

Figure 4-17a corresponds to the columnar structure, Figure 4-17b to the equiaxed zone and Figure 4-17c to the chill zone. The cast structure analysis was done with large step sizes to attain a large area of analysis of the cast structure.

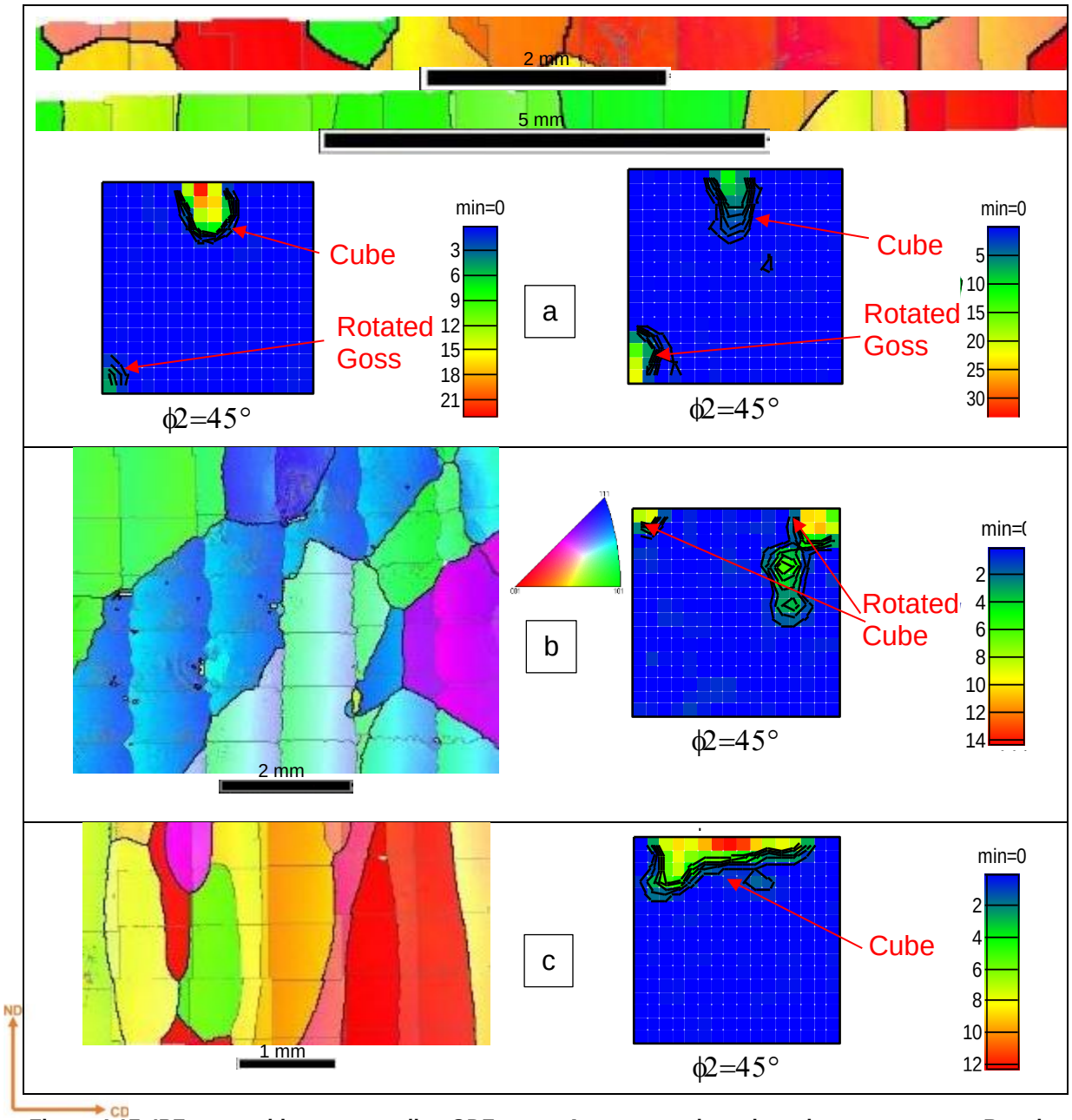

Figure 4-17: IPF maps with corresponding ODF maps, A corresponds to the columnar structure, B to the equiaxed zone and C to the chill zone. Cube grains are red and Goss are green.

High angle grain boundaries (HAGB) are defined as having misorientations above 15º, whilst low angle boundaries (LAGB) are between 2º and 15º, sometimes referred to as sub-grains [43, 95]. Figure 4-18 shows the columnar structure at high-magnification with the absence of LAGB, as expected. The presence of grain boundary pinning [88] by particles is also observed. The grain boundary pinning resists grain rotation during hot deformation.

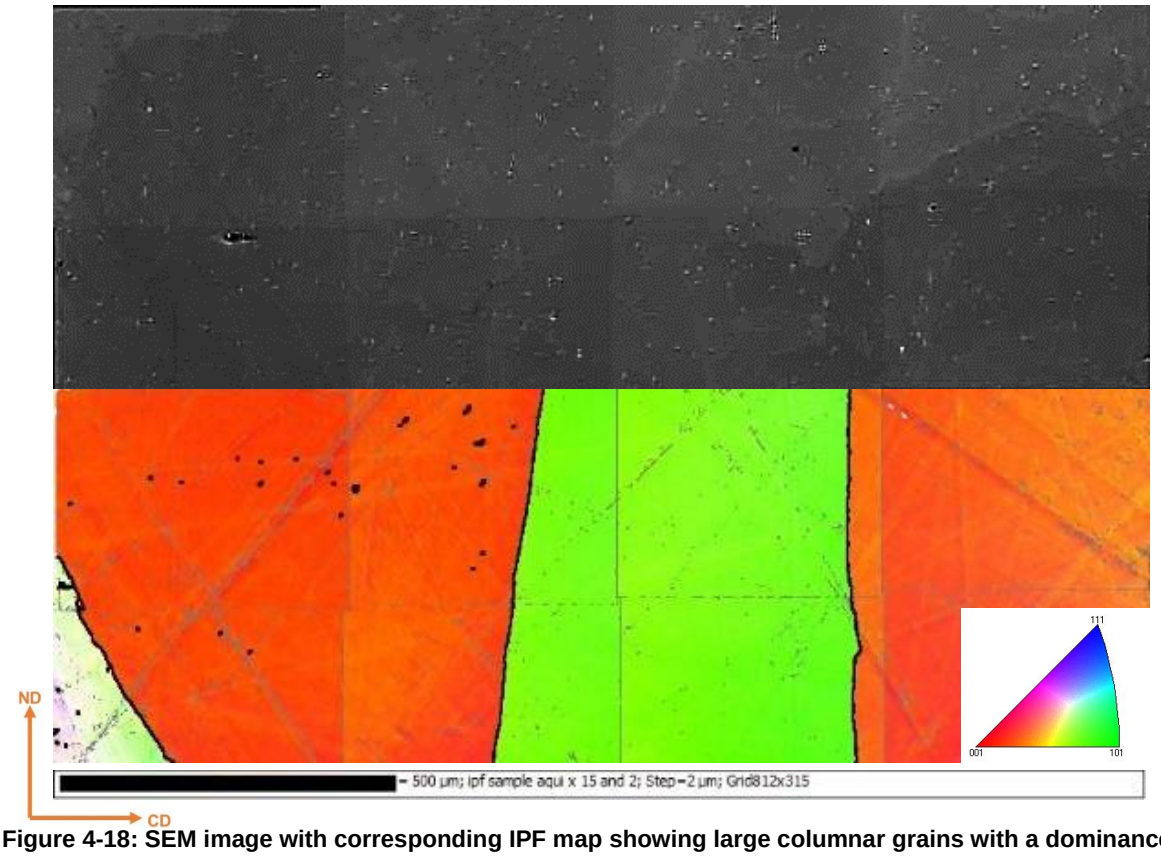

Figure 4-18: SEM image with corresponding IPF map showing large columnar grains with a dominance of 001 and 101 orientations along the cast direction (CD) at high magnification under a 2µm step size.

The cast structure shows apparent variations in the orientation of grains between the equiaxed and columnar zone. The chill zone seems to maintain a similar orientation to the columnar region, maintaining a Cube texture with elements of rotated Goss texture in agreement with previous researchers that studied the cast structure [23, 28]. Liu [28] observed random orientations in the equiaxed region but in this study rotated Cube texture was observed for the area analysed. Characterisation of the initial cast texture is important as texture is often inherited from upstream processes [18, 71].

Figure 4-19 presents the as-cast misorientation angle distribution (MAD) corresponding to Figure 4-18. Low-angle grain boundaries that show up on the misorientation angle distribution are likely due to the scratches on the cast sample due to the relative softness of the cast material and stitching multiple frames together. The uncorrelated misorientation data shows the change in misorientation within a grain. The correlated data shows misorientation between neighbouring points.

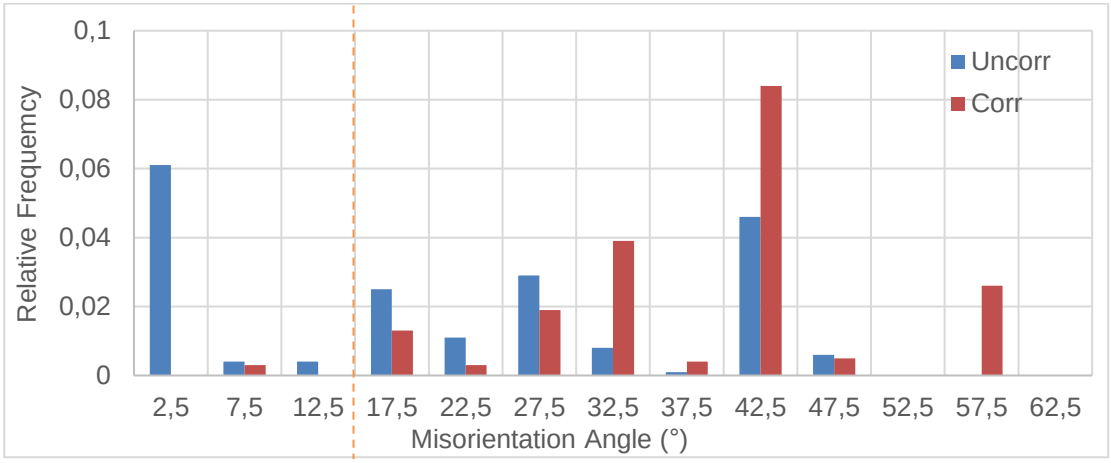

Figure 4-19: Correlated (Corr) and uncorrelated (Uncorr) misorientation angle distribution for the cast structure.

Effectively, the cast structure was characterised by a significant proportion of high-angle grain boundaries, with mostly Cube-orientated grains known to be a challenge to recrystallise. As expected, the cast structure exhibited minimal low-angle grain boundaries. Therefore, any low-angle grain boundaries and sub-grains that form in subsequent processing resulted from the hot deformation.

4.4.2 EBSD analysis after 3-pass and 4-pass simulated roughing rolling

After 3-pass deformation, the precipitates aligned with the sheared grains, Figure 4-20 and Figure 4-28. The formation of shear bands was associated with grain curling. From the CR sample, the presence of grain boundary serrations is evident of the initiation of DDRX. The presence of PSN is apparent in the R1 and R2 samples, both of which were subjected to increased inter-pass times. For all samples, the parent grains are still visible even though some recrystallisation was initiated. Hence, softening was primarily through recovery as opposed to recrystallisation.

Figure 4-20 shows micro-shear bands. Micro-shear bands form within grains and they form corrugations/serrations when they reach the grain boundaries [20,23]. These micro-shear bands are associated with the precipitates in the matrix.

In Figure 4-20a, the central grain in red in the texture map has a Cube texture, and the sample seems to be moving away from the Cube orientation. It is noted that the high-angle grain boundaries within this Cube grain are lower than the high-angle grain

boundaries found in the grain to the left of the Cube grain. Recrystallisation in the left grain has Brass orientations (blue on the texture map), and the grain is found to recrystallise easier than the central Cube grain. Based on the ODF image, it can be said that the central Cube grain is moving towards rotated Cube orientation.

The process conditions for R1 (Figure 4-19b) differed from CR (Figure 4-20a) because it had a longer inter-pass time, which allowed for the nucleation of new grains through SRX. As may be seen, recrystallised grains in the parent grain are aligned to 30 - 40º angles to the rolling direction (depicted by RD on Figure 4-20), typical of SRX in shear bands. Grains recrystallised with Cube (red), Gamma (blue) and Alpha (green) textures, in Figure 4-20.

Analysis of sample R2 (Figure 4-20c) shows clear evidence of shear bands; however, the amount of recrystallisation is minimal compared to the CR and R1 schedules, even though the total strain was higher than the other two deformation schedules. As strain per pass in R2 was higher than CR and R1, the lack of recrystallised grains suggests that energy was restored through recovery before subsequent simulated finishing rolling process.

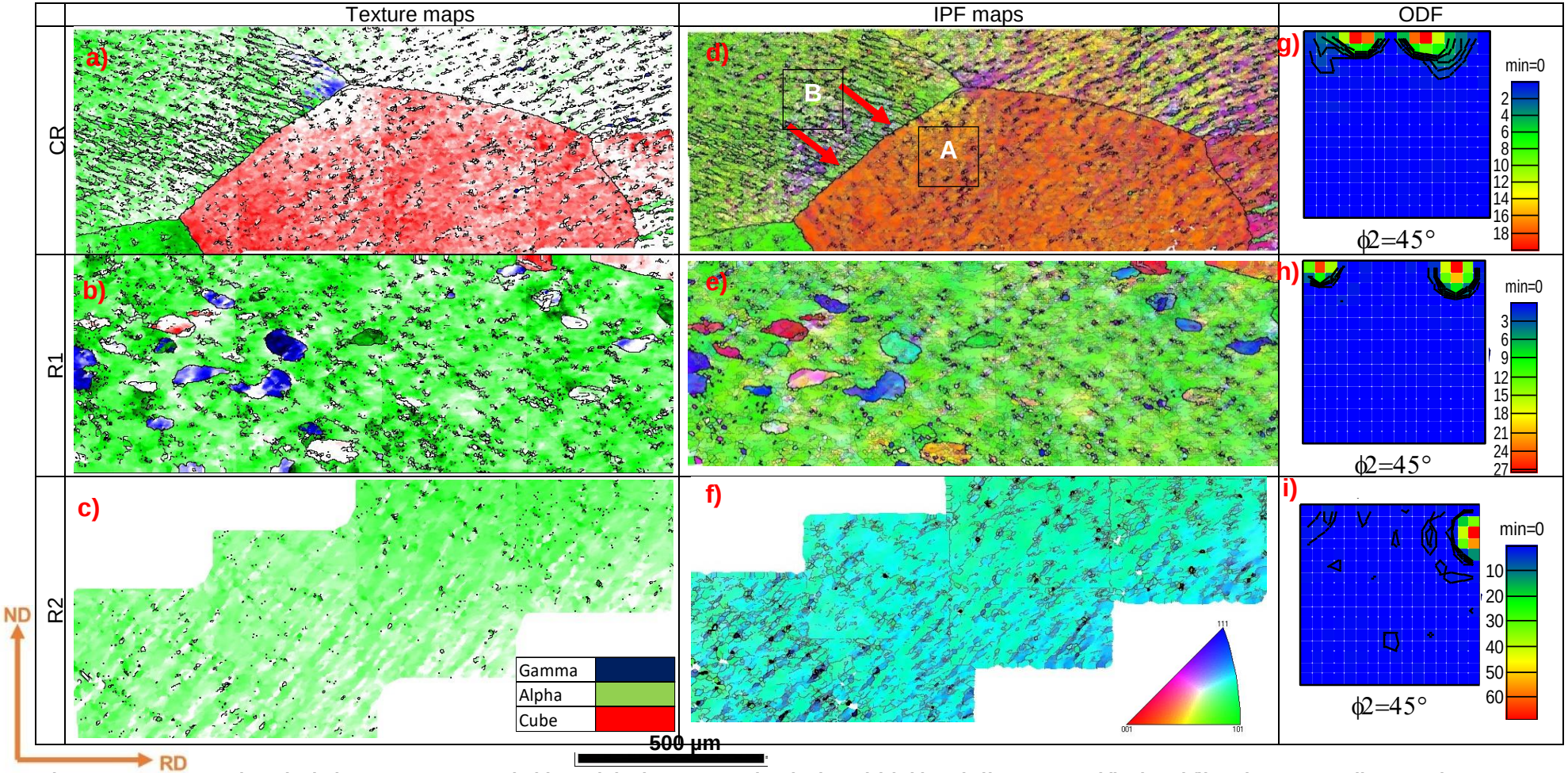

Figure 4-20: Texture plots depicting Gamma texture in blue, Alpha in green, and Cube in red (a), b) and c)), IPF maps (d), e) and f)) and corresponding ODF images (g), h) and i)) for samples CR, R1 and R2 samples. Note areas A and B analysed later in text.

		Pass 1	Pass 2	Pass 3
Temperature		1000 C	950	930 C
Strain rates		5/s		
Strain	CR R2	0.18 0.24	0.24 0.3	0.3 0.3
Inter-pass time	CR R1 & R2	11 s 15 s	14 s 20 s	18.3 s 25 s

The CR sample had much of the parent grain orientation visible. As such, deformation behaviour within the different grain orientations was studied to identify the different recrystallisation behaviour, particularly on a grain conforming to a Cubic texture and one to a non-cubic texture. The non-cubic grain in Figure 4-20a had its <101>//RD. The MAD data of single grains in the CR sample is presented in Figure 4-21.

From the uncorrelated data (Figure 4-21a), it has been found that the general structure within the non-cubic grain is random, with orientations differing greatly within the sample, having multiple misorientations greater than 15º. It is noted that the Cubic grain is defined by small misorientations relative to the general structure, with misorientations peaking below 15º. When misorientations peak below 15º, it points to the view that minimal recrystallisation occurred in the Cubic grain, conforming to what has been previously reported [23, 28], although restoration was not necessarily expected at these strains, it was observed. Figure 4-21b, from correlated data, shows that the general structure has a large number of low-angle orientations and sub-grains. For the Cubic grain, the uncorrelated data shows that there are large deviations in grain orientation, whilst the correlated data shows no direct concentrations of high-angle grain boundaries. This observation suggests that there is a continuous change in grain orientation in the material, typical of grain rotation during CDRX.

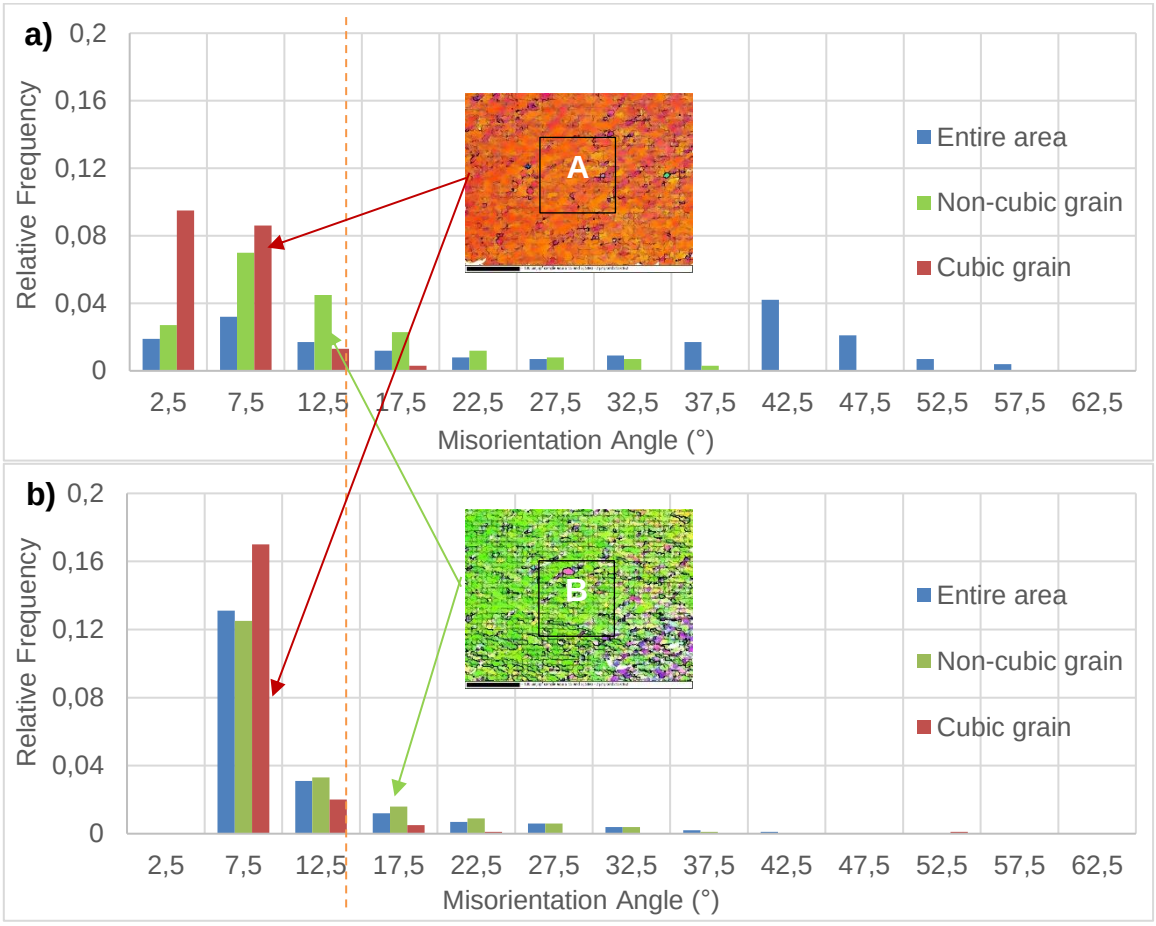

Figure 4-21: a) Uncorrelated and, b) correlated misorientation angle distribution data of CR for the grains in question and the entire area of the structure.

Figure 4-22 presents the misorientation angle distribution (MAD) data for samples CR, R1 and R2. These MADs are for the areas analysed in Figure 4-20.

The control (CR) shows a scatter in orientations of the sample when looking at the uncorrelated data (Figure 4-22a). For the R1 and R2 samples, the misorientations of grains are minimal in the overall structure in that majority of the area has low misorientations to each other. It is seen from correlated data (Figure 4-22b), which gives insight into grain boundary misorientations, that for the CR sample misorientations for neighbouring pixels are primarily low angle misorientations. Essentially, this would mean that the sample has a large amount of LAGB and sub-grain boundaries. These sub-grains have low-angle boundaries within the grain they formed. From correlated misorientation data, the control sample that simulated industrial process, CR, showed the onset of sub-grain formation through the formation of a high density of LAGB. This randomised the overall grain orientation as evident

from the MAD of uncorrelated data. R1 and R2 samples show similar behaviour in that the uncorrelated data shows low misorientations. Correlated data for R1 and R2 show that the creation of high-angle grain boundaries took place resulting in partial breaking down of the texture in the area observed, a quantitative analysis of recrystallisation within grains and associated recrystallisation maps are contained in the Appendix, Figure 6-4. R1 and R2 show that recrystallised grains had 25 - 35º misorientation from the parent structure. Therefore, it can be said that recrystallised grains had an effect of preferentially nucleating a specific grain orientation. The recrystallisation from the R1 and R2 samples are likely due to the increased inter-pass time that promoted the SRX.

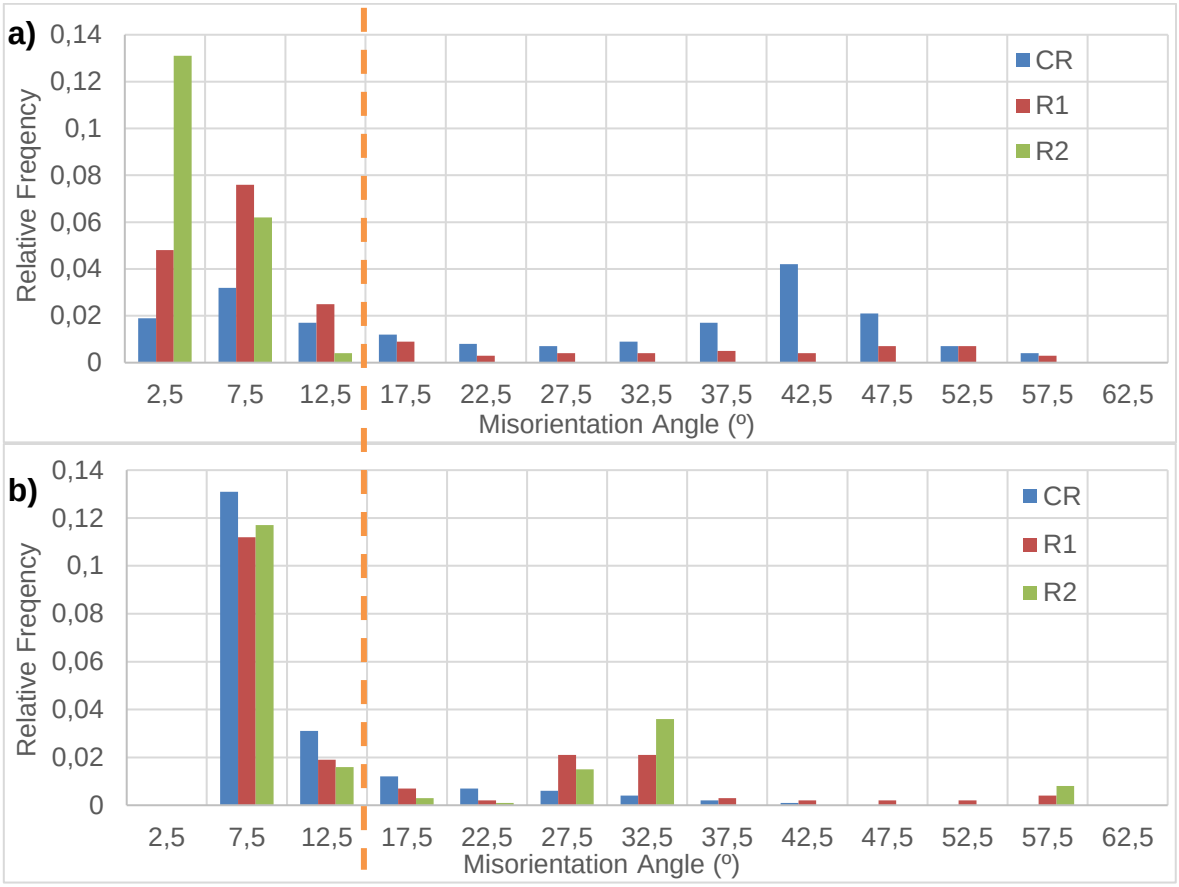

Figure 4-22: a) Uncorrelated and b) correlated misorientation angle distribution data for samples CR, R1 and R2.

As mentioned earlier, the higher degree of HAGB from the correlated data in sample R2 would have resulted from the higher driving force for texture randomisation of recrystallised grains for the area observed in Figure 4-20c.

Figure 4-23 shows the results of the 3-pass high strain rate schedules (15/s). The recrystallisation that occurs along the shear bands emanates from precipitates. These are shear bands, as low angle grain boundaries are aligned to 30 - 40º to the rolling direction, and areas with recrystallisation are found along these 'bands' due to the high strain levels associated with these regions. These bands are arrowed in white, and the areas recrystallised are circled. As may be seen, the parent grains conform to a Cube texture. With the increased strain rate, shearing within grains was favorable [16, 56]. It can be deduced that the formation of the micro shear bands plays a substantial role in the breakdown of the as cast Cube texture as they act as sites for DDRX [16, 27].

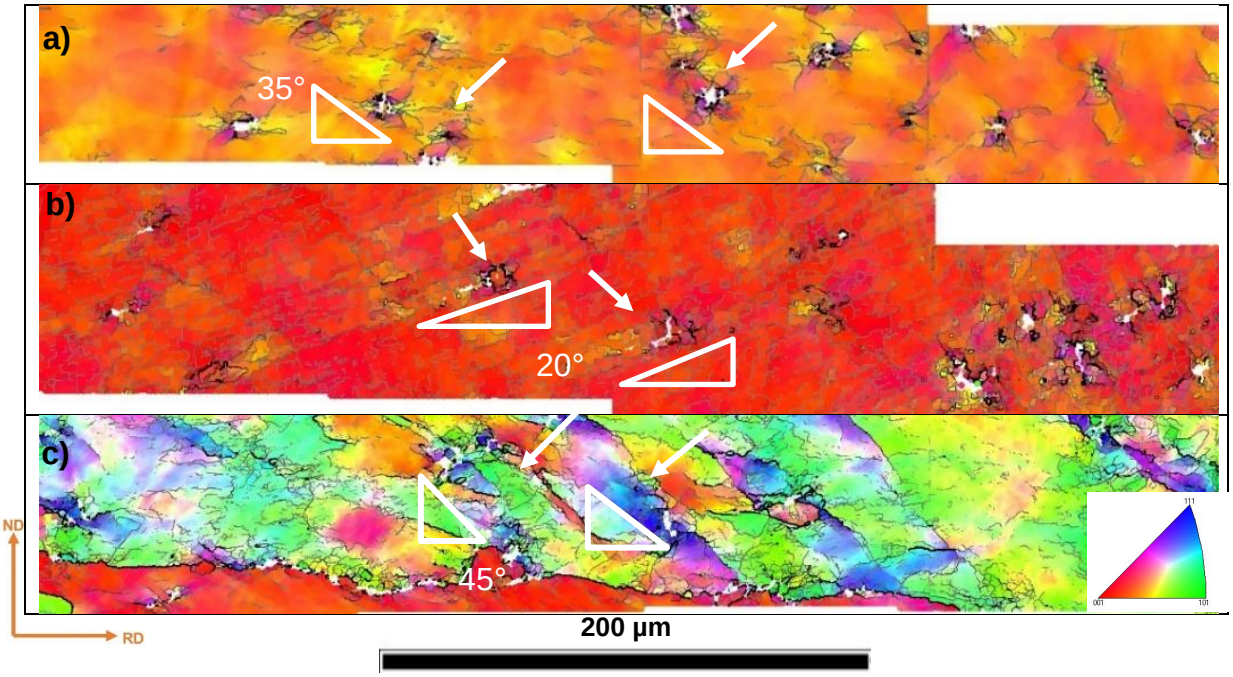

Figure 4-23: IPF maps of a) CR- 15/s, b) R1-15/s and c) R2-15/s 3-pass simulations, showing recrystallisation along shear bands.

Four-pass schedules were undertaken to study the effects of strain rate and inter-pass time independently and the results are presented in

Figure 4-24. As may be seen, the short inter-pass time of 20 s resulted in finer recrystallised grains with a more deformed structure and sub-grains.

It is evident from the ODF maps in

Figure 4-24e, f, g and h, that with the as cast strong Cube texture was difficult to break down as it was shifted to rotated Cube orientation. The long inter-pass and low strain

rate resulted in some Gamma fibre texture (arrowed in white) from the strong Cubic texture, further imaging is contained in Appendix (Figure 6-9).

An in-depth analysis of results for the four pass simulations was undertaken in a conference proceeding [89]. Like previous tests, recrystallisation within the samples did not reach completion. However, there is a difference in the recrystallisation behaviour among the samples. All areas analysed in

Figure 4-24 show that the parent grain have Cube texture. Using correlated data,

Figure 4-24i and j, to understand grain boundary behaviour, it showed that neighbouring grains have a high degree of LAGB at high strain rates, typical of the onset of CDRX mechanisms.

Figure 4-24i shows that for a sample at low strain rates, adjacent pixels have a high degree of high-angle boundaries, which is typical of DRX.

Figure 4-25 presents 4-pass deformation under low strain rate and short inter-pass time, region A in

Figure 4-24a. As may be seen, recrystallisation was also possible through DDRX under the short inter-pass time and low strain rate, whereby a necklace structure occurred around grain boundaries [16], arrowed in blue. The recrystallisation occurs along newly formed grains through nucleation on the grain boundaries, showing that it is possible to initiate recrystallisation from newly formed grains during deformation. Therefore, initiating recrystallisation and growth would allow for further recrystallisation, eventually leading to the complete breakdown of the parent grain.

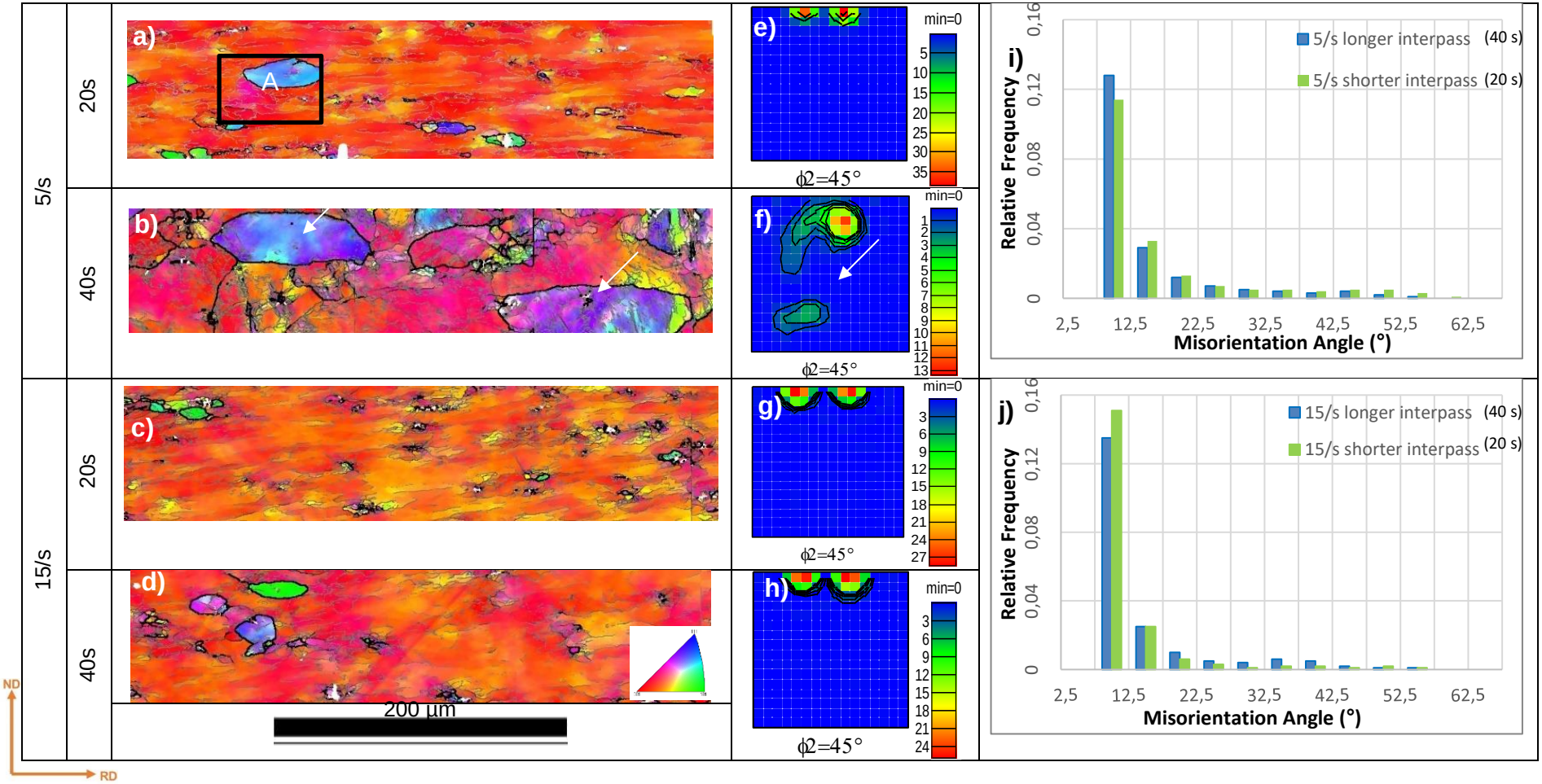

Figure 4-24: IPF and ODF images, for 5 /s strain rates and 20 s inter-pass times, a) and e); 5 /s strain rates and 40 s inter-pass times, b) and f); 15 /s strain rates and 20 s inter-pass times, c) and g); and 15 /s strain rates and 40 s inter-pass times, d) and h) for 4-pass deformation schedules with corresponding Correlated MAD data for a) 5 /s strain rates and b) 15 /s strain rates. Area A demarcated for further analysis in Figure 4-25 [89].

	Pass 1	Pass 2	Pass 3	Pass 4
Temperature	1000˚C	960˚C	930˚C	900˚C
Strain	0.24	0.3	0.23	0.23
Inter-pass time	20 s or 40 s			
Strain rate	5/s or 15/s			

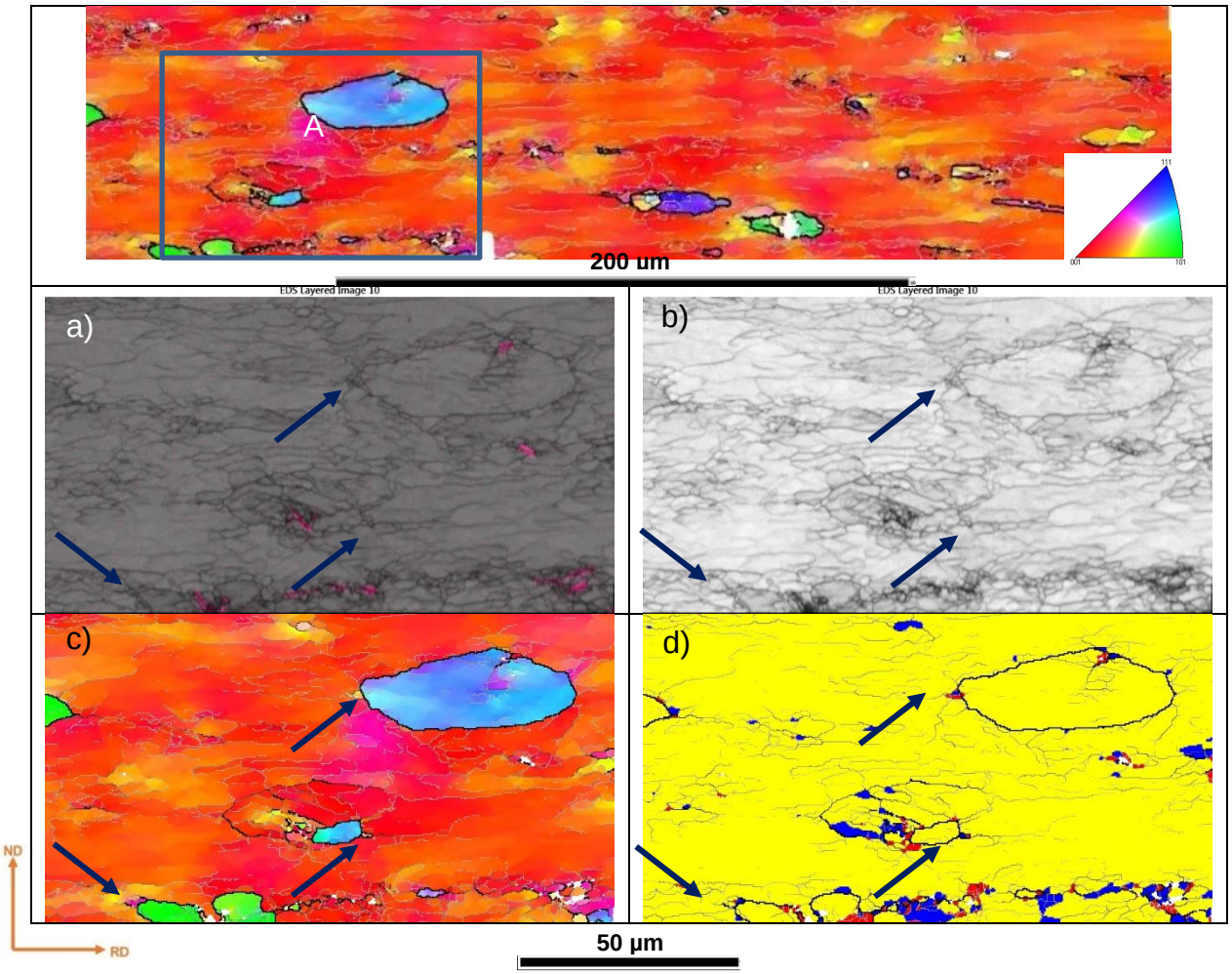

Figure 4-25: a) Band contrast image overlaid with the Nb map, b) band contrast image, c) IPF image, and d) recrystallisation fraction map of area A demarcated in Figure 4-24. the

4.4.3 EBSD analysis of 3-pass roughing and 6-pass finishing rolling simulations

Figure 4-26 presents MADs for 3 versus 6-pass schedules in as hot worked condition for the simulated plant conditions and Figure 4-27 compares the corresponding IPF maps. As may be seen from Figure 4-26a, 3-pass schedule yielded larger HAGB densities, from Figure 4-27, these were located mostly around precipitates. The 6-pass schedules, however, exhibited a well-defined sub-grain boundary network, typical evidence of the onset of CDRX [16], which resulted in high frequency of low angle misorientations. Of note is that these low-angle grain boundary networks show evidence of having emanated from precipitates after 6-passes, Figure 4-27.

Sample R1 (Figure 4-27b) shows the distribution of LAGB in the structure, depicted by the grey boundaries with a concentration of HAGB around precipitates, depicted by the black boundaries (< 15°). After 6-passes, the structure showed a well-defined sub-grain structure network, with a shift in orientations from the parent orientation Figure 4-27d, e and f.

The presence of DRX seems to be more pronounced in 6-pass than 3-pass schedules with recrystallisation within the grain typical of the process of CDRX, where grains form new orientations with the parent grain.

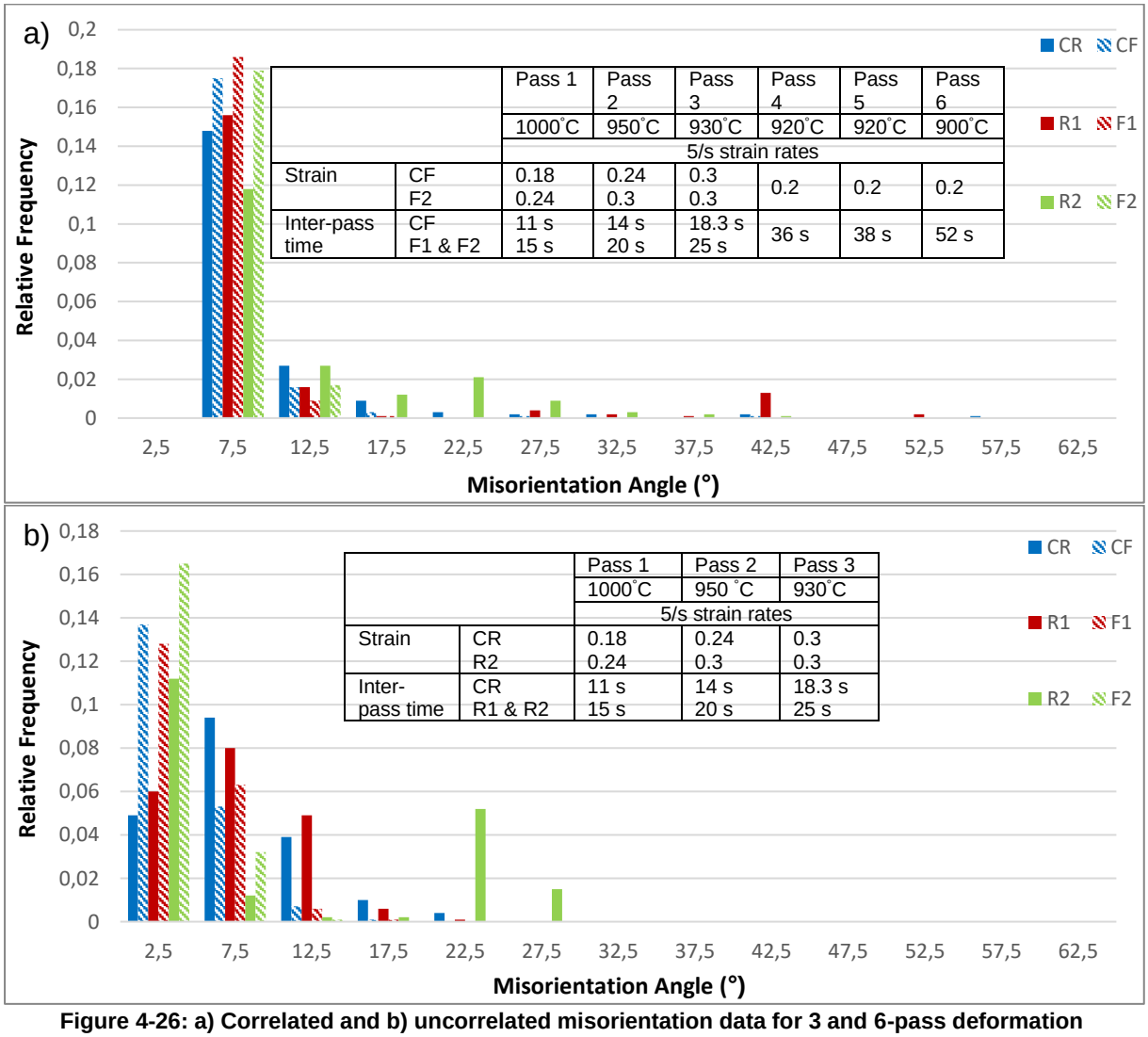

Figure 4-26: a) Correlated and b) uncorrelated misorientation data for 3 and 6-pass deformation schedules for the IPF maps contained in Figure 4-27.

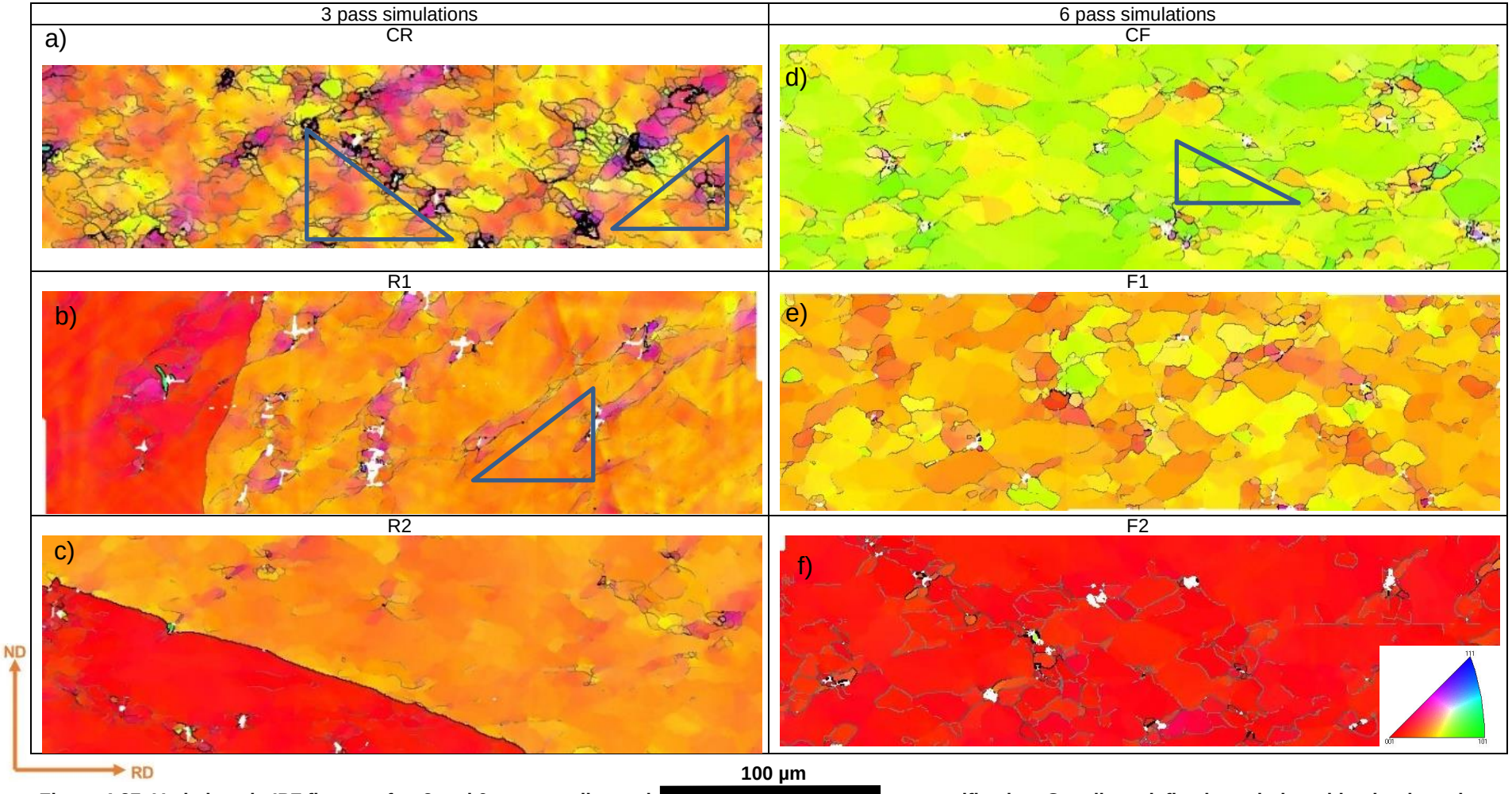

Figure 4-27: Variations in IPF figures after 3 and 6-passes, all samples are observed at the same magnification. Grey lines define boundaries with misorientations below 15°, and black lines, for boundaries greater than 15°. Recrystallisation maps can be found in Figure 6-7.

4.4.4 Dynamic softening assisted by particle stimulated nucleation

Figure 4-28 shows typical examples of various dynamic softening mechanisms during the 3-pass roughing rolling simulation. The presence of shear bands is typical of the initiation of CDRX processes, whilst grain boundary serrations and migration indicate the start of DDRX, where these serrations would eventually lead to a necklace structure around the grains [20, 63].

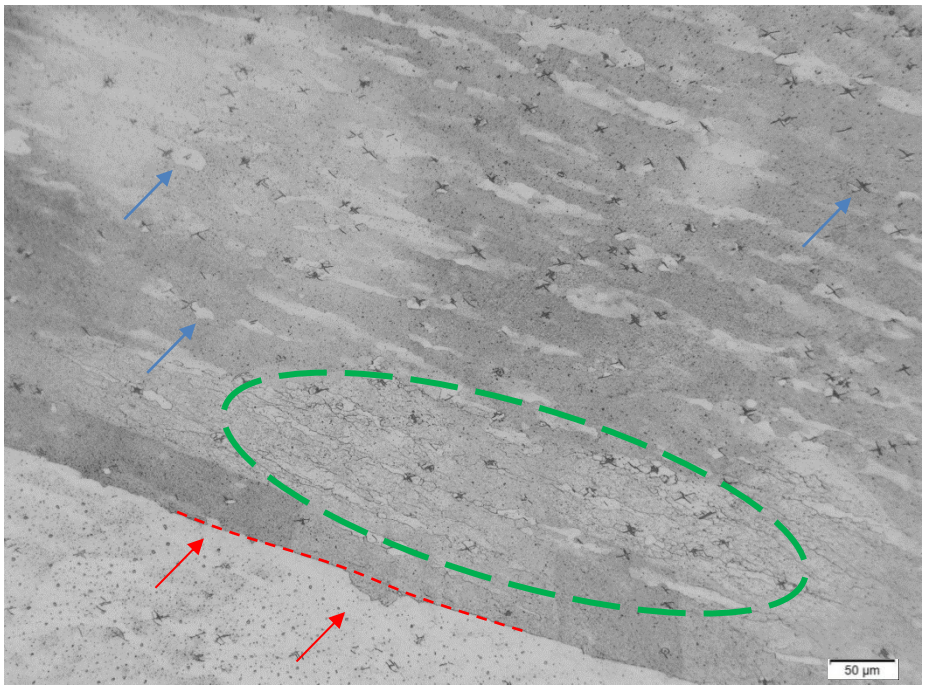

Figure 4-28: Optical micrograph showing strain induced boundary migration (SIBM), arrowed in red, PSN (arrowed in blue) and shear bands (depicted in green) for sample R1 taken at 200X.

High magnification results for the 3-pass roughing rolling simulations at a strain rate of 5 /s are presented in Figure 4-29. CR showed a relatively higher volume fraction of recrystallised grains, Figure 4-29d. The recrystallised grains (Figure 4-29g, h, i) were found to be concentrated around areas with precipitates (circled in red). The grain boundary seems to be migrating into the grain on the left, evident by the bulging of the grain boundary (arrowed in blue). The grain on the left seems to have fewer recrystallised grains and a lower density of precipitates. Similar observations were made in R1, Figure 4-29e. Notice is made again that the evidence of recrystallisation is low when

precipitate density is low. As may be seen, the area analysed in R2, Figure 4-29f, has much finer precipitates than CR and R1. This resulted in almost no recrystallisation implying that there is a critical size for PSN as a mechanism for grain refinement [49]. In this work, the average particle size was found to be 5 µm for the CR while for the R1 and R2 sample it averaged to 7 µm, likely due to longer interpass times. PSN generally occurs around non-deformable particles as a result of strain localization around these particles, which leads to DRX.

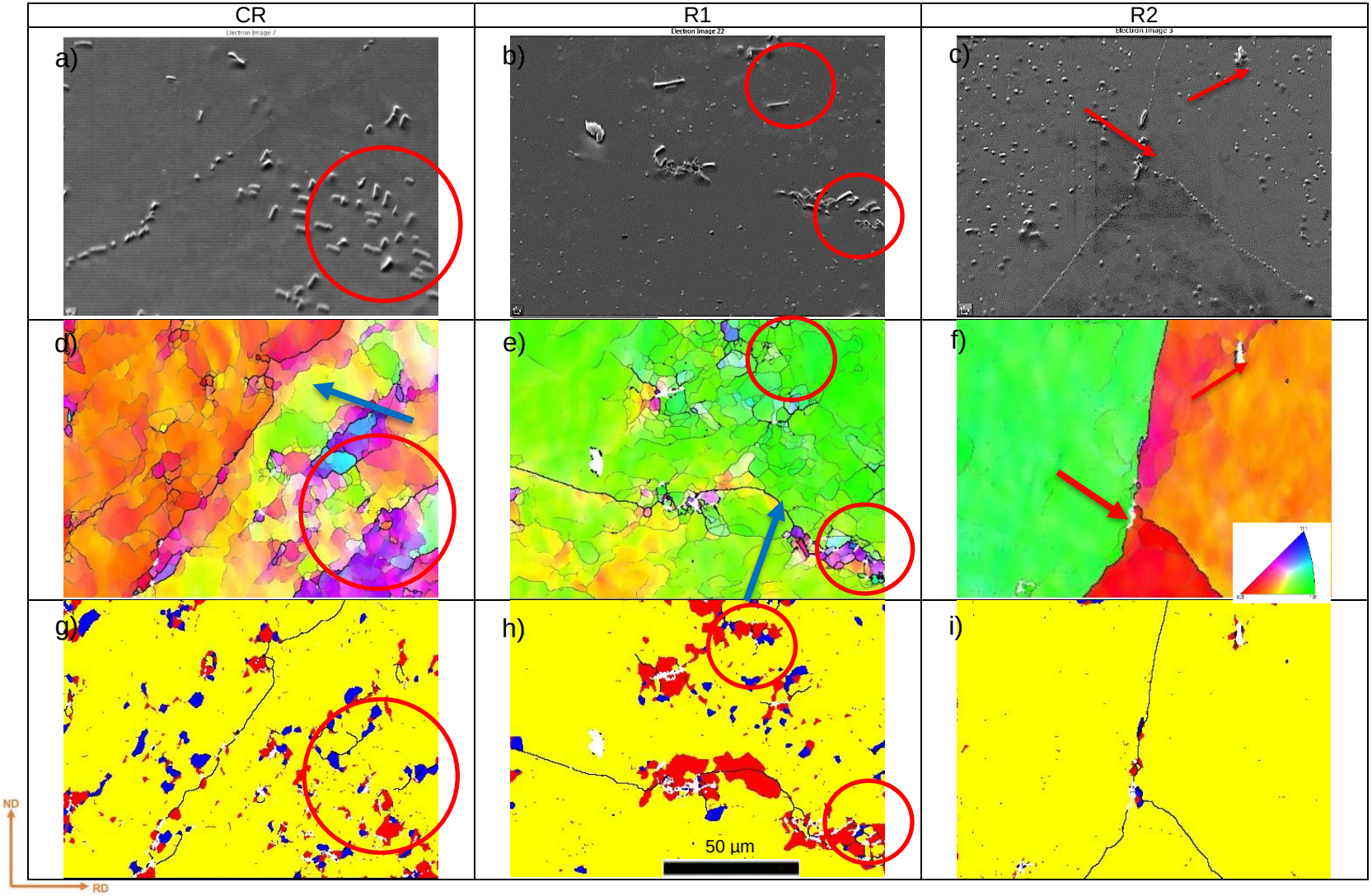

Figure 4-29: High magnification SEM images (a, b, c) with corresponding IPF plots (d, e, f) and recrystallisation plots (g, h, i) for 3-pass simulation of CR, R1 and R2 with red representing deformed material, yellow representing substructure material and blue representing recrystallised material.

Figure 4-30 shows PSN in 3-pass schedules at a strain rate of 15 /s and a similar trend is observed. However, for sample R2 -15/s the LAGB structure seemed to have covered the entire parent grain with the newly formed grains aligned to the micro shear bands, resulting in the breakdown of texture in the parent grain. No significant difference was observed after hot rolling at 15 /s with an inter-pass time of 40 s in 4-passes, Figure 4-31.

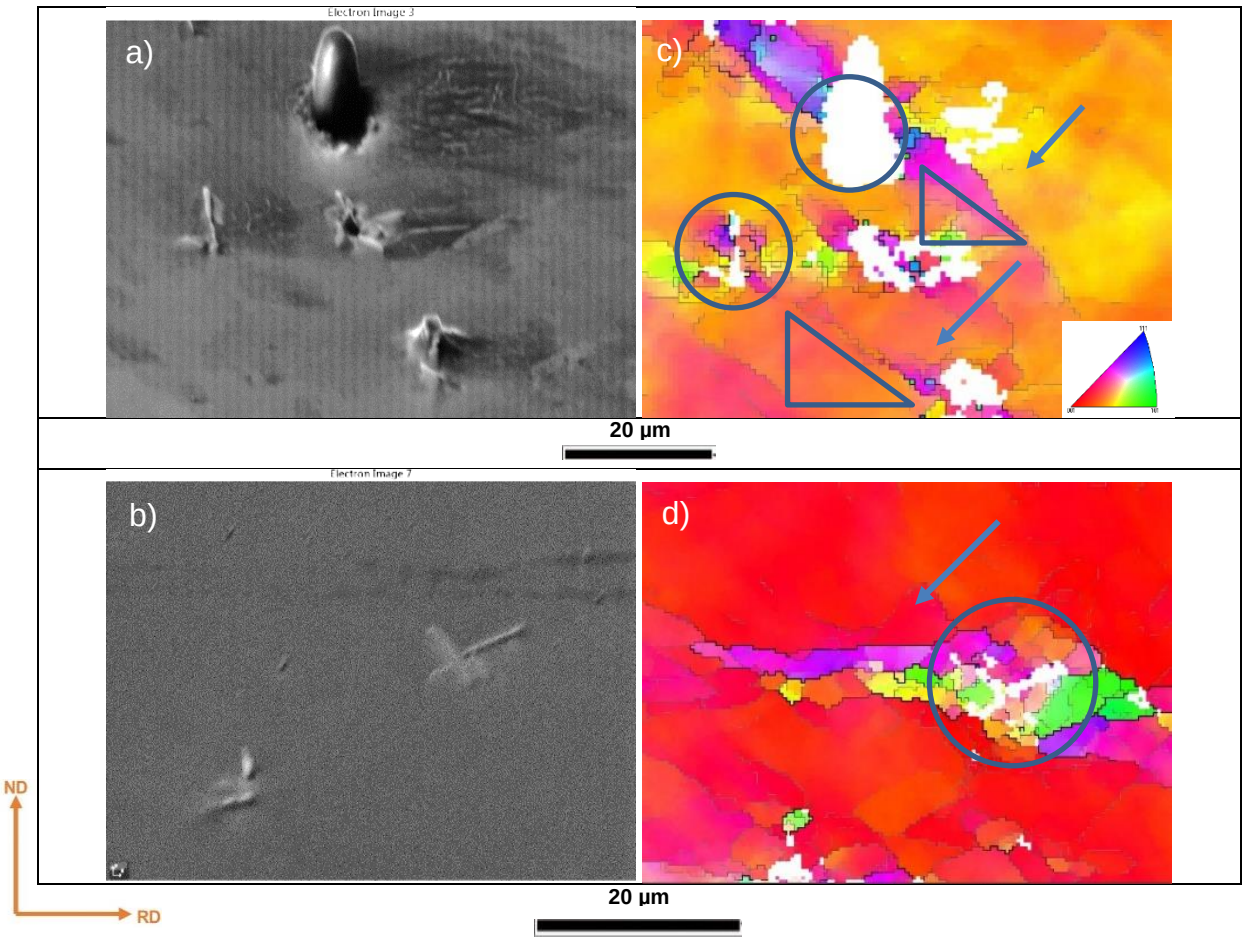

Figure 4-30:SEM micrographs of a) CR -15/s, and b) R2 -15/s with corresponding IPF maps of c) CR -15/s, and d) R2 -15/s showing PSN.

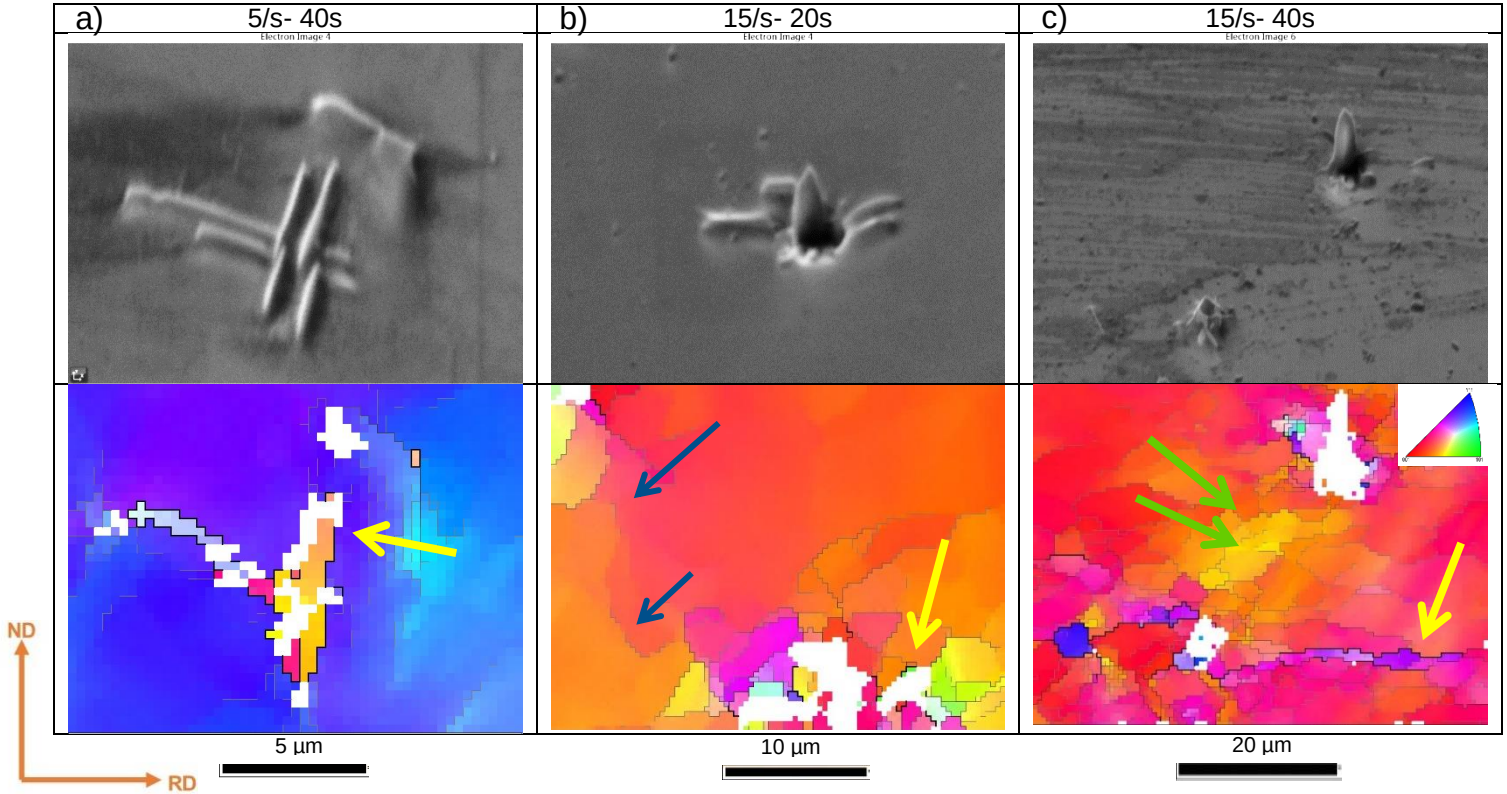

Figure 4-31: SEM images with corresponding IPF maps for various 4-pass schedules at high magnification. Scale bars are at a) 5 µm, b) 10 µm and c) 20 µm, respectively.

In Figure 4-32, the band contrast image overlaid with EDS maps show high concentrations in Nb reflecting areas where precipitates are present. The local misorientation intensity map shows the degree of misorientation emanating from the regions with precipitates, Figure 4-32. The recrystallisation fraction map (Figure 4-32c) shows the deformed structure in red when the average misorientation within the reconstructed grain is high and yellow when the average misorientation is slightly lower, whilst blue grains define grains where the average misorientation is low and are thus considered to be recrystallised grains. The processing is automated in Channel 5, Tango software. The texture map highlights that the structure is mostly affiliated with Cube orientations, shown by the significant presence of blue colour. Orientations that cannot be classified as any of the unique textures are presented as white. Figure 4-32 shows how the low angle grain boundaries, shown by grey lines in the recrystallisation fraction map formed sub-grain boundaries after being subjected to a strain rate of 15 /s and inter-pass time of 40 s. This is further evidence of how the subgrains grow from the regions around the precipitates present in the matrix.

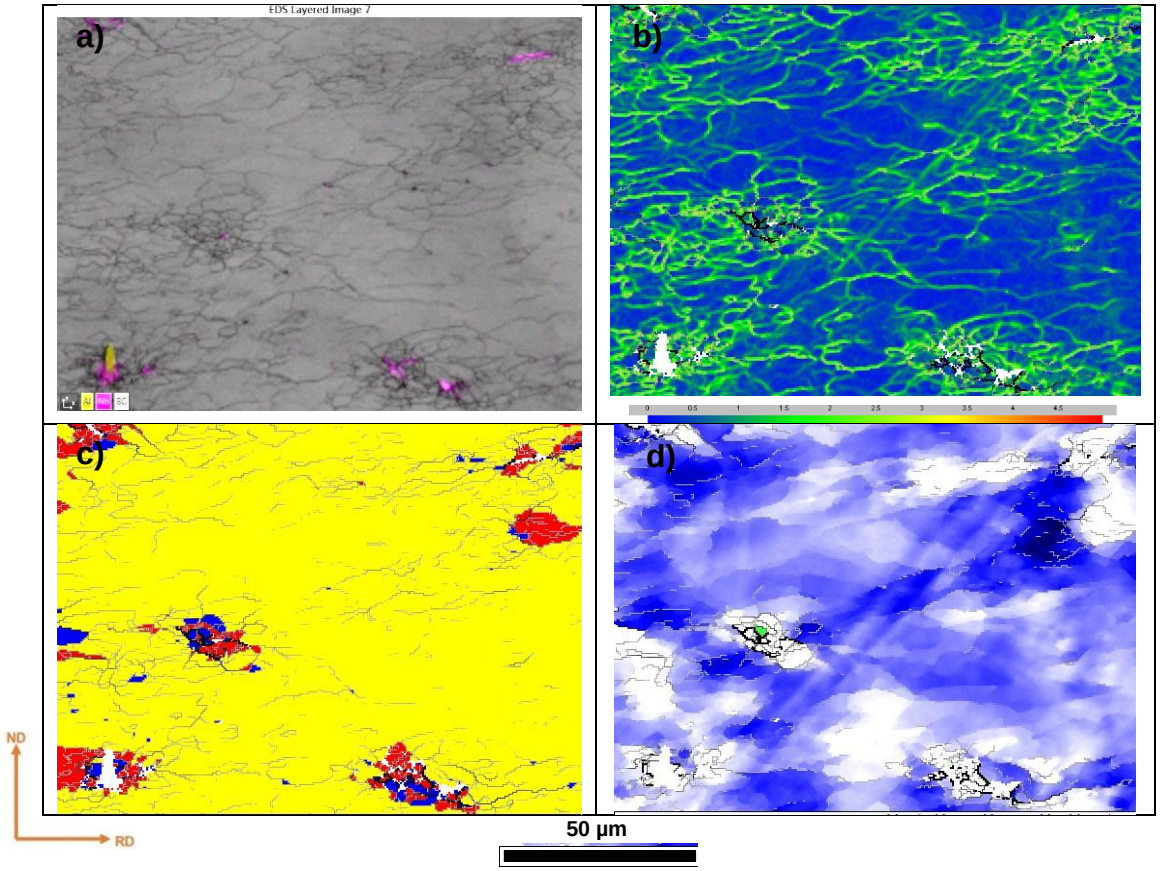

Figure 4-32: a) Nb and Al (aluminium) EDS maps overlapped on a band contrast image, b) local misorientation map, c) recrystallisation fraction map, and d) texture map showing the parent Cube texture in blue colour and S in green.

Figure 4-33 shows further analysis of CR in Figure 4-29, now focusing on the boundary around the Cube grain, red in the texture map correlated with lower Taylor values, Figure 4-33 c and d respectively. These low Taylor Factor (TF) grains are known to be hard to recrystalise during hot rolling and annealing [27]. However, there is a change of the Cube orientation, areas not coloured red, possibly due to the rotation of the sub-grains formed within the parent Cube texture grain. Notably, there was less volume fraction of precipitates in the Cube oriented grain compared to the neighbouring grain, that exhibited a high-volume fraction of recrystallised grains, some with relatively high TF. These high TF grains most likely recrystallised further in the subsequent deformation passes.

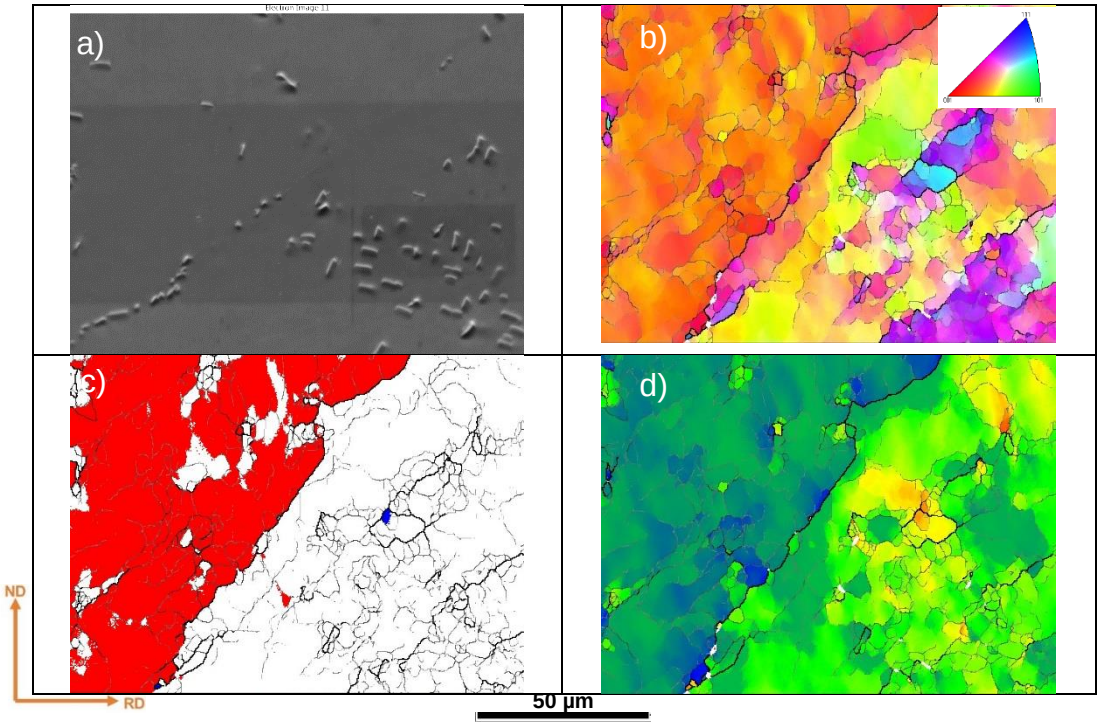

Figure 4-33: Further analysis of CR in Figure 4-29; clockwise a) SEM micrograph, b) IPF map; c) texture map and d) TF map.

4.4.5 Inclusions and precipitates in the as cast condition

Both the inclusions and precipitates were analysed using the SEM-EDS. In Figure 4-34a, star-like precipitates formed heterogeneously on an inclusion in the matrix, while the irregular-shaped precipitates (arrowed in blue) formed heterogeneously on grain boundaries as shown in Figure 4-34b. Based on previous works [86, 85, 90, 91, 92], these precipitates are known to either be NbC or Laves phases.

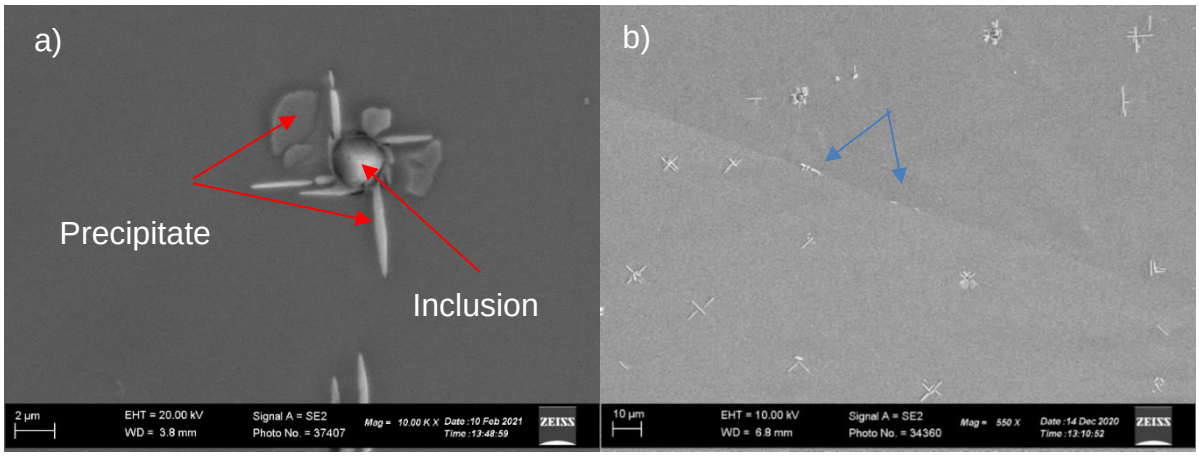

Figure 4-34: a) Magnified image of complex inclusion-precipitate particles, b) distribution of precipitates in grains.

The needle-like precipitates in the columnar region were found to be Laves phase, Figure 4-35, that formed during casting, as the cooling rate is slower within the slab interior [93]. The Laves phase was also predicted by ThermoCalc^{TM} simulations. This was confirmed by the EDS evaluations, which showed that these particles were rich in Fe, thus making them the form of $Fe_2(Nb, Cr)$.

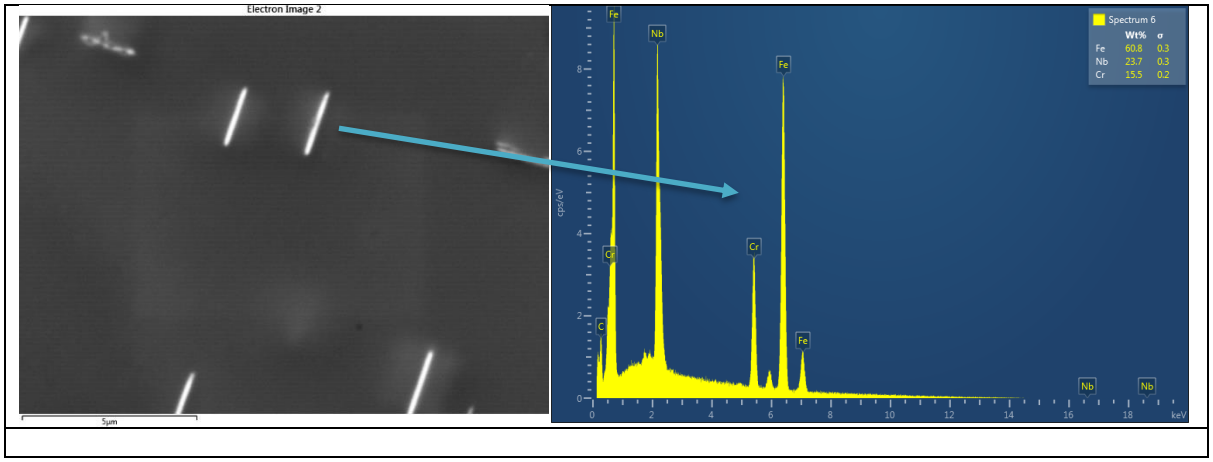

Figure 4-35: EDS analysis of the needle-like precipitates found in the columnar region of the cast slab correlating to Laves phase.

Figure 4-36a presents the morphology of the precipitates. The morphology varied with some being shaped irregularly (arrowed in purple), needle-like (arrowed in blue), plate-like (arrowed in orange) and star-like (arrowed in white) precipitates. The star and needle-like precipitates grew along preferred directions depending on the grain orientation. Precipitates seemed to form favourably in certain grains as opposed to other grains, as seen in Figure 4-36b.

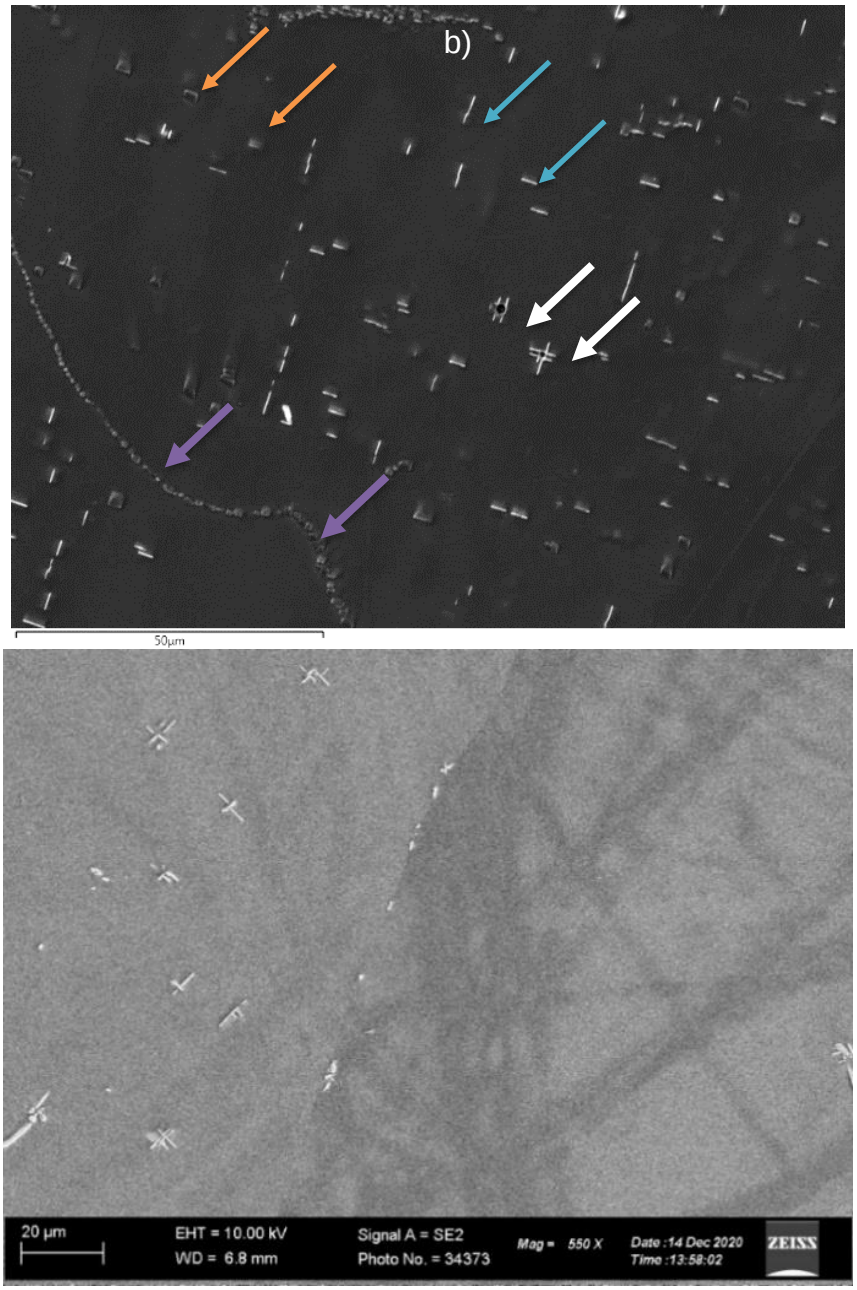

Figure 4-36: a) Precipitate morphologies in the as-cast structure; b) as cast columnar sample, showing the uneven precipitate distribution across grains.

While needle-like precipitates were the Laves phases, plate-like precipitates were found to be NbC. This analysis correlated with analysis of previous studies [93, 98, 99, 102] and ThermoCalc™ simulations, in terms of precipitate morphology and type. The precipitate and inclusions found in the continuously cast slab differed in the surface (chill-zone), columnar, and equiaxed regions. The precipitates in the chill zone were too fine to be detected by the SEM and, therefore, only the inclusions, which formed in the melt, were observed and contained Al, Si, Ca and O, as shown in Figure 4-37a.

As expected, due to slower cooling rates, the columnar and equiaxed regions showed coarse NbC and Laves phase, Figure 4-37b and c.

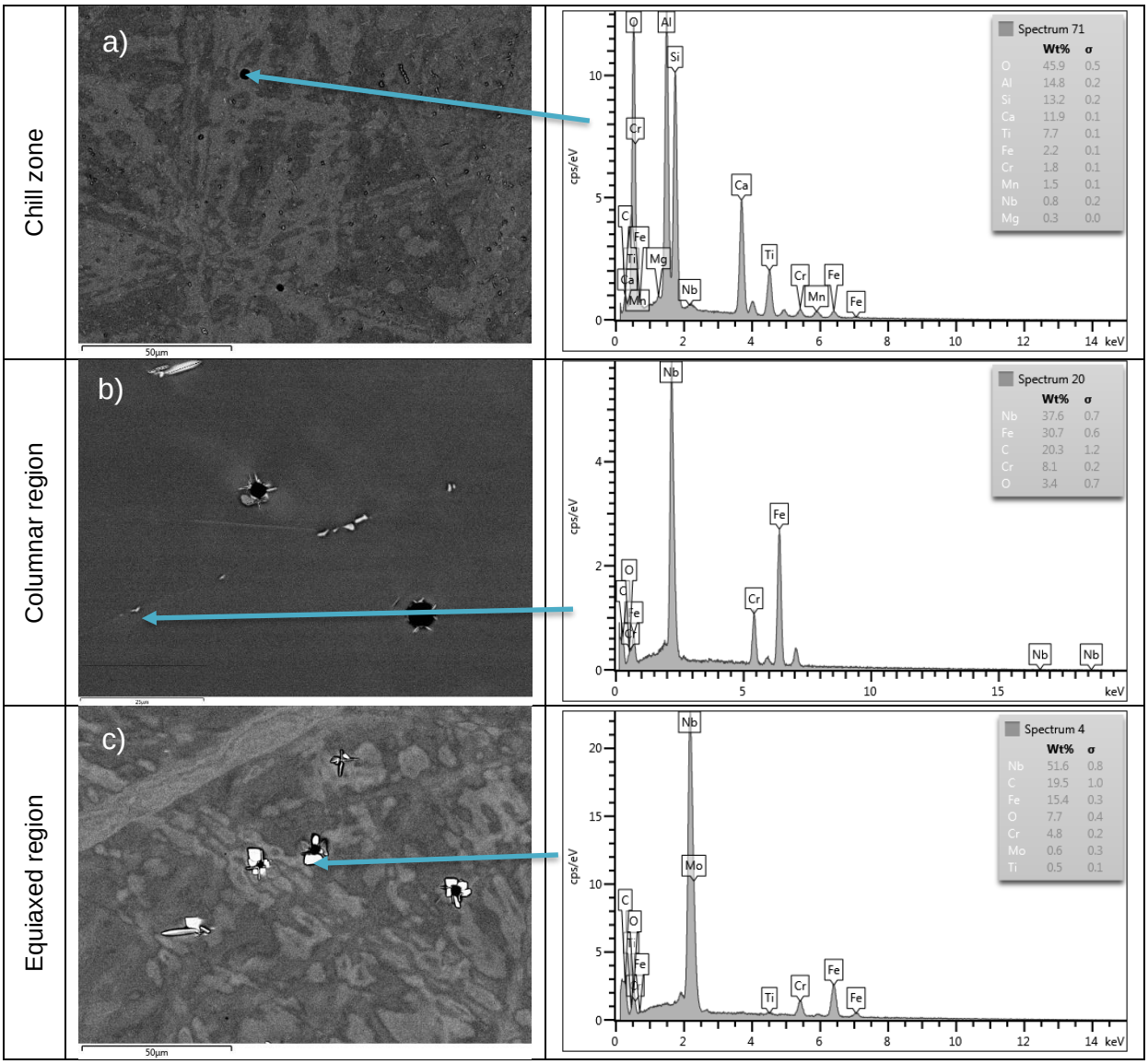

Figure 4-37: SEM images with corresponding EDS analyses of the particles in different regions of the cast slab.

Figure 4-38 shows the volume fraction of the inclusions and precipitates observable by SEM from the surface to the center of the slab. Unlike the interior of the slab, the chill zone is known to cool the fastest and, therefore time for the precipitation is limited and most particles are finer due to the higher driving force [92]. Hence the lower volume fraction of precipitates in the chill zone. Important to note is that precipitates were visible in the chill zone but they were just not large enough to be measured accurately. Therefore, it does not come as surprise that the chill zone grain size is the

finest and remains so after the slab cools to room temperature since fine precipitates are known to pin grain boundaries [88].

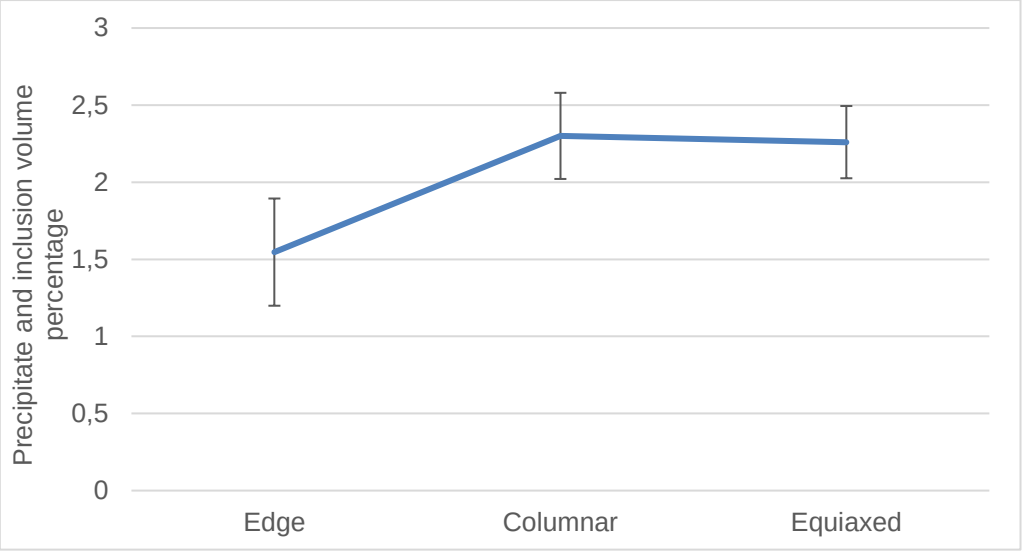

Figure 4-38: Volume fraction of precipitates, observable by SEM, from the from the surface to the slab centre.

4.4.6 Inclusions and precipitates after hot rolling simulations

Figure 4-39 to Figure 4-40 show the TEM micrographs of the R2 sample. Figure 4-39 shows two star-like precipitates, one nucleated heterogeneously around an inclusion and the other homogeneously in the matrix. It was found that significant sub-grain structure formed around these precipitates. The formation and organisation of the deformed structure into grain boundaries are arrowed in green in Figure 4-39 a, c, d and f. As may be seen, some of the PSN recrystallised grains were present (A) and others quite evidently did not show the formation of a complete grain (B), see Figure 4-39 a, c and f. This is evidence that the structure has partially recrystallised. The new grains formed when the accumulated strain around the precipitates reached the critical strain for the recrystallisation.

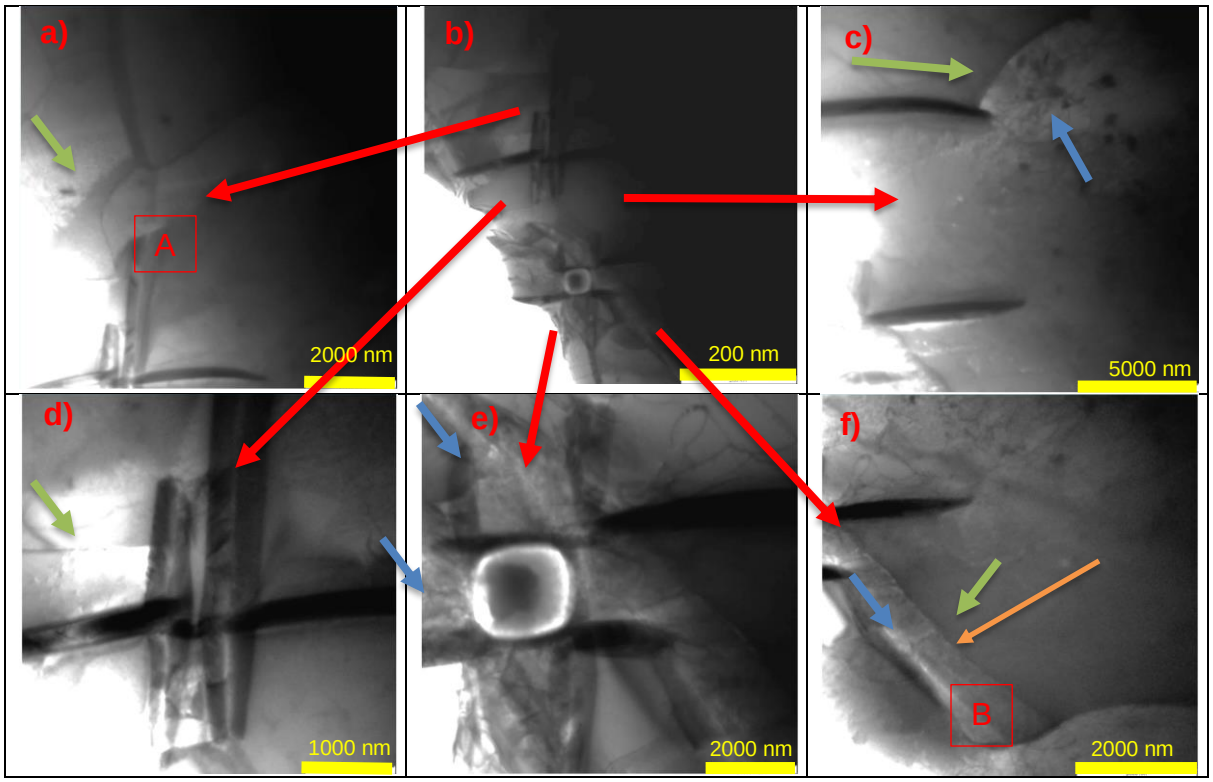

Figure 4-39: TEM images showing needle-like precipitates with sub-grain formation around precipitates. Scale bars are at a) 2000 nm, b) 200 nm, c) 5000 nm, d) 1000 nm, e) 2000 nm and f) 2000 nm.

Figure 4-40 shows the TEM micrographs of samples after 3-pass deformation at 5 /s, high strains and longer inter-pass times, sample R2.

Figure 4-40 shows the general structure of the deformed sample. Sub-grain boundaries are well-defined and arrowed in orange. The dislocation network is clearly shown to be present within the sub-grain. The sub-grain structure indicates that this is still highly deformed but has dislocations organising in subgrains, typical of the onset of recovery [22, 40, 63].

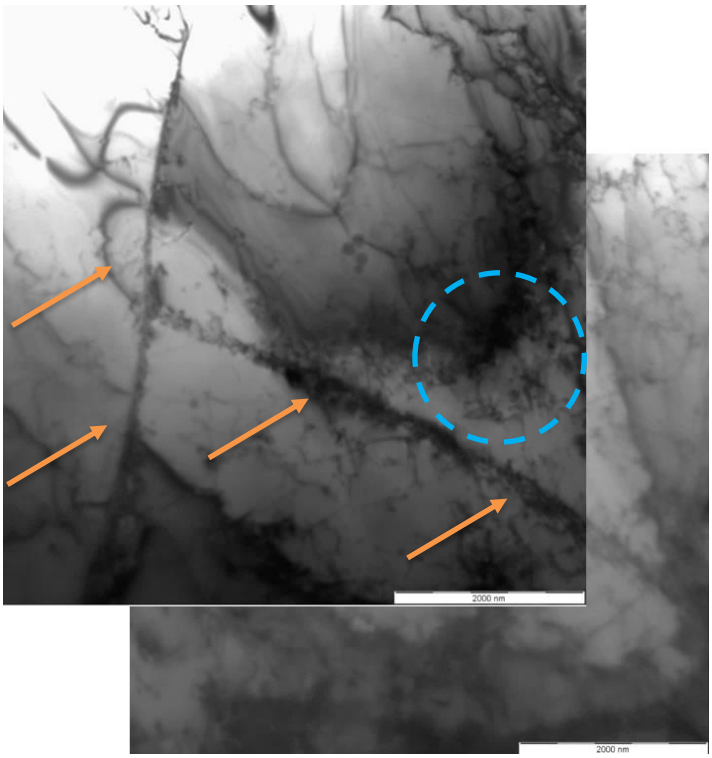

Figure 4-40: TEM image showing the sub-grain structure and precipitate distribution in the deformed sample. Orange arrows showing organisation of dislocation into subgrain boundaries, with disordered dislocation presence circled in blue.

Work by previous authors [94] showed that the interaction and density of dislocations around NbC precipitates were found to be more around precipitates (>200 nm) than in the rest of the matrix. Although the quantification of dislocation was not undertaken in this study, it is shown from TEM imaging that the larger precipitates showed PSN around the precipitates as opposed to smaller precipitates. Furthermore, de Siqueira [49] found that the precipitate size for PSN in FSSs to be about 1 µm, which is much smaller than what was observed in this work i.e., 5 nm. In other words, the TEM revealed the occurrence of DDRX around precipitates.

Chapter 5: Discussions

5 DISCUSSIONS

5.1 Introduction

The results are presented in an elaborate manner, which includes to some extent, some discussion. However, there are still a few points pertaining to the influence of the simulated roughing schedules on the evolution of the microstructures and texture during the simulated finishing process that require further discussion and are presented in this chapter. Recovery and recrystallisation are well documented processes [11, 17, 27, 32, 35, 63], particularly on FSS, where the need for improved drawability and the elimination of ridging is of significance. Retained strain occurs due to *inter alia*, inhomogeneous deformation leading to differing degrees of recovery and recrystallisation, increased strain rate, increased strain and lowered deformation temperature. Increasing strain, will create a higher driving force for restoration earlier in the process, limiting recrystallisation later. It is known by increasing inter-pass times, retained strain is reduced by some form of static restoration. Previous work [95] has shown that strain can be retained by increasing strain in initial passes and controlling inter-pass times. Recovery is known to be affected by strain, temperature, and nature of the material [either high or low stacking fault energy (SFE) material, and the presence of solute atoms or second phases [60], where although recovery reduces the driving force for recrystallisation, it also plays a role in 'nucleating' recrystallisation. It is of note that retaining strain aids in driving recrystallisation forward.

5.2 Role of retained strain on the softening process.

The primary focus of this study was to increase the strain in the material in the first passes of the simulated roughing rolling, thereby controlling the dynamic restoration. This was done by increasing the inter-pass time to allow for static recovery. The reason behind this was to increase the overall amount of the retained strain during the finishing rolling process i.e., by limiting the likelihood of reaching the critical strain per pass during roughing simulation [16, 19, 95]. The roughing simulations revealed that the CR and R1 schedules exhibited lower work hardening rate and highly strained structure, Figure 4-3. The increased strain in R2, coupled with the increased inter-pass time led to higher work hardening rate in pass three due to increased softening during

the interpass times in the preceding passes. As opposed to R1 and CR, Figure 4-3, one would argue that the R2 sample accumulated the least strain during roughing rolling simulation due to static recovery as a result of the increased interpass time.

After 6-passes, a clear sub-grain structure emerged in all materials (Figure 4-9). The work hardening rate in CF was lower than that of samples F1 and F2. As such, it can be deduced that the CF material underwent more restoration during deformation as opposed to F1 and F2. In other words, the extent of softening was measured by the difference in the hardness values before and after the annealing process, Table 4-1. Schedule R2 exhibited the least recrystallisation fraction after the 6-pass deformation. This implies that the material accumulated strain during finishing although the critical strain for recrystallisation was not reached due to recovery, Figure 4-10.

Overall, R2-F2 schedule retained the highest amount of strain after 6-passes. It was likely that the limited retained strain from roughing contributed to less recrystallization after 6-passes, as the accumulated strain was not sufficient to reach the critical strain for recrystallisation. The increased inter-pass time encouraged SRV, as with R1. However, recovery only imparts limited amounts of restoration as opposed to recrystallisation itself [20, 63, 104].

5.3 **Role of retained strain in texture development.**

The IPF maps in Figure 4-27 correlate with the observed evolution of hardness i.e., the control sample, CF, showed relatively more recrystallised grains compared to the rest after 3 and 6-pass rolling simulations. However, all simulation schedules in general, failed to break down the inherent Cube texture of the continuously cast slabs. The sub-grain structure was still prevalent even after 6-passes, Figure 4-27. Therefore, it can be deduced that although recrystallisation occurred to a limited extent, the restoration mechanism was largely dynamic and static recovery. Never the less, the control schedule showed improved breakdown of the cast structure compared to the other two experimental schedules.

In view of these findings, it can be deduced that the experimental R2-F2 simulations were not successful in retaining strain after roughing rolling to be used as extra driving force for the recrystallisation process during finishing rolling schedules. None of the

schedules reached the critical strain for recrystallisation following finishing. Therefore, the initial cast Cube texture was not randomised except for the formation of sub-grains with small misorientations relative to the parent grain. This is evident from the correlated misorientation angle distribution data, which is largely below 15°, typical of low angle grain boundaries, Figure 4-26. However, EBSD analysis showed that the inclusions and precipitates through PSN, was capable of randomising texture within the vicinity of the particles.

5.4 Particle stimulated nucleation and its influence in recrystallisation and texture of 436 ferritic stainless steel

Both 3 and 6-pass schedules showed evidence of PSN. PSN is known for texture randomisation through the nucleation of randomly oriented grains during hot deformation [18, 89]. Essentially, the recrystallisation mechanism associated with PSN is DDRX, where a high concentration of deformation around the precipitate provides enough driving force for nucleation and growth of new grains, Figure 4-29 to Figure 4-33. Observation at high magnification revealed that the DDRX was by HAGB migration through strain-induced boundary migration (SIBM), another particular trait of DDRX, which is not typical of high stacking fault energy materials [16],
Figure 4-29 d and e.

Overall, in the 3 and 6-pass tests, samples were mainly strain-hardened during the first three passes, Figure 4-8, with softening occurring from the fourth pass onward. The samples were primarily deformed, with recrystallisation occurring mainly through micro-shear band formation emanating from the precipitates. The EBSD analysis confirmed the development of clear sub-grain networks after 6-passes, Figure 4-27. The formation of sub-grains through recovery within a material is typical of the onset of CDRX. Recrystallisation was, however, only found around larger precipitates and was not found around finer precipitates. The presence of PSN resulted in randomisation of grain orientations, whereas the formation of sub-grain networks showed minimal variation in grain orientations.

In this work, the initial grains prior to hot working were large as cast columnar grains. The initiation of recrystallisation at grain boundaries through DDRX would therefore be limited. As a result, heterogeneities like shear bands within the material would form more readily and act as sites for nucleation of recrystallisation even during hot deformation [16]. Generally, this occurs at high strains and lower temperatures [89]. The shear bands produce new grain orientations within the parent grain through recrystallisation, which is imperative in breaking down the cast structure. In this work, it was observed that the shear bands seemed to emanate from areas with precipitates, Figure 4-30. These micro shear bands were observed at relatively higher deformation temperatures. This was attributed to the higher strain rate of 15 /s, typically not studied by other authors [19], as these are generally found at low deformation temperatures. At lower temperatures, particles restrict dislocation rearrangement, leading to stabilisation of the substructure, which in turn leads to the formation of micro shear bands.

5.5 Applicability of the results to typical plant hot strip rolling

In general, laboratory simulations are not an adequate representation of plant scale testing because of the associated limitations and as such, in this work the following limitations were encountered:

- The number of passes in the multi-pass rolling simulations were limited by the specimen size to avoid the barrelling effects on the 10 mm diameter and 15 mm long cylinders for the Gleeble 1500, and 5 mm diameter and 10 mm long cylinders for the Dilatometer 850D simulations. The three passes were applied to simulate roughing rolling with an additional three passes simulating finishing rolling. The typical industrial reverse roughing rolling and Steckel mill finishing rolling takes about 7-passes each with strains per pass ranging from 0.17 to 0.24 resulting in about 1.6 total strain.
- The strain rates in the plant can range from 4 to 20/s during roughing and from 20 to 100/s during finishing which is substantially higher than the laboratory strain rates of 5 and 15/s used in this work.

Considering these limitations and the fact that R2 schedule resulted in the least recrystallisation and most sub-structure in the laboratory simulations, it would be a worthwhile endeavour to attempt industrial scale simulations using the modified R2 schedule, i.e., six pass roughing rolling schedule followed by the normal Steckel mill finishing rolling process. This would confirm if the material could reach its critical strain for the initiation of CDRX or DRX leading to an improvement in the breakdown of the cast structure and its Cube texture, and randomisation of texture. Figure 5-1 shows the industrially produced hot band microstructures before and after annealing that the benchmark roughing schedule, CF, simulated. As may be seen, the hot band was partially recrystallised and the retained strain acted as a driving force for the static recrystallisation, which was not the case with laboratory simulations.

a)

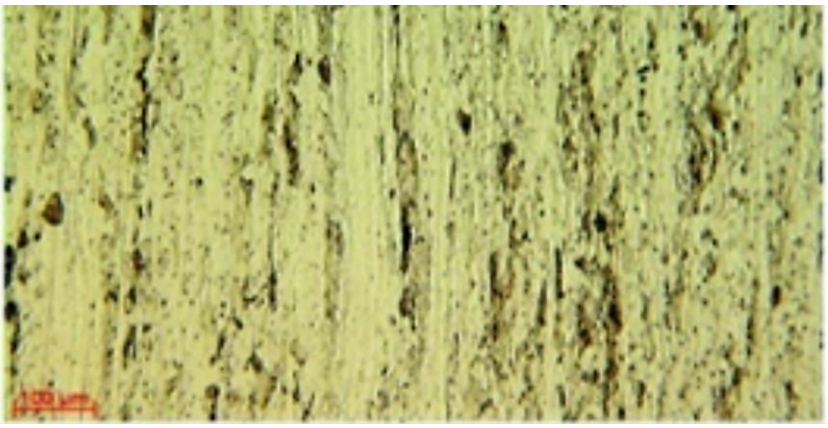

b)

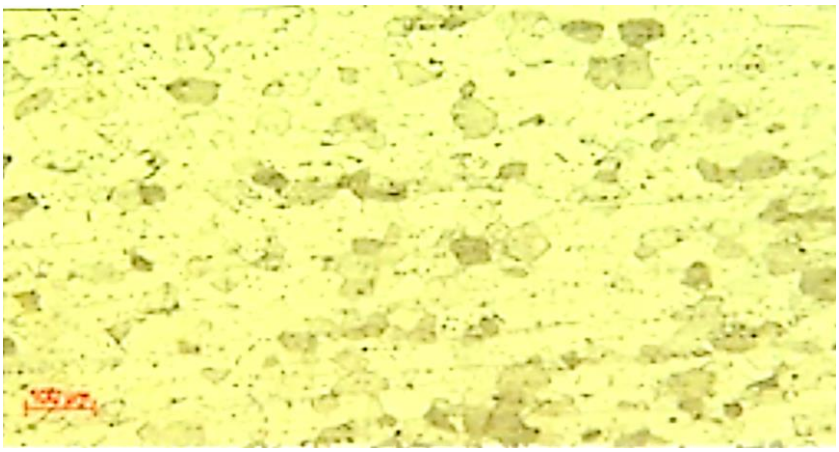

Figure 5-1: Microstructures of the studied steel, 436, industrially rolled hot band sample showing an unrecrystallised microstructure after hot rolling (a) and after hot band annealing (b) [15].

Overall, it can be concluded that increasing both the strain per pass and inter-pass time can potentially contribute to an increased driving force for recrystallisation needed

as opposed to recovery during the final stages of the hot rolling process of FSSs. However, this is yet to be confirmed at industrial level.

Chapter 6: Conclusions & Recommendations

6 CONCLUSIONS & RECOMMENDATIONS

6.1 Conclusions

The evolution of the microstructures and texture of AISI 436 ferritic stainless steel were investigated through simulated hot rolling with the aim of accumulating strain during the roughing rolling so that it could act as an extra driving force for recrystallisation in the finishing rolling process. The primary goal was to breakdown the cast columnar grains and the Cube texture for improved drawability and surface quality. However, this was partially achieved and the following conclusions can be made:

- The simulated roughing rolling schedule, R2, with increased total strain (from 0.68 to 0.8) and inter-pass times (from 43.3 to 60 s), exhibited less sub-grain refinement i.e., resulted in less retained strain than the other two schedules, CF and R1 after three passes. This resulted in CR and R1 schedules having increased driving force for recrystallisation during roughing but less energy for recrystallisation during finishing. The goal of accumulating strain during the simulated roughing rolling process to act as the driving for recrystallization during finishing rolling was not achieved, but this increased the potential for strain retention during finishing.
- However, the accumulated strain per pass in all simulations could not reach the critical strain for recrystallisation during the simulated finishing rolling process to aid the breaking down of the cast columnar grains with predominantly Cube oriented grains.
- The particle stimulated nucleation was present in all hot working schedules. As expected, the recrystallisation mechanism was by DDRX. This resulted in random grain orientations around the inclusions and precipitates. However, the recrystallised fraction was not adequate to significantly change the bulk of the cast structure and texture.
- Industrial trials are necessary to validate the hypothesis that limiting the restoration processes during the early stages of hot working i.e., during roughing rolling, can promote the recrystallisation process in the later stages of the finishing rolling process. This could not be done in this work due to the limitations imposed by the laboratory simulation process.

REFERENCES

[1] V. Pienaar, “Linkedin Feed,” 2020. [Online]. Available: https://www.linkedin.com/feed/update/urn:li:activity:6703628792184770560/. [Accessed 22 09 2020].

[2] Damstahl, “Brochure,” in *Technical Information*, Damstahl, Ed., Skanderborg, Damstahl, 2015, pp. 250-285.

[3] S. M. Kim, Y. S. Chun, S. Y. Won, Y. H. Kim and C. S. Lee, “Hydrogen Embrittlement Behavior of 430 and 445NF Ferritic Stainless Steel,” *Metallurgical and Materials Transactions A,* vol. 44, no. A, pp. 1331-1339, 2013.

[4] F. Gao, F. Yu, R. D. K. Misra, X. Zhang, S. Zhang and Z. Liu, “Microstructure, Texture, and Deep Drawability Under Two Different Cold-Rolling Processes on Ferritic Stainless Steel,” *Journal of Materials Engineering and Performance,* vol. 24, no. 10, pp. 3862-3880, 2015.

[5] K. H. Lo, C. She and J. K. L. Lai, “Recent developments in stainless steel,” *Materials Science and Engineering,* vol. 65, no. R, pp. 39-104, 2009.

[6] F. V. Braga, “Hot deformation behaviour of ferritic stainless steel stabilized with Nb during hot rolling simulation at different temperature ranges,” *Journal of Materials Research,* vol. 31, no. 5, pp. 635-645, 2016.

[7] J. Charles, J. Mithieux, P. Santacreu and L. Peguet, “The ferritic stainless family: The appropriate answer to nickel volatility?,” *Revue de Métallurgie,* pp. 703-720, 2009.

[8] K. A. Annan, “Effect of Hot Working Characteristics on the Texture Development in AISI 430 and 433 Ferritic Stainless Steel,” University of Pretoria, Department of Materials Science and Metallurgical Engineering, Pretoria, 2012.

[9] H. Uananisa, C. Siyasiya and W. S. a. M. J. Papo, “The Influence of Thermomechanical Processing on the Surface Quality of an AISI 436 Ferritic Stainless Steel,” *The Journal of The Southern African Institute of Mining and Metallurgy,* vol. 116, pp. 981-986, 2016.

[10] M. G. Maruma., “Effect of composition and thermomechanical processing on texture evolution, formability and ridging behaviour of ferritic stainless steel,” Department of Materials Science and Metallurgical Engineering, University of Pretoria, Pretoria, 2013.

[11] H. C. Chao, “Recent Studies into the Mechanism of Ridgin in Ferritic Stainless Steels,” *Metallurgical Transactions,* vol. 4, pp. 1973-1183, 1971.

[12] C. W. Sinclair, J. D. Mithieux, J. H. Schmitt and Y. Brechet, “Recrystallization of stabilized ferritic stainless steel sheet.,” *Metallurgical and Materials Transactions a-Physical Metallurgy and Materials Science,* vol. 36A, no. 11, p. 3205–3215, 2005.

[13] P. D. Wu, H. Jin, Y. Shi and D. J. Lloyd, “Analysis of ridging in ferritic stainless steel sheet,” *Materials Science and Engineering: A,* vol. 423, no. 1-2, pp. 300-305, 2006.

[14] H. Takechi, H. Kato, T. Sunami and T. Nakayama, “The Mechanism of Ridging Formation in 17% Chromium Stainless Steel Sheets,” *Transactions of Japan Institute of Metals,* vol. 8, pp. 233-239, 1967.

[15] A. J. Kruger, Influence of the cast structure on the evolution of the microstructures and texture during roughing mill rolling of Mo-added 436 ferritic stainless steel., Pretoria: Department of Materials Science and Metallurgical Engineering, University of Pretoria, 2020.

[16] K. Huang and R. E. Loge, “A review of dynamic recrystallization phenomena in metallic materials,” *Materials and Design,* vol. 111, p. 548–574, 2016.

[17] K. A. Annan, C. Siyasiya and W. Stumpf, “Characterization of the texture evolution in AISI 430 and AISI 433 ferritic stainless steels during simulated hot rolling,” *Materials Research Society Advances,* pp. 1985-2002, 2018.

[18] D. Raabe, “Recovery and recrystallisation: Phenomenon, Physics, Models, Simulations,” in *Physical Metallurgy*, Germany, Elsevier, 2014, pp. 2291-2396.

[19] T. Sakai, A. Belyakov, R. Kaibyshev and H. Miura, “Dynamic and post-dynamic recrystallization under hot, cold and severe plastic deformation,” *Progress in Materials Science* , vol. 60 , p. 130–207, 2014.

[20] S. Mehtonen, E. Palmiere, D. Misra, P. Karjalainen and D. Porter, “Microstructural and Texture Development during Multi-Pass Hot Deformation of a Stabilized High-Chromium Ferritic Stainless Steel,” *ISIJ International,* vol. 54, no. 6, pp. 1406-1415, 2014.

[21] X. Ma, J. Zhao, X. Z. W. Du, L. Jiang and Z. Jiang, “Quantification of texture-induced ridging in ferritic stainless steels 430 and 430LR during tensile deformation,” *Journal of Materials Research and Technology,* vol. 8, no. 2, pp. 2041-2051, 2019.

[22] G. Lefebvre, “Relationship Between Microstructure, Texture and Ridging in Ferritic Stainless Steels,” University of British Columbia, Materials Engineering, Vancouver, 2014.

[23] P. Modak, S. Patra, R. Mitra and D. Chakrabarti, “Effect of Starting As-cast Structure on the Microstructure–Texture Evolution During Subsequent Processing and Finally Ridging Behavior of Ferritic Stainless Steel,” *Metallurgical and Materials Transactions A,* vol. 49, no. A, pp. 2219-2234, 2018.

[24] H. Bhadeshia and R. Honeycombe, “Chapter 12 Stainless Steels,” in *Steels - Microstructure and Properties, 4ed*, Elsevier, 2017, pp. 259-287.

[25] Total Matria, “Total Materia,” 2013. [Online]. Available: https://www.totalmateria.com/page.aspx?ID=CheckArticle&site=kts&LN=EL&NM=104. [Accessed 12 2022].

[26] Ulbrich, “Ferritic Stainless Steels: A useful overview of Ferritic Stainless Steels,” 2022. [Online]. Available: https://www.ulbrich.com/blog/ferritic-stainless-steel-a-useful-overview-of-ferritic-steel-grades/. [Accessed 14 12 2022].

[27] C. Zhang, Z. Liu and G. Wang, “Effects of hot rolled shear bands on formability and surface ridging of an ultra-purified 21%Cr ferritic stainless steel,” *Journal of Materials Processing Technology,* vol. 211, pp. 1051-1059, 2011.

[28] Y. Liu, Y. Yang, H. Bi and L. Zuo, “The Hereditary Feature for Preferred Orientation in Ferritic Stainless Steel,” *Advanced Materials Research,* vol. 97, no. 101, pp. 897-900, 2010.

[29] Columbus Stainless Steel Pty Ltd, “Downloads/Technical Brochures,” 15 July 2020. [Online]. Available: https://www.columbus.co.za/.

[30] B. I. Voronenko, “Austenitic-Ferritic Stainless Steels: A State-of-the-Art Review,” *Metal Science and Heat Treatment,* vol. 39, no. 9-10, pp. 429-437, 1997.

[31] W. D. Callister and D. G. Rethwisch, Materials Science and Engineering, An Introduction, 7ed, Utah: John Wiley & Sons Incorporated, 2007.

[32] R. Abbaschian, L. Abbaschian and R. E. Reed-Hill, Physical Metallurgy Principles, 4 ed., Stamford: Cengage Learning, 2010.

[33] T. H. Courtney, Mechanical Behavior of Materials, 2 ed., illinois: Waveland Press Inc, 1990.

[34] R. F. Ivo, D. A. Rodrigues, J. C. Santos, F. N. C. Freitas, L. F. G. Herculano, H. F. G. d. Abreu and P. P. R. Filho, “Study and classification of the Crystallographic Orientation Distribution Function of a non-grain oriented electrical steel using computer vision system,” *Journal of Materials Research and Technology,* vol. 8, no. 1, pp. 1070-1083, 2019.

[35] O. Engler and V. Randle, Introduction to Texture Analysis. Macrotexture, Microtexture and Orientation Mapping, 2 ed., Florida: CRC Press, 2010.

[36] H. Brokmeier, “Neutron diffraction texture analysis,” *Physica B ,* Vols. 234-236, pp. 977-979, 1997.

[37] J. A. Szpunar, “Texture studies using neutron diffraction,” *Journal of Materials Science,* vol. 19, pp. 3467-3476, 1984.

[38] A. D. Rollett, “Texture Measurement and Analysis,” in *ASM Handbook, Volume 22B, Metals Process Simulation*, D. U. Semiatin and S. L. Furrer, Eds., ASM International, 2010, pp. 92-99.

[39] R. Schwarzer, “Texture Mapping by Scanning X-Ray Diffraction and Related Methods,” Amsterdam, 2005.

[40] C. W. Sinclair, J.-D. Mithieux and F. Chassagne, “Unpublished work,” Aperam research centre, 2002.

[41] T. Oliveira, M. Cunha and I. Gonçalves, “Improving the ridging in AISI 430 ferritic stainless steel stabilised with niobium,” Helsinki, 2008.

[42] R. N. Wright, “Anisotropic plastic flow in ferritic stainless steels and the "roping" phenomenon,” *Metallurgical Transactions,* vol. 3, no. 7, pp. 83-91, 1972.

[43] H. J.Shin, J. K. An, S. H. Park and D. N. Lee, ““The effect of texture on ridging of ferritic stainless steel,” *Acta Materialia,* vol. 51, no. 16, pp. 4693-4706, 2003.

[44] D. Raabe and K. Lücke, “Annealing textures of bcc metals,” *Scripta Metallurgy,* vol. 27, p. 1533, 1992.

[45] C. W. Sinclair, “Embedded grain rotation and roping of stainless steel,” *Metallurgical and Materials Transactions a-Physical Metallurgy and Materials Science ,* Vols. 38A,, no. 10 , p. 2435–2441, 2007.

[46] O. Engler, M. Y. Huh and C. N. Tomé, “Crystal-plasticity analysis of ridging in ferritic stainless steel,” *Metallurgical and Materials Transactions a-Physical Metallurgy and Materials Science,* vol. 36A, no. 11, pp. 3127-3139, 2005.

[47] F. J. Humphreys and M. Hatherly, “Chapter 11 - Grain Growth Following Recrystallization,” in *Recrystallization and Related Annealing Phenomena*, Elsevier, 2004, pp. 333-378.

[48] H.-J. Shin, S.-H. Hong and D. N. Lee, “Analysis of ridging in ferritic stainless steel and aluminum alloy sheets,” Switzerland, 2004.

[49] R. P. d. Siqueira, H. R. Z. Sandim and D. Raabe, “Particle Stimulated Nucleation in Coarse-Grained Ferritic Stainless Steel,” *Metallurgical and Materials Transactions A,* vol. 44, pp. 469-478, 2013.

[50] F. Gao, Z. Y. Liu and G. D. Wang, “Effect of the size and dispersion of precipitates formed in hot rolling on recrystalisation texture of FSS,” *Journal of Material Science,* vol. 48, pp. 2404-2415, 2013.

[51] X. Y. Wang, J. T. Li, A. G. Jiang, X. M. Wang, W. Z. Shao and L. Zhen, “Particle-stimulated nucleation and recrystallization texture initiated by coarsened Al2CuLi phase in Al-Cu-Li alloy,” *Journal of Materials Research and Technology,* vol. 10, pp. 643-650, 2021.

[52] S. Mehtonen, E. Palmiere, D. Misra, P. Karjalainen and D. Porter, “Microstructural and Texture Development during Multi-Pass Hot Deformation of a Stabilized High-Chromium Ferritic Stainless Steel,” *ISIJ International,* vol. 54, no. 6, pp. 1406-1415, 2014.

[53] S. Mehtonen, E.J.Palmiere, R.D.K.Misra, L.P.Karjalainen and D.A.Porter, “Dynamic restoration mechanisms in a Ti–Nb stabilized ferritic stainless steel during hot deformation,” *Materials Science & Engineering A,* vol. 601, p. 7–19, 2014.

[54] N. I. Vázquez-Fernández, M. Isakov and M. Hokka, “Strain Hardening and Adiabatic Heating of Stainless Steels After a Sudden Increase of Strain Rate,” *Journal of Dynamic Behavior of Materials ,* vol. 8, pp. 316-321, 2022.

[55] S. V. Mehtonen, L. P. Karjalainen and D. A. Porter, “Hot deformation behaviour and microstructure evolution of a stabilized high CR ferritic stainless steel,” *Materials Science & Engineering A,* vol. 571, pp. 1-12, 2013.

[56] C. Zener and J. H. Hollomon, “Effect of Strain Rate Upon Plastic Flow of Steel,” *Journal of Applied Physics ,* vol. 15, no. 22, pp. 22-32, 1944.

[57] G. Glover and C. M. Sellers, “Recovery and Recrystallization During High-Temperature Deformation of Alpha Iron,” *Metallurgical Transactions,* vol. 4, pp. 765-776, 1973.

[58] F. J. Humphreys and M. Hatherly, Recrystallisation and related annealing phenomenon, 2 ed., Oxord: Elsevier, 2004.

[59] F. Humphreys and M. Hatherly, “Chapter 13: Hot Deformation and Dynamic Recovery,” in *Recrystallization and Related Annealing Phenomena*, Elsevier, 2004, pp. 469-509.

[60] F. Humphreys and M. Hatherly, “Chapter 6 Recovery after Deformation,” in *Recrystallization and Related Annealing Phenomena*, Elsevier, 2004, pp. 169-213.

[61] F. V. Braga, D. P. Escobar, T. J. Á. Reis, N. J. L. d. Oliveira and M. S. Andrade, “Recrystallization of niobium stabilized ferritic stainless steel during hot rolling simulation by torsion tests,” *Journal of Materials Research and Technology,* vol. 5, no. 1, pp. 92-99, 2016.

[62] R. A. Petković, M. J. Luton and J. J. Jonas, “Recovery and recrystallization of carbon steel between intervals of hot working,” *The Canadian Journal of Metallurgy and Materials Science,* vol. 14, no. 2, pp. 137-145, 1975.

[63] J. Humphreys, G. S. Rohrer and A. Rollett, “Hot Deformation and Dynamic Restoration,” in *Recrystallization and Related Annealing Phenomena (Third Edition)*, Elsevier, 2017, pp. 469-508.

[64] J. Hamada, Y. Matsumoto, F. Fudanoki and S. Maeda, “Effect of Initial Solidified Structure on Ridging Phenomenon and Texture in Type 430 Ferritic Stainless Steel Sheets,” *ISIJ International,,* vol. 43, no. 12, p. 1989–1998, 2003.

[65] H. Takeuchi, H. Mori, Y. Ikehara, T. Komano and T. Yanai, “The Effects of Electromagnetic Stirring on Cast Structure of Continuously Cast SUS 430 Stainless Steel Slabs,” *ISIJ (Tetsu-to-Hagane),* vol. 66, p. 638, 1980.

[66] Y. Itoh, T. Okajima, H. Maede and K. Tashiro, “Refining of Solidification Structures of Continuously Cast Type 430 Stainless Steel Slabs by Electromagnetic Stirring,” *ISIJ Tetsu-to-Hagané,* vol. 67, p. 946, 1981.

[67] Y. Itoh, S. Takao, T. Okajima and K. Tashiro, “Effects of Alloying Elements and Inoculators on Refining of Solidification Structures of Type 430 Stainless Steel,” *ISIJ Tetsu-to-Hagané,* vol. 66, p. 710, 1980.

[68] J. Jiang, T. B. Britton and A. J. Wilkinson, “The orientation and strain dependence of dislocation structure evolution in monotonically deformed polycrystalline copper,” *International Journal of Plasticity,* vol. 69, p. 102–117, 2015.

[69] S. K. Thakur, A. K. Das and B. K. Jha, “Effect of Warm Rolling Process Parameters on Microstructure and Mechanical Properties of Structural Steels,” *Transactions of the Indian Institute of Metals,* vol. 75, p. 1509–1524, 2022.

[70] D. Q. Bai, Effect of rolling parameters on the no-recrystallisation temperature (Tnr) in Nb-bearing steels, Montreal: Department of Mining and Metallurgical Engineering-McGill University , 1993.

[71] J. J. Jonas, “Effect of Quench and Interpass Time on Dynamic and Static Softening during Hot Rolling,” *Steel Research Int,* vol. 76, no. 5, pp. 392-398, 2005.

[72] F. Gao, Z. Liu, H. Liu and G. Wang, “Texture evolution and formability under different hot rolling conditions in ultra-purified 17%Cr ferritic stainless steel,” *Materials Characterization,* vol. 75, pp. 93-100, 2012.

[73] M. Jonsson, TM-Rolling of Heavy Plate and Roll Wear, Lulea: Division of Material Mechanics Department of Applied Physics and Mechanical Engineering, 2006.

[74] J. Hollandt, J. Hartmann, O. Struß and R. Gärtner, “Chapter 1 - Industrial Applications of Radiation Thermometry,” in *Experimental Methods in the Physical Sciences*, Berlin, Elsevier, 2010, pp. 1-56.

[75] B. Roebuck, J. Lord, M. Brooks, M. Loveday, C. Sellars and R. Evans, “Measurement of flow stress in hot axisymmetric compression tests,” *Materials at High Temperatures,* vol. 23, no. 2, p. 59–83, 2006.

[76] J. V. Rensburg, Development and implementation of state variables based user materials in computational plasticity -PhD Thesis, University of Pretoria: Department of Mechanical and Aeronautical Engineering, 2016.

[77] G. E. Dieter, H. A. Kuhn and S. L. Samiatin, Handbook of workability and process design, Knovel, 2003.

[78] Y. C. Lin, M. Chen and J. Zhong, “Numerical simulation for stress/strain distribution and microstructural evolution in 42CrMo steel during hot upsetting process,” *Computational Materials Science,* vol. 43, pp. 1117-1122, 2008.

[79] ASTM International, “Designation: E112 − 13: Standard Test Methods for Determining Average Grain Size,” ASTM International, West Conshohocken, 2014.

[80] J. I. Goldstein, D. E. Newbury, P. Echlin, D. C. Joy, A. D. Romig, J. C. E. Lyman, C. Fiori and E. Lifshin, Scanning Electron Microscopy and X-ray Microanalysis, New York : Plenum Press, 1992.

[81] S. O. K. Kanaya, *Journal of Physics D: Applied Physics,* vol. 5, p. 43, 1972.

[82] S. K. Langer J, “Kinetics of nucleation in near-critical fluids,” *Physics Review A ,* vol. 21, no. 3, p. 948, 1980 .

[83] W. R. Kampmann R, “Kinetics of precipitation in metastable binary alloys: theory and application to copper–1. 9 at.% titanium and nickel–14 at.% aluminium (alloys).,” *Decompos Alloys Early Stages,* p. 91–103, 1983.

[84] S. Kodukula, H. Kokkomäki, E. Puukko, D. Porter and J. Kömi, “Influence of Hot Rolling Finishing Temperature on Texture and Ridging Resistance in Stabilized Ferritic Stainless Steel,” *Steel Research International,* vol. 92, pp. 1-11, 2021.

[85] E. Bemont, E. Cadel, P. Maugis and D. Blavette, “Precipitation of niobium carbides in Fe–C–Nb steel,” *Surface and Interface Analysis,* vol. 36, p. 585–588, 2003.

[86] M. P. Sello, “The Laves Phase embrittlement of Ferritic Stainless Steel Type 441,” Department of Materials Science and Metallurgical Engineering, University of Pretoria, Pretoria, 2009.

[87] H. J. Uananisa and C. W. Siyasiya, “The effect of hot deformation on the morphology and carbide distribution in a 436 ferritic stainless steel (FSS).,” *Acadamic Journal Education Research ,* vol. 10, no. 2, pp. 039-044, 2022.

[88] N. Meyer, Y. Bréchet, M. Véron, O. Geoffroy, M. Mantel and P. Dubois, “Microstructural development of 17% chromium ferritic stainless steels for electromagnetic actuation: Experiments nad modelling,” *Proceedings of the 6th Stainless Steel Science and Market Conference, ,* no. Part 17: Ferritics, pp. 751-756, 2008.

[89] M. Y. Salojee, C. W. Siyasiya, K. A. Annan and J. Moema, “Electron backscatter diffraction postprocessing techniques for studying recrystallisation phenomenon of Ferritic Stainless Steel,” Somerset West, 2022.

[90] T. Juuti, T. Manninen, L. Karjalainen and D. Porter, “The Effect of Niobium Carbides and Laves Phase on the Yielding Behaviour of a Stabilised Ferritic Stainless Steel,” Oulu, 2013.

[91] T. Juuti, L. Rovatti, A. Mäkelä, L. P. Karjalainen and D. Porter, “Influence of long heat treatments on the laves phase nucleation in a type 444 ferritic stainless steel,” *Journal of Alloys and Compounds,* vol. 616, p. 250–256, 2014.

[92] C. E. Muller, Precipitation during continuous casting, Berlin: Technischen Universit¨at Berlin, 2015.

[93] M. Labonne, A. Graux, S. Cazottes, F. Danoix, F. Cuvilly, F. Chassagne, M. Perez and V. Massardier, “Precipitation Kinetics in a Nb-stabilized Ferritic Stainless Steel,” *Metallurgical and Materials Transactions A ,* vol. 48A, p. 3655, 2017.

[94] A. Kostryzhev, P. Mannan and O. Marenych, “High temperature dislocation structure and NbC precipitation in three Ni-Fe-Nb-C model alloys,” *Journal of Materials Science,* vol. 50, no. 21, pp. 7115-7125, 2015.

[95] M. Candic, B. Tian, S. Kleber, M. Wießner, M. Kamaya and C. Sommitsch, “Investigation of retained strains and microstructures for a hot deformed stainless steel,” *Materials Science Forum,* Vols. 5571-572, pp. 169-174, 2008.

[96] ASTM International, “E407 − 07: Standard Practice for Microetching Metals and Alloys,” ASTM International, West Conshohocken, 2015.

[97] ASTM International, “Designation: E930 − 18: Standard Test Methods for Estimating the Largest Grain Observed in a Metallographic Section (ALA Grain Size),” ASTM International, West Conshohocken, 2019.

[98] ASTM International, “Designation: E1382 − 97 (Reapproved 2015): Standard Test Methods for Determining Average Grain Size Using Semiautomatic and Automatic Image Analysis,” ASTM International, West Conshohocken, 2015.

[99] ASTM International, “Designation: E517 − 19: Standard Test Method for Plastic Strain Ratio r for Sheet Metal,” ASTM International, West Conshohocken, 2019.

[100] J. Han, H. Li, Z. Zhu, L. Jiang, H. Xu and L. Ma, “Effects of processing optimisation on microstructure, texture, grain boundary and mechanical properties of Fe–17Cr ferritic

stainless steel thick plates," *Materials Science & Engineering A,* vol. 616, pp. 20-28, 2014.

[101] H. Yan, H. Bi, X. Li and Z. Xu, "Effect of two-step cold rolling and annealing on texture, grain boundary character distribution and r-value of Nb + Ti stabilized ferritic stainless steel," *Journal of Material Characterisation,* vol. 60, pp. 65-68, 2009.

[102] I. Jung, J. Mola, D. Chae and B. D. Cooman, "Influence of the cold rolling and annealing sequence on the ridging behaviour of Ti-stabilized 18% Cr ferritic stainless steel," *Journal of International Steel Research,* vol. 81, pp. 1089-1096, 2010.

[103] H. Liu, "Study of microstructure, texture and formability of Cr17 ferritic stainless steel: Ph. D. Thesis," Northeastern University, 2009.

[104] ASTM International, A240: Standard Specification for Chromium and Chromium-Nickel Stainless Steel Plate, Sheet, and Strip for Pressure Vessels and General Applications, West Conshohocken: ASTM International, 2019.

[105] M. Suehiro, "An analysis of the solute drag effect of Nb on the recrystallisation of ultra low carbon steel," *ISIJ International,* vol. 38, no. 6, pp. 547-552, 1998.

[106] B. Dutta, E. J. Palmiere and C. M. Sellars, "Modelling the kinetics of strain induced precipitation in Nb microalloyed steels," *Acta Materialia,* vol. 49, no. 5, pp. 785-794, 2001.

[107] T. Juuti, L. Rovatti, D. Porter, G. Angella and J. Kömi, "Factors controlling ambient and high temperature yield strength of ferritic stainless steel susceptible to intermetallic phase formation," *Materials Science & Engineering A,* vol. 726 , p. 45–55, 2018.

[108] A. Shekhtar, "Effect of aging and deformation on the microstructure and properties of Fe-Ni-Ti maraging steel," *Journal of Metal and Materials Transactions A,* vol. 35, no. A, pp. 973-983, 2004.

[109] A. Chbihi, X. Sauvage and D. Blavette, “Influence of plastic deformation on the precipitation of Cr in copper,” *Journal of material science,* vol. 49, pp. 6240-6247, 2014.

[110] F. J. Humphreys, “Reconstruction of grains and subgrains from electron backscatter diffraction maps,” *Journal of Microscopy,* vol. 213, no. 3 , p. 247–256, 2004.

[111] X. Ma, C. Miao, B. Langelier and S. Subramanian, “Suppression of strain-induced precipitation of NbC by epitaxial growth of NbC on pre-existing TiN in Nb-Ti microalloyed steel,” *Materials and Design,* vol. 132, p. 244–249, 2017.

[112] H. Lu, H. Guo, W. Liang, J. Li, G. Zhang and T. Li, “High-temperature Laves precipitation and its effects on recrystallisation behaviour and Lüders deformation in super ferritic stainless steel,” *Materials and Design ,* vol. 188, pp. 1-12, 2020.

[113] M. Salojee, K. A. Annan, C. W. Siyasiya and J. Moema, “Effect of hot rolling parameters on recovery mechanism in 436 (17%Cr, Nb-Mo) ferritic stainless steel,” *January 2022Suid-Afrikaanse Tydskrif vir Natuurwetenskap en Tegnologie ,* vol. 40, no. 1, pp. 1-7, 2022.

[114] T. B. Hilditch, T. d. Souza and P. D. Hodgson, “2 - Properties and automotive applications of advanced high-strength steels (AHSS),” in *Welding and Joining of Advanced High Strength Steels (AHSS)*, Woodhead Publishing, 2015, pp. 9-28.

[115] ASM Technical Books, “Chapter 6: Corrosion of Martensitic Stainless Steel Weldments,” in *Corrosion of Weldments*, J. R. Davis, Ed., ASM International, 2006.

[116] P. Cui, G. Xing, Z. Nong, L. Chen, Z. Lai, Y. Liu and J. Zhu, “Recent Advances on Composition-Microstructure-Properties Relationships of Precipitation Hardening Stainless Steel,” *Materials,* vol. 15, no. 23, p. 8443, 2022.

[117] J. H. Kim, M. G. Lee, J. H. Kang and C. S. O. F. Barlat, “Crystal plasticity finite element analysis of ferritic stainless steel for sheet formability prediction,” *International Journal of Plasticity,* vol. 93, pp. 26-45, 2017.

[118] R. W. Hertberg, Deformation and Fracture Mechanics of Engineering Materials, 3 ed., New York: John Wiley and Sons, 1989.

[119] D. R. N. Maubane, The Influence Of Rough Rolling Conditions On Austenite Evolution In Peritectic Microalloyed Plate Steels, University of Pretoria: Department of Materials Science and Metallurgical Engineering, 2018.

[120] B. Brockhouse, “The initial magnetization of nickel under tension,” *Canadian Journal of Physics,* vol. 31, p. 339, 1953.

[121] I. Samajdar, B. Verlinden, P. V. Houtte and D. Vanderschueren, “Recrystallisation kinetics in IF-steel: A study on the sluggish recrystallisation behaviour,” *Scripta Materialia ,* vol. 37, no. 6, p. 869–874., 1997.

[122] D. Raabe and K. Lücke, “Textures of Ferritic Stainless-Steel,” *Materials Science and Technology ,* vol. 9, no. 4, p. 302–312., 1993.

[123] D. Raabe and K. Lücke, “Texture and Microstructure of Hot Rolled Steel,” *Scripta Metallurgica Et Materialia ,* vol. 26, no. 8 , p. 1221–1226, 1992.

[124] M. F. Littmann, “Development of Improved Cube-on-Edge Texture from Strand Cast 3pct Silicon-Iron,” *Metallurgical Transactions A ,* vol. 6, no. 5 , p. 1041–1048, 1975.

[125] L. N. Pussegoda, S. Yue and J. J. Jonas, “Laboratory simulation of seamless tube piercing and rolling using dynamic recrystallization schedules,” *Metallurgical Transactions A ,* vol. 21A, p. 153–64, 1990.

[126] P. D. Hodgson, J. J. Jonas and S. Yue, “Growth during and after the static and metadynamic recrystallization of austenite.,” *Material Science Forum ,* vol. 715, no. 22, p. 94–96 , 1992.

[127] K. A. Annan, “The study of austenite grain growth in Nb-Ti-V microalloyed steels after reheating, during and after rough hot rolling,” Deppartment of Material Science and Metallurgical Engineering, University of Pretoria, Pretoria, 2015.

[128] D. Raabe, “Crystallographic Textures of Steels,” [Online]. Available: https://www.dierk-raabe.com/textures-of-steels/. [Accessed 17 August 2023].

[129] F. Boratto, S. Yue, J. J. Jonas and T. H. Lawrence, “Design of Schedules for the production of high strength microalloyed steel strip in a hot Steckel Mill,” Tokyo, 1988.

[130] S. Roy, S. Patra, S. Neogy, A. Laik, S. K. Choudhary and D. Chakrabarti, “Prediction of Inhomogeneous Distribution of Microalloy Precipitates in Continuous-Cast High-Strength, Low-Alloy Steel Slab,” *Metallurgical and Materials Transactions A,* vol. 43, no. A, pp. 1845-1860, 2012.

[131] C. M. Sellars, “Recrystallization of metals during hot deformation,” *Philosophical Transactions of the Royal Society of London,* vol. 288, pp. 147-158, 1978.

[132] M. Loveday, G. Mahon, B. Roebuck, A. Lacey, E. Palmiere, C. Sellars and M. R. v. d. Winden, “Measurement of flow stress in hot plane strain compression tests,” *Materials at High Temperatures,* vol. 23, no. 2, pp. 85-118, 2006.

[133] R. K. Viswanadham and C. A. Wert, “Electron microscopic study of precipitation in the system niobium-carbon,” *Journal of the Less Common Metals,* vol. 48, no. 1, pp. 135-150, 1976.

A SUPPLEMENTARY INFORMATION

Mill Log data was provided from Columbus Stainless Steel for Roughing (Table 6-2) and Steckel Mill (Table 6-3) rolling of 436 FSS.

The initial part of the study looked at mimicking roughing simulations obtained in the previous research, followed by the effect of finishing rolling on those simulations. Process data in the prior study (Table 6-1) shows three simulations. The first is the control replicating plant conditions, the second varies strain and strain rate, whilst the last simulation looks at the influence of inter-pass time alone.

Table 6-1: Previous master's study into rough rolling of 436 stainless steel.

Regime	A1								A1,1								A1,2						
Pass	P1	P2	P3	P4	P5	P6	P7		P1	P2	P3	P4	P5	P6	P7		P1	P2	P3	P4	P5	P6	P7
Thermomechanical Hits	Hit1	Hit2	Hit3	Hit4	Hit5	Hit6	Hit7		Hit1	Hit2	Hit3	Hit4	Hit5	Hit6	Hit7		Hit1	Hit2	Hit3	Hit4	Hit5	Hit6	Hit7
Preheat T (°C)	1080								1080								1080						
Start T (°C)	1010	990	975	960	950	935	930		1010	990	975	965	948	935	930		1010	990	975	960	950	935	930
End T (°C)	1000	980	970	952	938	931	925		1000	980	970	955	938	925	925		1000	980	970	952	938	931	925
Strain rate(1/s) [Mill logs]	4.83	7.24	9.80	12.50	15.00	17.40	23.00		4.83	5.50	10.00	11.50	19.00	22.30	21.70		4.83	7.24	9.80	12.50	15.00	17.40	23.00
Strain	0.18	0.34	0.23	0.24	0.24	0.24	0.30		0.18	0.22	0.24	0.27	0.29	0.30	0.29		0.18	0.34	0.23	0.24	0.24	0.24	0.30
Specimen tickness (mm) H_0=11.6mm	9.90	7.40	6.10	4.90	4.00	3.20	2.50		9.90	8.20	6.70	5.30	4.10	3.20	2.50		9.90	7.40	6.10	4.90	4.00	3.20	2.50
Interpass Time(s)	11	12.2	11.1	14	14.3	17.2	18.3		11	12.2	11.1	14	14.3	16.7	18.3		15.4	16.7	17.5	14	14.3	17.2	18.3

Table 6-2: Mill log data for rough rolling

PASS NO	LENGTH (m)	MAX ROLL TORQUE	MAX ROLL FORCE	AVG ROLL SPEED (m/s)	MAX ROLL SPEED (m/s)	MAX TEMP (°C)	AVG ENTRY GAUGE (mm)	AVG EXIT GAUGE (mm)	REDUCTION (%)	STRAIN RATE (/s)	Z (10^{17} /s)	Ln (Z)	ROLL TIME (S)	REVERSE TIME (S)
1	13.44	2050.279	11537.05	2.477	2.514	928.50	200	166.45	16.77	4.45	1.35	91.814	5.16	10.38
2	20.19	4031.749	19199.91	2.506	2.594	935.23	166.45	109.51	34.22	6.97	14.2	59.762	7.24	9.56
3	26.75	2650.197	14769.64	3.349	3.608	962.27	109.51	82.70	24.48	9.87	8.48	52.266	7.29	8.27
4	34.81	1931.019	14392.07	3.732	4.041	971.68	82.70	62.04	24.96	12.82	10.9	41.520	8.77	9.32
5	45.69	1826.894	14571.57	3.814	4.003	966.98	62.04	46.44	25.14	15.23	13.6	45.378	10.99	8.77
6	59	1397.633	14368.69	3.835	4.042	973.35	46.44	34.89	24.86	17.64	15.5	41.872	14.48	8.93
7	78.06	1434.268	16883.24	3.910	4.011	947.16	34.89	24.77	29.00	22.42	44.1	42.914	18.49	0

Table 6-3: Mill log data for finishing rolling on Steckel mill

PASS NO	LENGTH (m)	MAX ROLL TORQUE	MAX ROLL FORCE	AVG ROLL SPEED (m/s)	MAX ROLL SPEED (m/s)	MAX TEMP (°C)	AVG ENTRY GAUGE (mm)	AVG EXIT GAUGE (mm)	REDUCTION (%)	STRAIN RATE (/s)	Z (10^{17} /s)	Ln (Z)	ROLL TIME (S)	REVERSE TIME (S)
1	98.31	953.618	15235.5	3.214	927.06	911.11	29.77	22.67	23.83	21.31	9.25	43.7	33.5	6.10
2	132	1043.39	16912.6	5.096	926.07	921.11	22.60	17.067	24.47	39.36	22.6	44.6	31.2	4.39
3	176.69	913.017	17959.7	6.211	929.78	922.33	16.96	12.83	24.34	55.30	23.2	44.6	35.5	5.79
4	235.44	830.948	20009.7	7.053	926.23	921.91	12.73	9.63	24.33	72.52	45.4	45.3	41.3	4.34
5	315.38	866.63	22766.9	7.817	926.99	923.52	9.53	7.24	24.04	92.34	50.1	45.4	48.6	5.83
6	402.19	654.125	23563.7	8.417	920.06	910.52	7.15	5.66	20.80	106.87	111	46.2	56.5	7.47
7	501.56	603.794	23429.3	4.172	906.37	887.31	5.58	4.58	17.93	55.72	64.2	45.6	120.	0

An attempt was made to study the MAD data for the three-pass and six-pass tests. The data (Figure 6-1, Figure 6-2 and Figure 6-3), however, did not allow for much interpretation, particularly in finding the presence of increased grain rotation up to the point where low-angle grain boundaries form high-angle grain boundaries typical of CDRX. In addition, it is noted that all areas analysed were not of the same orientations, and different grains have different recrystallisation behaviour and different precipitate densities.

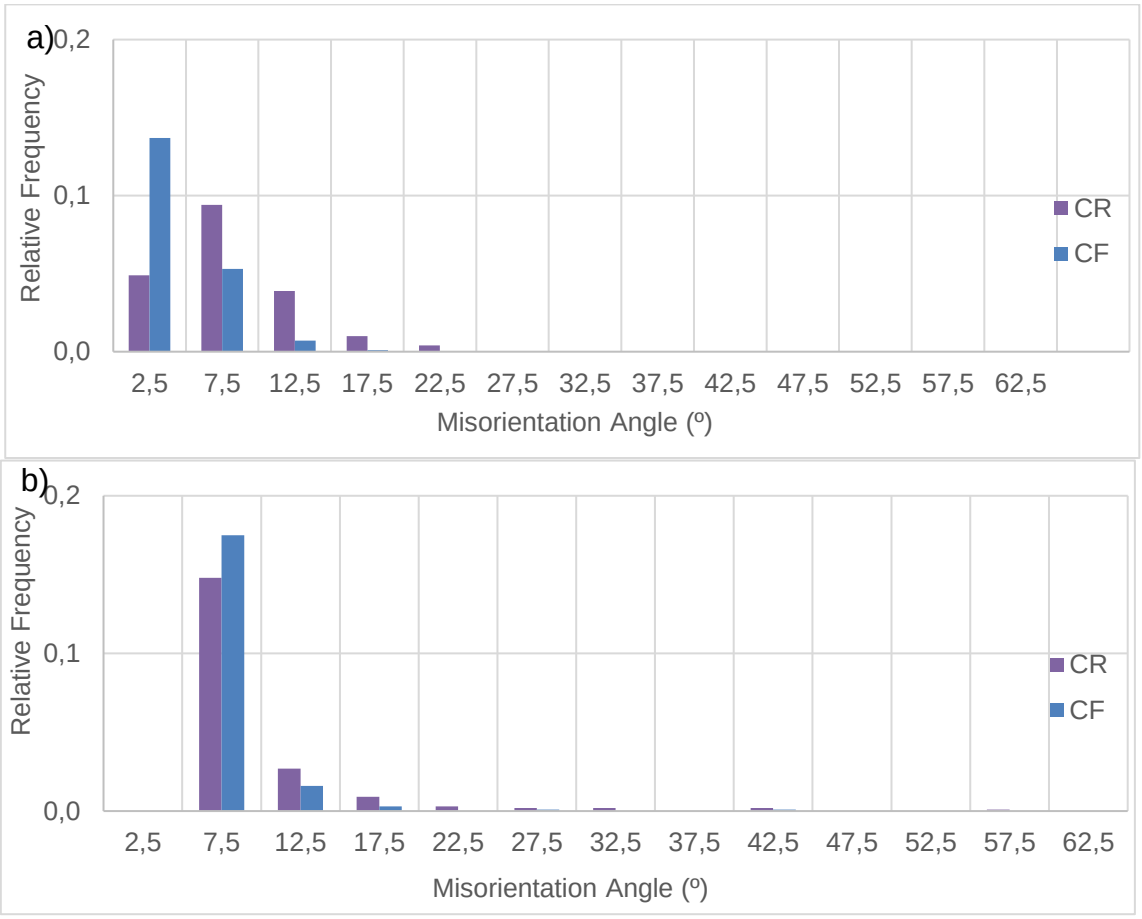

Figure 6-1: Misorientation angle distribution of CR and CF sample. a) Uncorrelated, and b) correlated data corresponding to EBSD areas analysed in Figure 4-27.

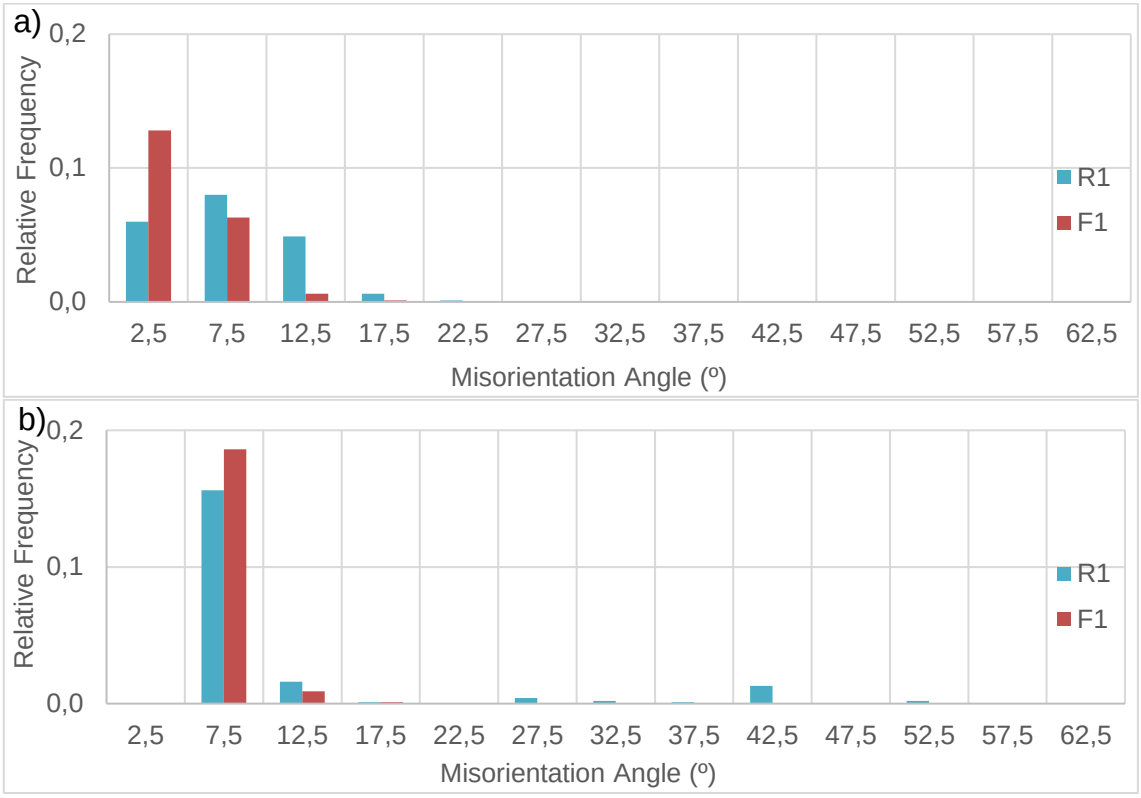

Figure 6-2: Misorientation angle distribution of R1 and F1 samples. a) Uncorrelated, and b) correlated data corresponding to EBSD areas analysed in Figure 4-27.

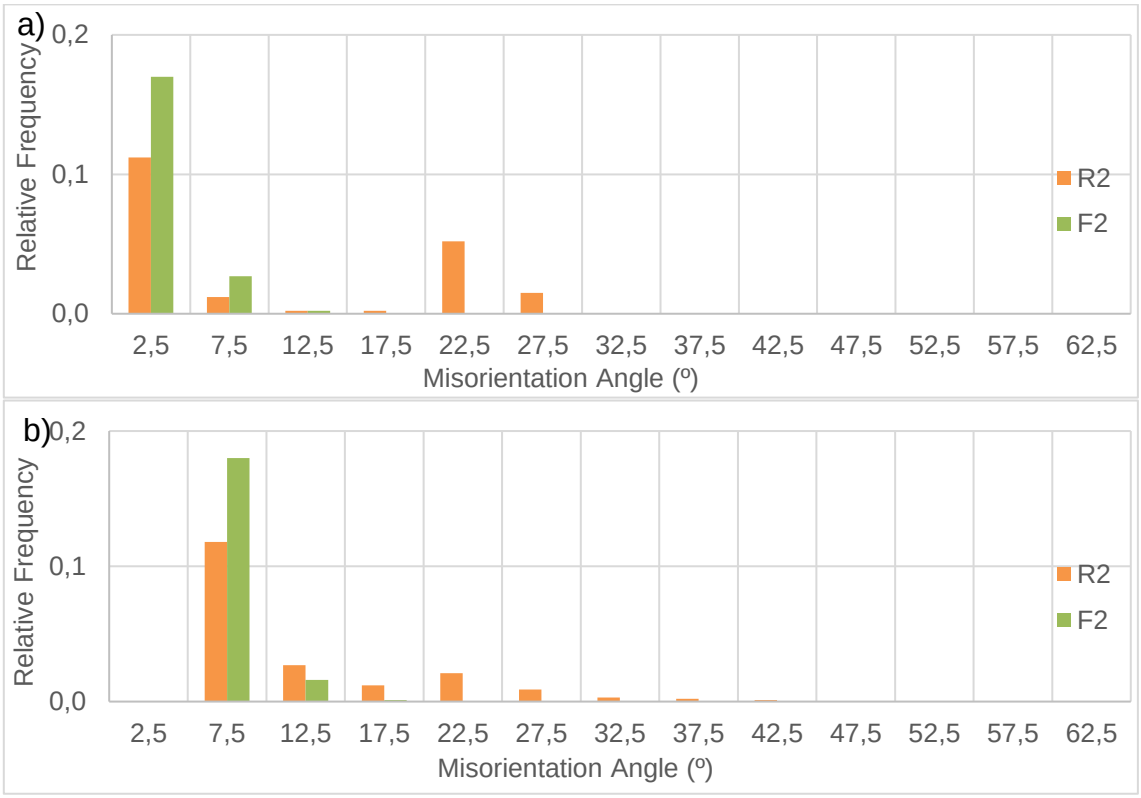

Figure 6-3: Misorientation angle distribution of R2 and F2 sample. a) Uncorrelated, and correlated data corresponding to EBSD areas analysed in Figure 4-27.

	IPF Maps	Recrystallisation Maps	Recrystallised grains	Map Area
CR	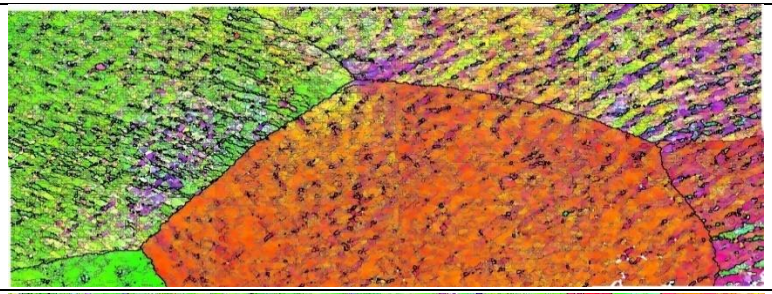	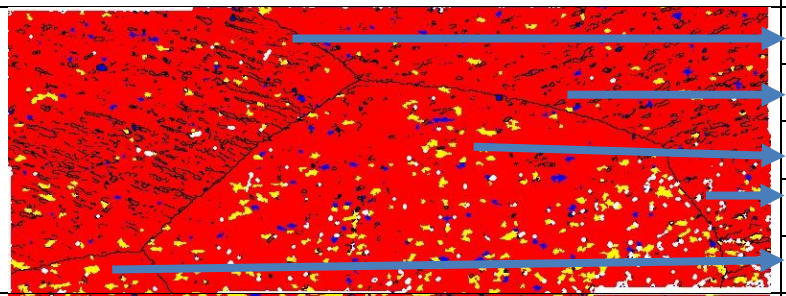	80 70 110 15 5	1500 µm X 500 µm
R1	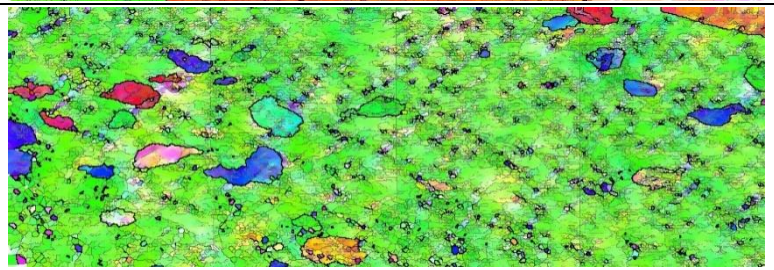	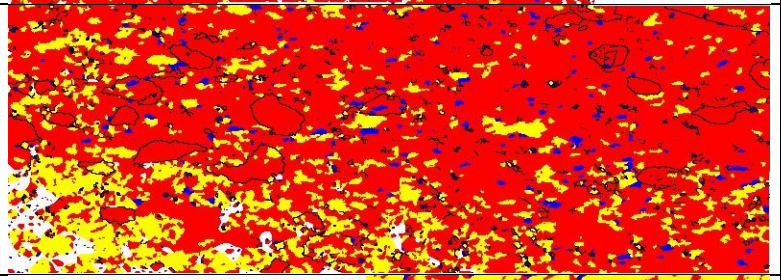	130	1500 µm X 500 µm
R2	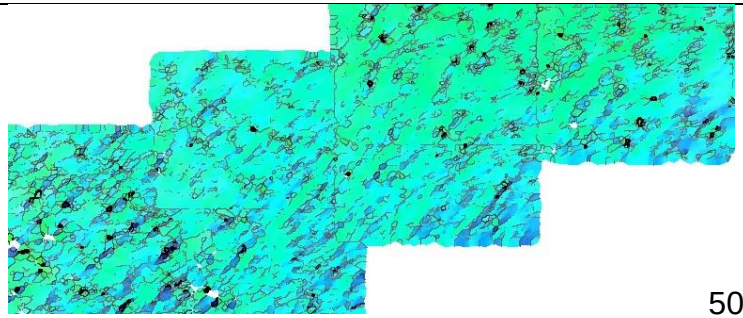	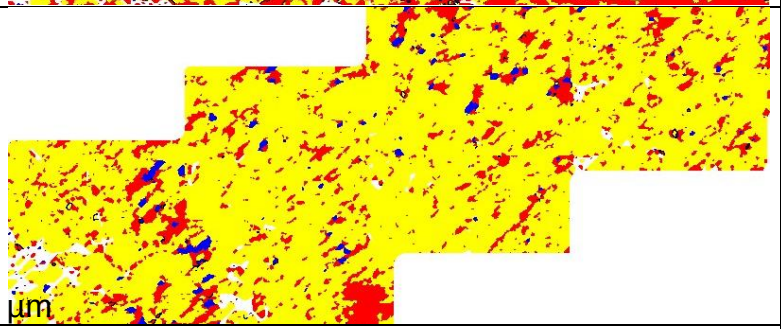	70	1400 µm X 500 µm
	500 µm			

Figure 6-4: IPF maps for samples with corresponding recrystallisation plots for 3-pass simulation of CR, R1 and R2 with red representing deformed material, yellow representing substructure material and blue representing recrystallised material. The number of recrystallised grains formed in each parent grain was counted to give some statistical validity to results.

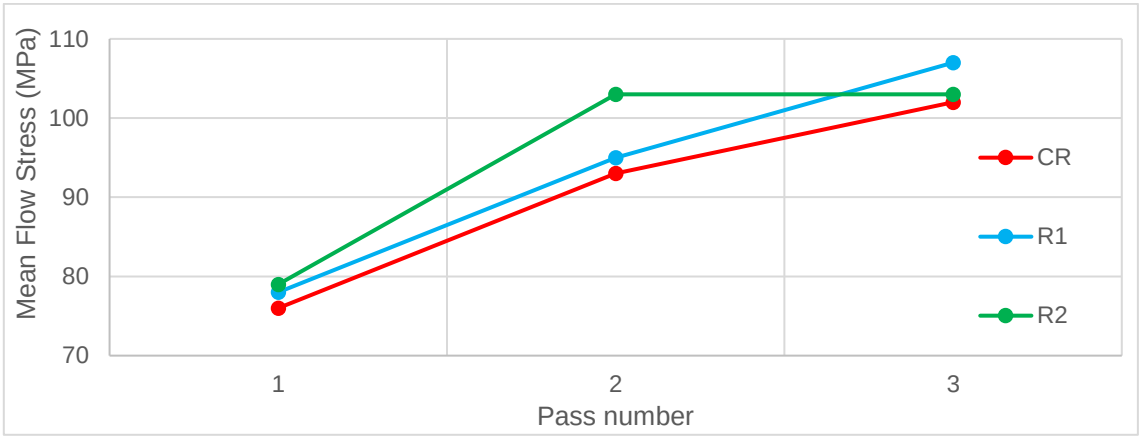

Figure 6-5: Mean flow stress for the 3-pass roughing rolling simulation at 5/s as a function of the number of passes.

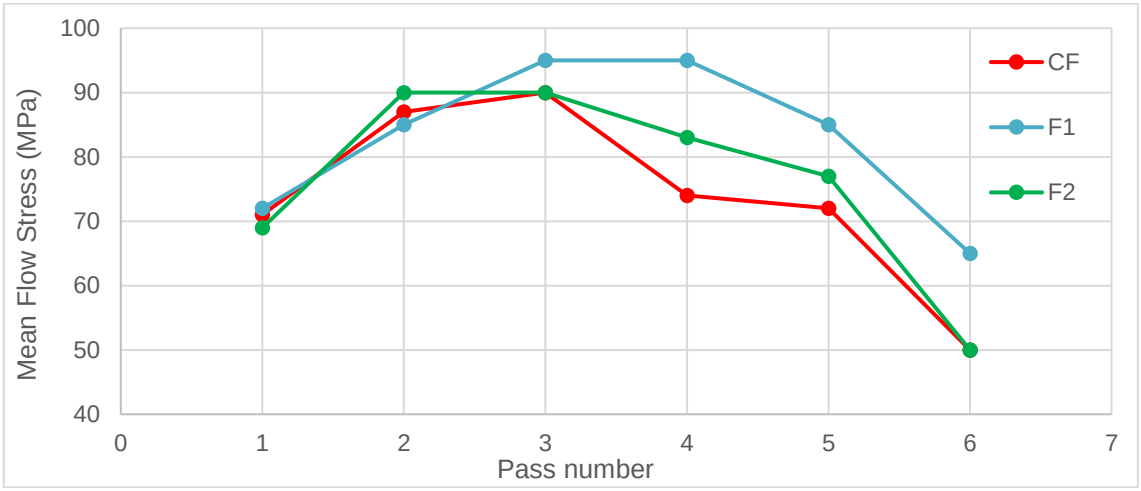

Figure 6-6: Plot of the mean flow stress for the 6-pass roughing and finishing rolling simulations as a function of the number of passes.

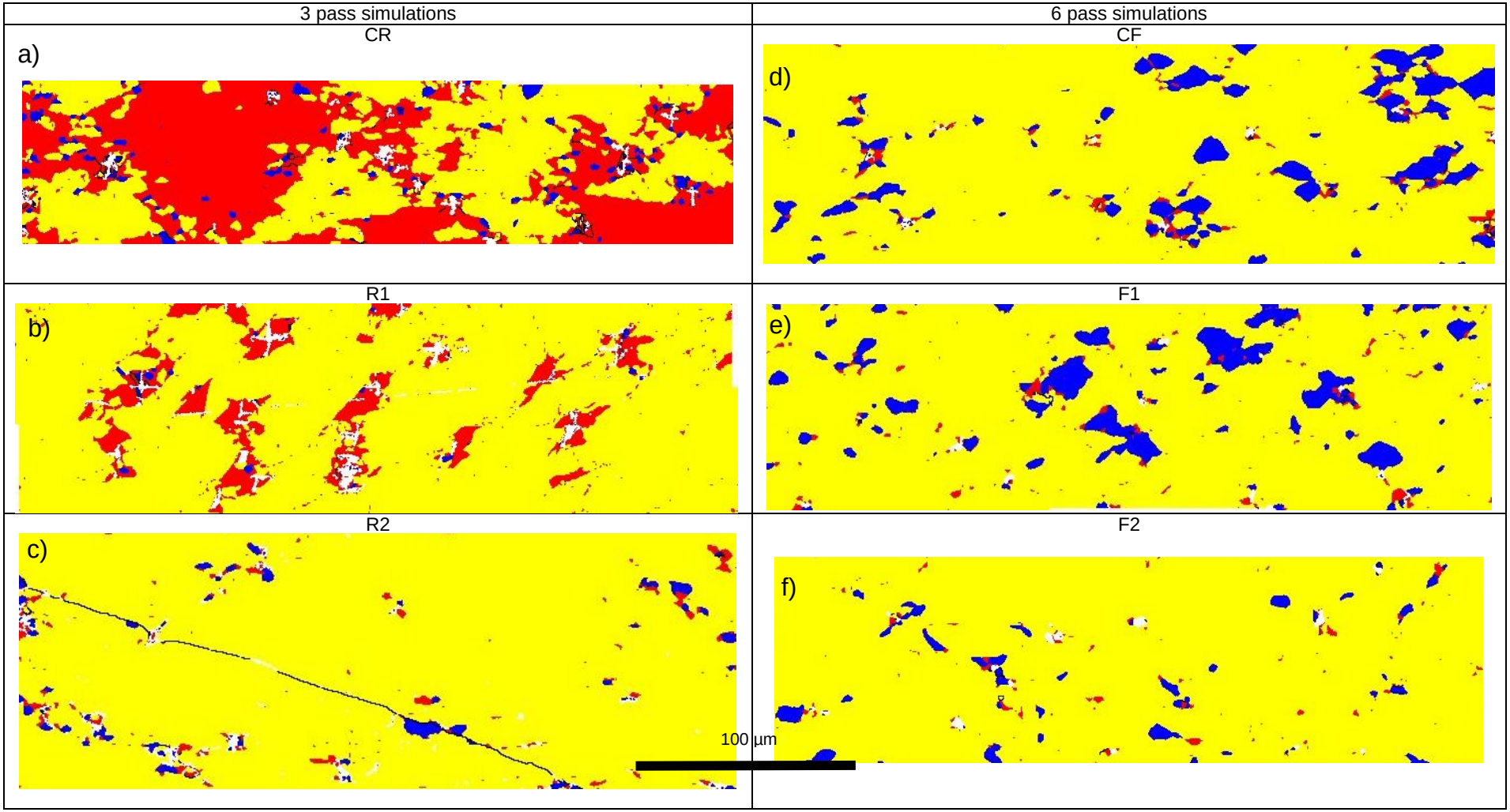

Figure 6-7: Variations in recrystallisation maps after 3 and 6-passes. All samples are observed at the same magnification. Black lines represent boundaries greater than 15°. Red areas represent deformed material, yellow represents substructure material and blue represents recrystallised material.

Table 6-4: Recrystallisation percentage data after 3 and 6-passes for recrystallisation maps in Figure 6-7

	3			6		
	CR	**R1**	**R2**	**CR/ CF**	**R1/ F1**	**R2/ F2**
Recrystallised	3	0.4	2.6	8.9	8.2	2.6
Substructure	37.2	90	95.2	88.7	90.1	96.3
Deformed	59.7	9.6	2.2	2.4	1.7	1.1

Table 6-5 presents hardness results after 3 and 6-passes schedules before and after annealing of samples. Results are presented in Figure 4-10. Standard deviations are within 5 HV.

Table 6-5: Average hardness results (with standard deviations) on 3 and 6-passes schedules before and after annealing at 800 °C for 300 s.

	3-pass before anneal	3-pass after anneal	6-pass before anneal	6-pass after anneal
CR/CF	171.5 (2.6)	167.6 (4.8)	160.8 (3.6)	157.6 (3.3)
R1/F1	173.0 (3.5)	159.0 (1.4)	168.5 (1.2)	156.1 (1.7)
R2/F2	172.2 (3.5)	161.9 (4.1)	192.6 (3.3)	165.3 (4.4)

Figure 6-8 shows the minimal recrystallisation found in R2 roughing simulation. It showed the lowered presence of well-defined sub-grains suspected due to the formation of fine precipitates in the material, likely formed through strain-induced precipitation lowering the driving force for recrystallisation. Strain-induced precipitation would probably have occurred from the increased strain imposed during the first three passes. The same can be said for the F2 sample.

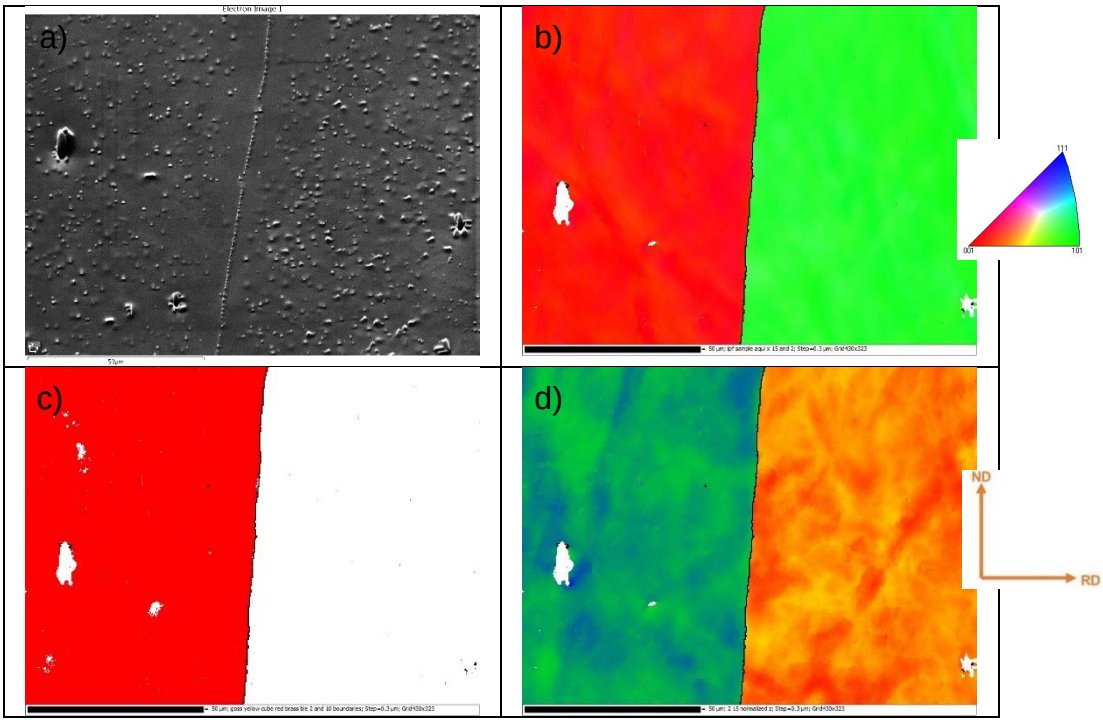

Figure 6-8: R2 sample, SEM image showing finely distribued pecipitates, with b) IPF image, and c) texture map, with cube texture in red showing minimal recrystallisation in the sample and d) Taylor factor heat map showing the grains were of different Taylor value.

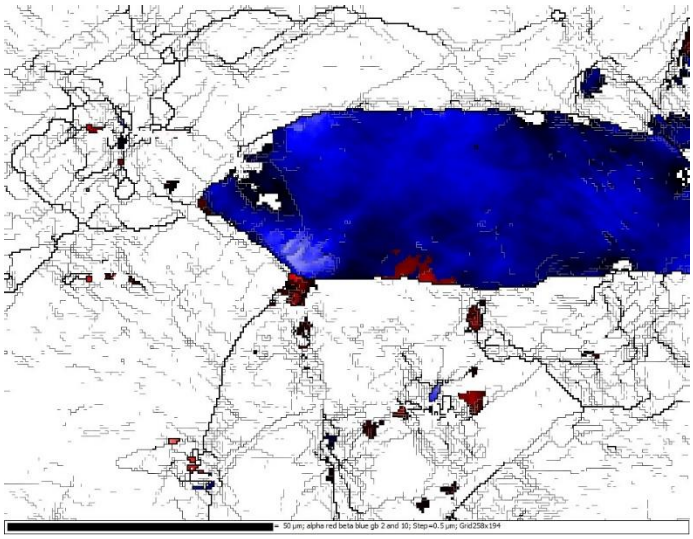

Figure 6-9: Texture map, close-up of Figure 4-31 showing Gamma fibre highlighted in blue and Alpha fibre in red for samples deformed under low strain rates and long inter-pass times.

Figure 6-10 presents SEM-EDS mapping showing precipitates surrounding inclusions. Inclusions were identified based on their oxygen content from the oxygen map. Furthermore, it is noted that areas, where precipitates form are depleted in Fe relative to the matrix and rich in Nb, signifying that these precipitates are Nb-rich precipitates.

As a better representation of results, all mapping analysis was done through the integrated mapping software of the Aztec software called Trumap analysis.

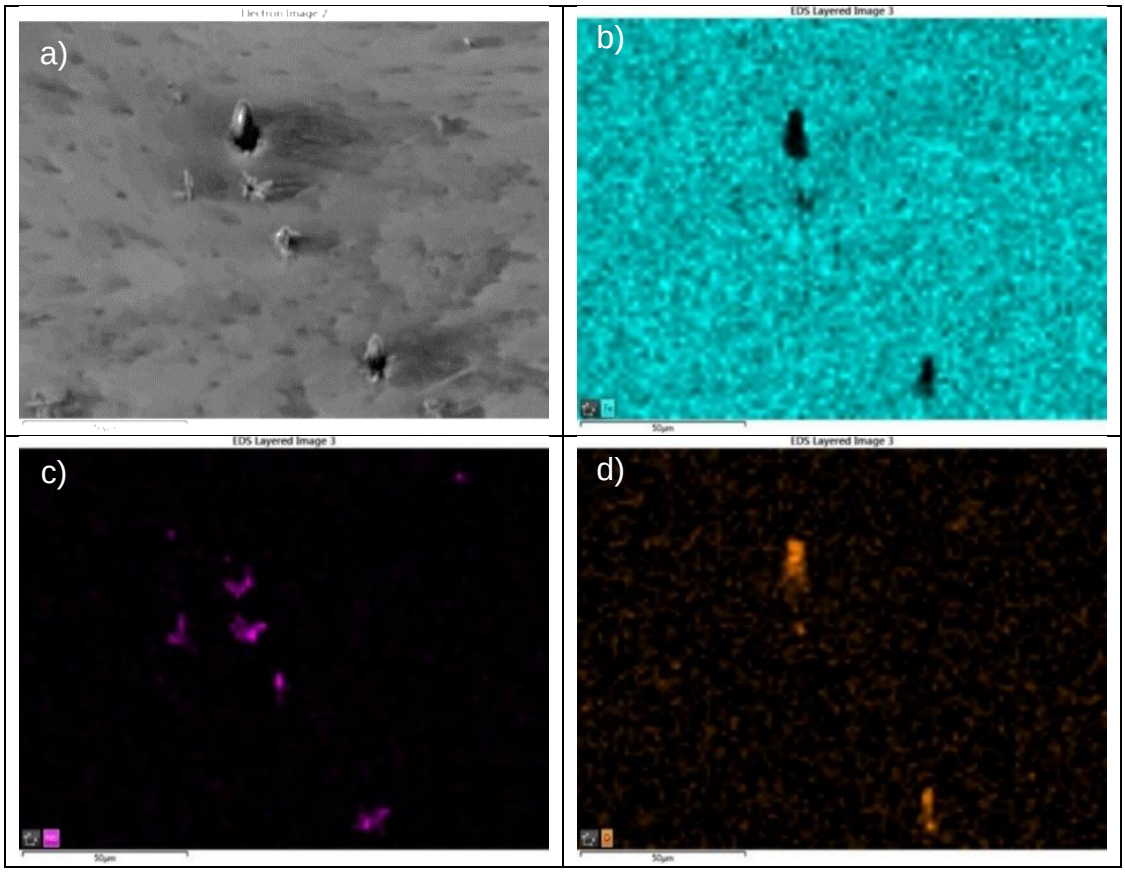

Figure 6-10: EDS mapping of sample CR-15/s taken during EBSD analyses. b) Blue map correlates with Fe, c) purple with Nb and d) orange with O. Note precipitates formed were around oxide inclusions and are Nb rich.

Figure 6-11 shows the precipitation behavior in the R2-15/s samples with high Nb content. The analysis indicates that precipitates were depleted of other metallic elements, such as Cr and Fe. The map results of R2-15/s are found in Figure 6-12: and correlate to the results from sample R1-15/s. The high concentration of Nb and other metallic elements at precipitate sites with depletion of Nb in the matrix is evident that these precipitates are Nb-rich.

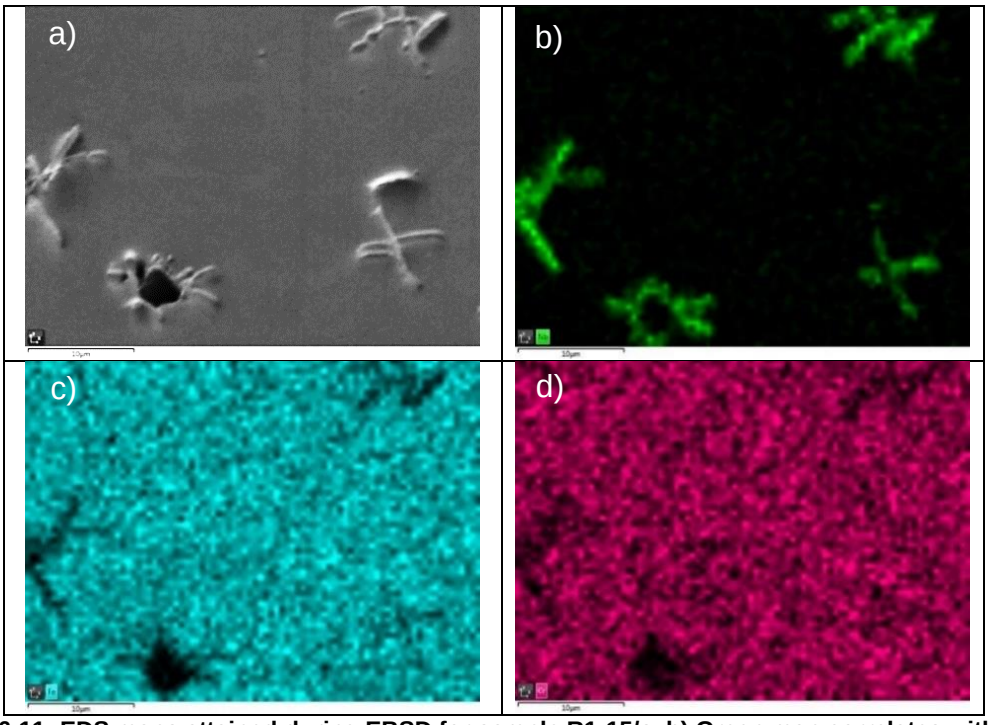

Figure 6-11: EDS maps attained during EBSD for sample R1-15/s. b) Green map correlates with Nb, c) blue with Fe and d) pink with Cr. Note precipitates formed were around oxide inclusions and with some being depleted of Cr and Fe, typical of NbC type precipitates.

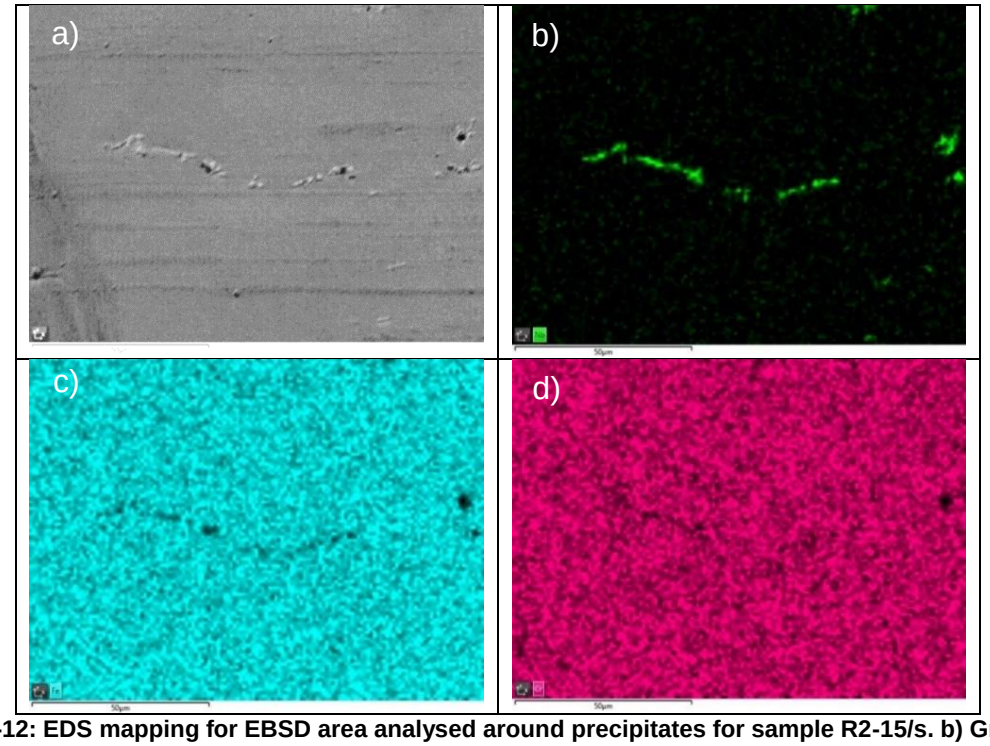

Figure 6-12: EDS mapping for EBSD area analysed around precipitates for sample R2-15/s. b) Green map correlates with Nb, c) blue with Fe and d) pink with Cr. Note precipitates formed were depleted of Fe, and formed along a band typical of segregation.

R2 and F2 deformation schedules samples were analysed to evaluate precipitate behavior. The SEM-EDS analysis of the precipitation behaviour from the heat treatment, finishing and roughing rolling are presented in Figure 6-14, and Figure 6-15.

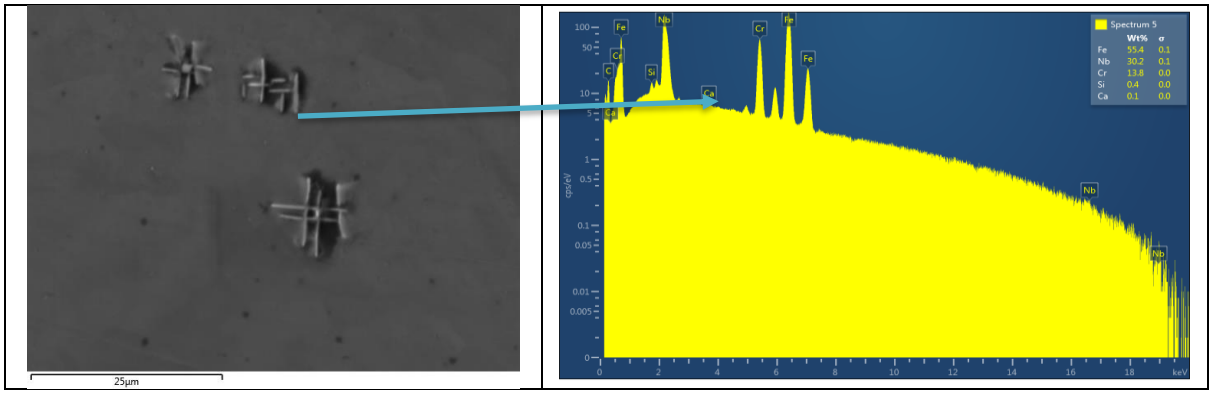

Figure 6-13: SEM micrographs and EDS analysis of samples deformed by following R2 schedule showing the presence of Laves phase.

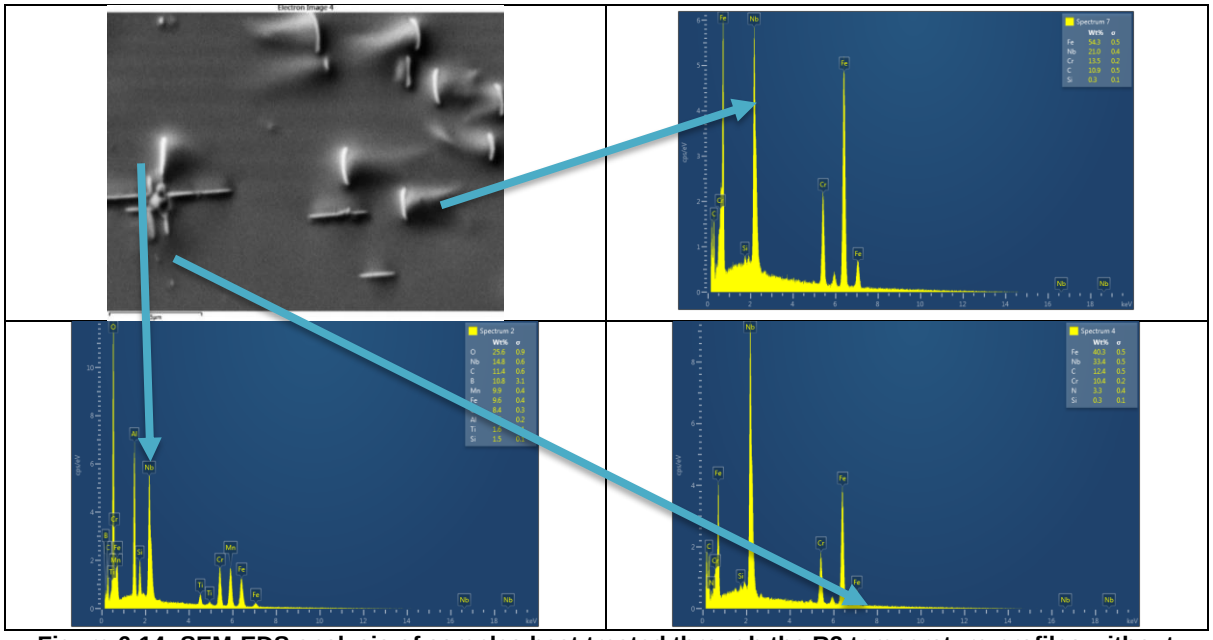

Figure 6-14: SEM-EDS analysis of samples heat treated through the R2 temperature profiles without deformation showing undeformed precipitates with compositions typical of Laves phase.

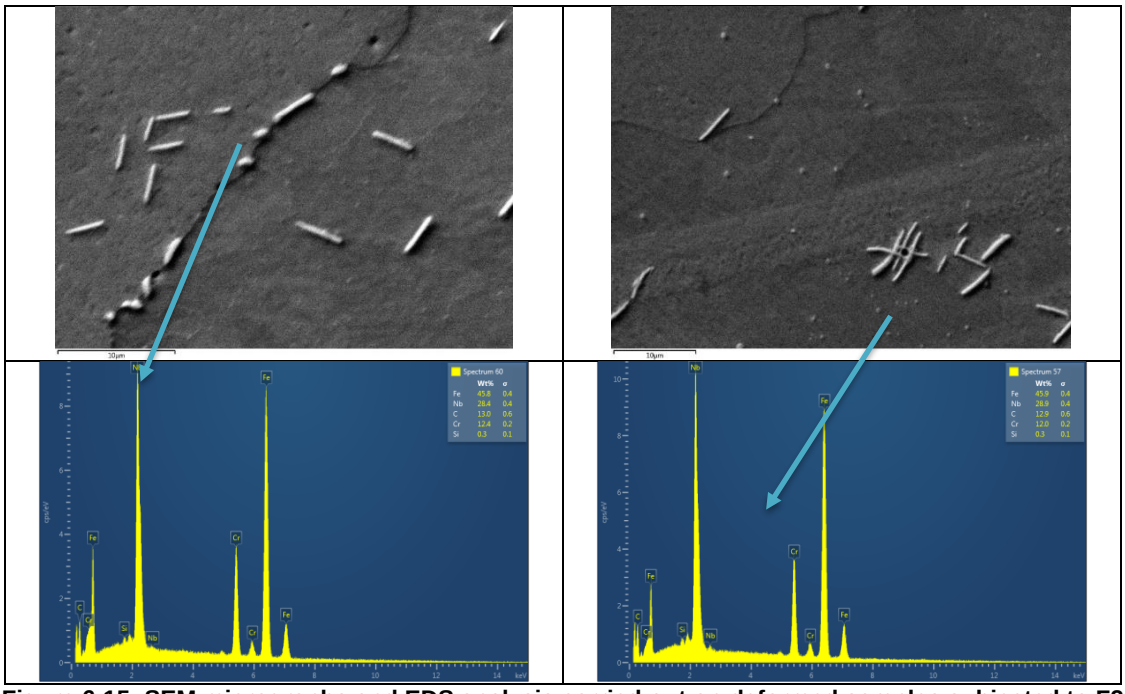

Figure 6-15: SEM micrographs and EDS analysis carried out on deformed samples subjected to F2 conditions showing needle-like precipitates.

Figure 6-16 presents Irregular shaped NbC which have nucleated heterogeneously on inclusions in the 6-pass control sample (CF).

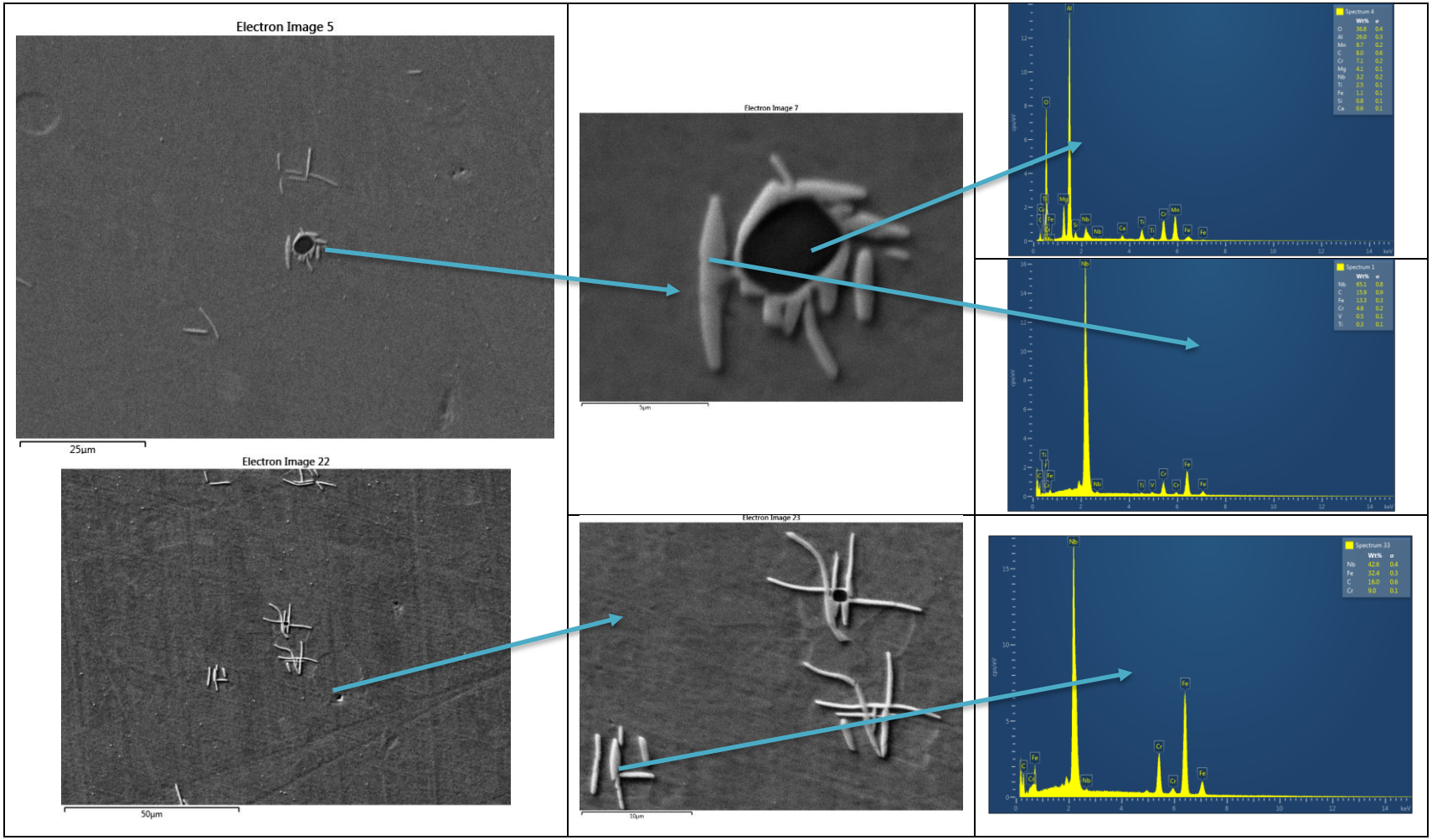

Figure 6-16: SEM-EDS analysis of 6 pass CF showing inclusions surrounded by Nb precipitates, and homogeneous precipitates correlating to Laves phase.

Figure 6-17 presents SEM micrographs and EDS analysis of the finishing rolling samples. Figure 6-17 shows prevalence of (Nb, Fe) C carbides which are comparable to the results obtained from the 6-pass Control schedule, where precipitates formed around inclusions. The star-like precipitate has morphologies similar to the Laves phase precipitate, but the composition correlates to (Nb, Fe) C.

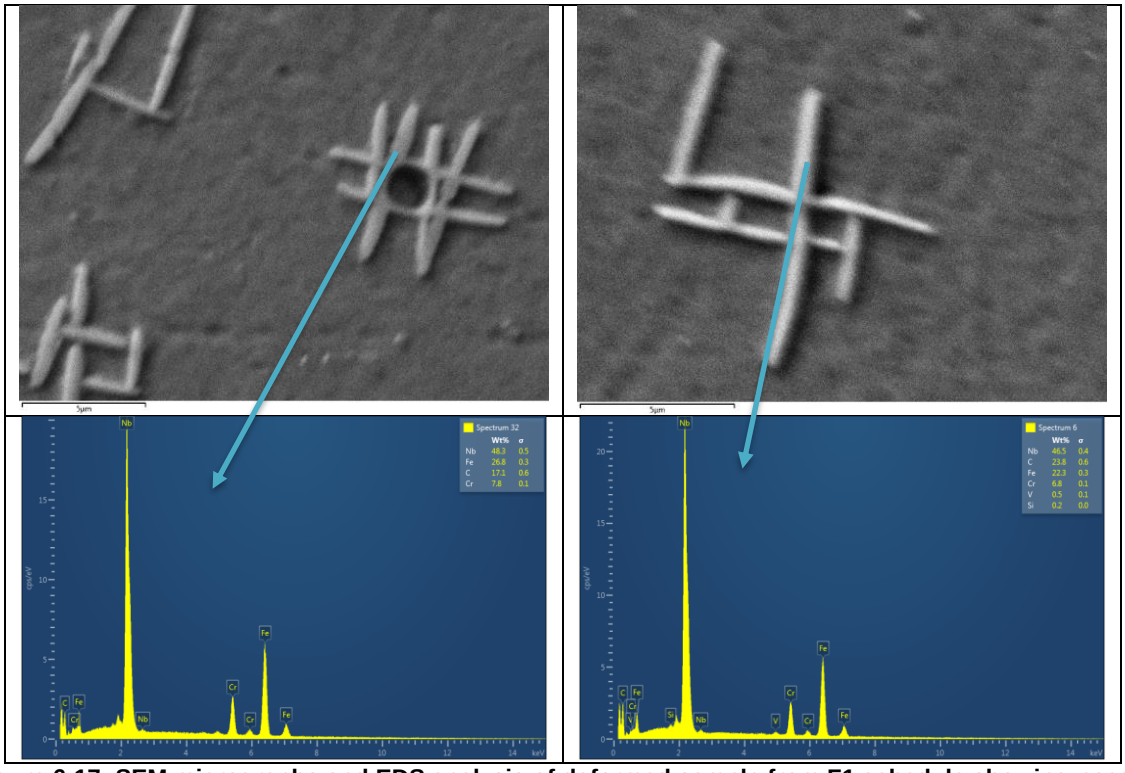

Figure 6-17: SEM micrographs and EDS analysis of deformed sample from F1 schedule showing needle like (Nb, Fe) C precipitates.